

---

# Increasing Resilience and Functionality of DNA-Assembled Structures

Linh Nguyen

---



München 2022



---

# **Increasing Resilience and Functionality of DNA-Assembled Structures**

**Linh Nguyen**

---

Dissertation  
an der Fakultät für Physik  
der Ludwig-Maximilians-Universität  
München

vorgelegt von  
Linh Nguyen  
aus Müllheim

München, den 26.09.2022





Erstgutacher/in: Prof. Dr. Tim Liedl  
Zweitgutachter/in: Prof. Dr. Philip Tinnefeld  
Tag der mündlichen Prüfung: 21.11.2022

## PUBLICATIONS

---

Publications based on the results of this thesis:

- *DNA-Origami-Templated Silica Growth by Sol–Gel Chemistry*  
L. Nguyen, M. Döblinger, T. Liedl & A. Heuer-Jungemann\*  
**Angewandte Chemie**, 2018.
- *Chiral Assembly of Gold-Silver Core-Shell Plasmonic Nanorods on DNA Origami with Strong Optical Activity*  
L. Nguyen, M. Dass, M. F. Ober, L. V. Besteiro, Z. M. Wang, A. O. Govorov, B. Nickel, T. Liedl & A. Heuer-Jungemann\*  
**ACS Nano**, 2020.
- *Picomolar Analyte Detection in Lateral Flow Immunoassays by DNA Origami Signal Amplification*  
L. Nguyen, C. Sikeler, S. Van Rest, T. Liedl, P. Nickels\* & M. Urban\*  
Manuskript, 2021.

Further publications:

- *Method of Making Nanoparticles in an Aqueous Solution Providing Functionalization and Hindered Aggregation in One Step*  
L. Nguyen, A. Heuer-Jungemann, M. Urban, T. Liedl & LMU  
**European Patent Application**, 19210989.0-1103, 2019.
- *Long-and Short-Ranged Chiral Interactions in DNA Assembled Plasmonic Chains.*  
K. Martens, F. Binkowski, L. Nguyen, L. Hu, A. O. Govorov, S. Burger, and T. Liedl  
**Nature Communications**, 2021.
- *DNA Origami Nano-Sheets and Nano-Rods Alter the Orientational Order in a Lyotropic Chromonic Liquid Crystal*  
B. Zhang, K. Martens, L. Kneer, T. Funck, L. Nguyen, R. Berger, M. Dass, S. Kempter, J. Schmidtke, T. Liedl & H.-S. Kitzerow  
**Nanomaterials**, 2020.
- *Lipid Bilayer-Coated Curcumin-Based Mesoporous Organosilica Nanoparticles for Cellular Delivery*  
S. Datz, H. Engelke, C. V. Schirnding, L. Nguyen & T. Bein  
**Microporous and Mesoporous Materials**, 2016.

## ZUSAMMENFASSUNG

---

Mithilfe der DNA Origami Technik können nanometergroße 1-, 2- und 3-dimensionale Strukturen aus DNA mit hoher Präzision hergestellt werden. Die Wechselwirkung zwischen Basenpaaren ermöglicht die genaue Kontrolle über die DNA Origami Struktur. Im Vergleich zu anorganischen Materialien sind diese jedoch weniger chemisch oder physisch stabil. Anorganische Materialien sind meist formstabil und widerstandsfähig. Der Nachteil besteht jedoch darin, dass keine hochkomplexen Strukturen durch Selbstassemblierung hergestellt werden können.

In dieser Arbeit wird ein Verfahren vorgestellt um anorganisch-organische Hybridmaterialien herzustellen, die aus einer formgebenden DNA Struktur und einer formerhaltenden Silikahülle bestehen. Damit konnten die Vorteile beider Materialklassen genutzt werden um sowohl stabile als auch hochkomplexe Strukturen herzustellen.

Des Weiteren wurde eine schnelle und einfache Methode entwickelt um silberummantelte Goldstäbchen herzustellen, die an ihrer Oberfläche mit funktionaler DNA ausgestattet sind. Diese bimetallischen Stäbchen haben plasmonische Eigenschaften mit sehr leicht einzustellender Resonanz im sichtbaren Bereich. Mithilfe der DNA Origami Technik konnten die Stäbchen räumlich präzise angeordnet werden um ihre optischen Eigenschaften und synergistischen Effekte zu untersuchen.

Schließlich wurden die bimetallischen Stäbchen in Form von DNA Origami-Nanopartikel-Konjugaten in chromatographischen Schnelltests eingesetzt um eine Signalverstärkung zu erzielen. Da die DNA Origami-Nanopartikel-Konjugate ein viel stärkeres Signal emittierten als konventionelle Nanopartikel, konnte die Sensitivität und damit auch die Zuverlässigkeit dieser Schnelltests verbessert werden. Die Technik wurde anfänglich mithilfe von DNA-Schnelltests entwickelt. Die darauffolgende Weiterentwicklung der Technik geschah mithilfe von konventionellen Schwangerschaftsschnelltests und führte zu einer signifikanten Erhöhung der Sensitivität. In weiteren hoch-sensitiven Antigenschnelltests konnten mithilfe der bimetallischen Gold/Silber-Stäbchen unterschiedliche Farbsignale erzeugt werden, die das Potenzial haben zukünftig für die Detektion mehrerer Biomarker gleichzeitig eingesetzt zu werden.

## ABSTRACT

---

The DNA origami technique can be used to fabricate nanometer-sized 1-, 2-, and 3-dimensional structures with high precision and controllability. DNA is an excellent construction material owing to its specific base pair interaction. However, DNA origami structures are less thermally, chemically or mechanically resilient compared to inorganic materials. Inorganic materials keep their integrity but controllable nanostructures are virtually not accessible through self-assembly. In this work a method is presented to produce inorganic-organic hybrid structures consisting of a template DNA structure and a protective silica shell. By combining the advantages of each material class highly stable and complex structures could be fabricated.

Furthermore, a fast and simple method was developed to fabricate gold-silver core-shell nanorods with a functional DNA layer on their surface. These bimetallic rods have special plasmonic properties with resonances that can be easily tuned in the visible range. They were precisely arranged into a chiral structure using DNA origami which allowed us to study their optical properties and synergistic effects.

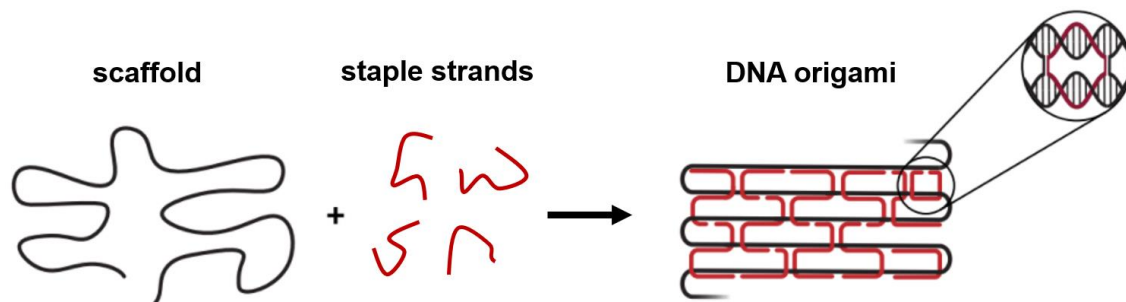
Finally, these bimetallic rods and other plasmonic particles were applied as DNA-origami-nanoparticle conjugates in lateral flow assays (rapid tests). The sensitivity and thus the reliability of these rapid tests were improved since the DNA-origami nanoparticle conjugates emit stronger signals than state-of-the-art individual nanoparticles. After the conjugates were applied in DNA detection assays, the technique was further developed for reliable antigen detection. An anticipated strong signal enhancement was obtained in conventional home pregnancy tests. In further sensitive antigen tests the gold-silver core-shell nanorods performed excellently while signals of various colors were introduced which have a potential for use in multiplex assays.

# List of Contents

1	Introduction.....	1
2	Theoretical Background & Methodology.....	12
2.1	Sol Gel Chemistry.....	12
2.2	Plasmon Hybridization Model.....	15
2.3	Rapid Test / Lateral Flow Assay.....	19
3	DNA Origami-Directed Silica Mineralization.....	23
3.1	Associated Publication 1.....	28
4	One-Pot Synthesis of Gold-Silver Nanorods for Plasmonic Application.....	33
4.1	Associated Publication 2.....	38
5	Using DNA Origami in Rapid Tests for Signal Amplification.....	46
5.1	Associated Manuscript.....	57
6	Appendix.....	68
6.1	Supporting Information for Publication 1.....	68
6.2	Supporting Information for Publication 2.....	85
7	Bibliography.....	100

# 1 Introduction

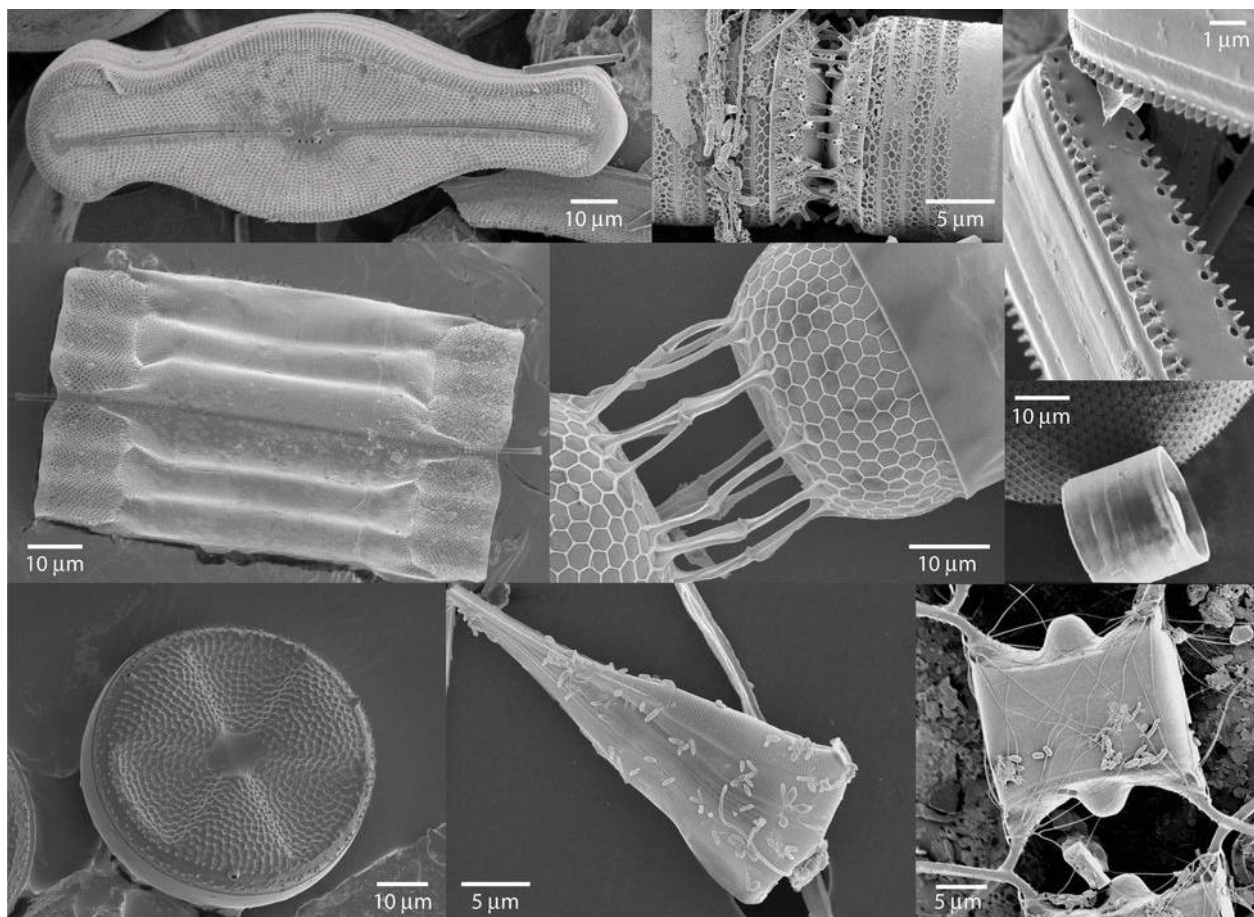
For fabricating structures at the nanoscale, two main approaches have been established: the top-down and the bottom-up technique.<sup>[1]</sup> Starting from bulk material, top-down techniques involve molding, casting, and ablation producing smaller parts forming the final structures. In contrast, bottom-up techniques rely on self-assembly and growth which produces larger structures consisting of individual single units. Top-down techniques are mostly applied on inorganic hard materials such as silicon where covalent bonds cause rigidity and resistance. Breaking and connecting new covalent bonds using mechanical and chemical force and energy is key for the fabrication of nanostructures. Weaker interactions like hydrogen bonds, electrostatic or Van der Waals forces are prominent in soft organic matter, which allow intermolecular movement, bonding and debonding processes under mild condition. The dynamic processes allow self-assembly in a controlled manner. For instance, the formation of hydrogen bonds between base pairs is essential for self-assembly of Deoxyribonucleic acid (DNA) into higher-ordered structures. This lays the ground for the DNA origami method where a long, single-stranded DNA (ssDNA, ~7 kb, "scaffold") is folded into rationally designed shapes using short ssDNA ("staple strands") (**Figure 1**).<sup>[2]</sup> DNA origami is one of the most convenient and reliable bottom-up strategies used in soft matter.



**Figure 1. DNA origami method. Folding mechanism.**<sup>[3]</sup>

## **1.1 Bottom-Up for Hard Matter**

There is no bottom-up strategy for inorganic matter as self-assembly into desired shapes is not accessible due to their intrinsic properties. However, some natural, bottom-up synthesized hard materials with complex shapes do occur in nature, including minerals, crystals, seashells, pearls, bone, and teeth. These materials are fabricated in a controlled manner from micro to macro scale resulting in sophisticated and multilevel-ordered structures. Furthermore, they are eminent for their impressive mechanical strength and rigidity. Biominerals are great examples for the vast variety of distinct patterns. Living organisms such as diatoms produce biominerals in order to ensure viability. During the mineralization process, the organism's soft tissue is used as a template to grow hard materials, typically calcium phosphate, calcium carbonate, or silicon dioxide. Here, many different, perfectly matched processes take place simultaneously and successively. As a result, the structure and shape of the soft organic tissue is transcribed into a solid shell that provides stability, protection, and functionality. Constructing such rigid and elaborate nanostructures in the laboratory is a major challenge. However, understanding and mimicking these individual processes that have been evolutionarily optimized, provides a step towards advanced and functional materials. This is performed for example in biomimetic chemistry.



**Figure 2. Scanning electron microscope (SEM) images of diatoms.<sup>[4]</sup> Adapted with permission.**

The concept of pre-organization and templating was first proposed by Stephen Mann in the 90s. He described it as “synthesis-with-construction”.<sup>[5]</sup> A key aspect of this approach is the integration and connection of organic self-assembly and inorganic reaction chemistry. Organic-inorganic hybrid materials were synthesized using templates such as proteins, DNA, and viruses and coating materials such as silica, titanium dioxide, and polymers.<sup>[6]</sup> Only recently have DNA origami structures been used in the mineralization process and subsequently turned out to be an excellent template, particularly since DNA origami structures provide custom designed shapes in 2 and 3 dimensions. The first silica-mineralized (silicified) DNA origami structures adsorbed to a copper grid were reported in 2018<sup>[7]</sup>, shortly before the work presented here was published.<sup>[8]</sup> We demonstrated a strategy for the silicification of high concentrations of 1 and 3 dimensional DNA origami in solution which is presented in **Ch. 3**. Especially the silicification of a DNA origami crystal proved the rigidity and support of the solid shell since the “naked” origami crystal was



prone to deformation and collapse. Our method was the first bottom-up synthesis of a hard nanomaterial with periodic structure in the laboratory. The silicified DNA origami structures further showed mechanical, thermal and chemical stability owing to the silica shell. The silica mineralization of DNA origami has become a fast-developing technique in the last four years. Since the initial interdisciplinary work was reported, a plethora of silica structures with high level of complexity and further improvements of the method itself have been reported.<sup>[7, 9-24]</sup>

## 1.2 Advances in Colloidal Systems

Another example of a dispersed system includes metal nanocrystals (nanoparticles, colloids) that can be accessed either via bottom-up or top-down techniques, e.g. through wet chemical synthesis or lithographic techniques such as laser ablation.<sup>[25]</sup> For high-throughput fabrication the bottom-up methods such as the “seeding growth method” are more efficient. However, metal colloids are not a recent discovery; their use dates back to the ancient times (as shown in the timeline of colloidal systems in Error! Reference source not found.).<sup>[26]</sup> Metal colloids such as gold (Au), silver (Ag), and copper (Cu) nanoparticles (NPs) were used in the ancient world by the Romans and the Chinese for staining glass. Back then, it was not known that the color originated from the metal nanocrystals embedded in the glass. Further examples where metal NPs were used are in medieval church windows, Islamic lusterware, and Renaissance pottery. Later, in 1857, Michael Faraday accidentally produced a solution of dispersed AuNPs while making thin Au films using a chemical process.<sup>[27]</sup> After washing the Au films, he obtained a red solution which he called “Ruby gold”. He deduced that the solution must contain AuNPs which were too small to observe with the scientific instruments of his time. Only in 1990, gold-silver alloy NPs embedded in the famous “Lycurgus cup” were first visualized using transmission electron microscopy.<sup>[28]</sup> This cup appears green or red depending on the direction of the light source. It is probably the oldest (4<sup>th</sup> century AD) known example with optical features caused by the surface plasmon phenomenon (**Ch. 2.2**). Plasmons are collective electron vibrations that are excited through light. These electron vibrations give an intense color impression. Despite the ubiquity of NPs since ancient times, the development of scientific knowledge about these systems has been relatively recent. Richard Zsigmondy worked on the heterogenous nature of colloidal solutions for which he was awarded the Nobel Prize in chemistry in 1925.<sup>[27]</sup> The chemical synthesis was developed and improved over




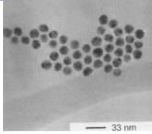

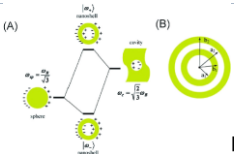
the years from Turkevich<sup>[29]</sup> (1951), over Brust-Schiffrin<sup>[30]</sup> (1994) to the seeding growth method<sup>[31]</sup> (2001). It was not until 2001, when anisotropic gold and silver nanorods (NR) were synthesized for the first time. Today, different NP shapes are accessible; the spherical ones are most widely and commercially used. Au colloids are used e.g. for bioimaging, or as drug, gene, and protein carriers in nanomedicine.<sup>[32]</sup>

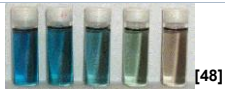
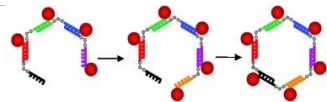
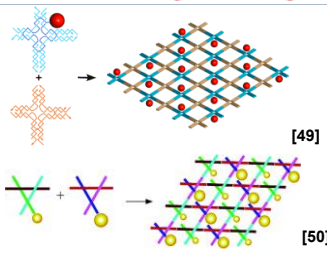
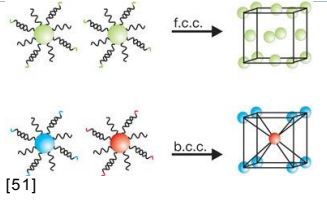
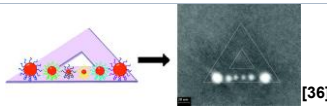
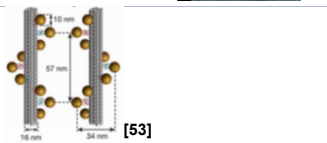
In recent developments in DNA nanotechnology, metal nanocrystals are integrated in controlled systems where they are rationally ordered. This involves knowledge about the interplay between colloidal systems and the physical behavior of soft matter. As of today, the creation of nanostructures is key for a deeper understanding of the science behind it. For understanding metal NP interactions, it is of paramount importance to be capable of generating them. This is a general scientific idea coined by Richard Feynman:

***“What I cannot create, I do not understand.”***

The first self-assembly of AuNPs into ordered macroscopic structures using DNA as a linker was reported independently by Mirkin<sup>[33]</sup> and Alivisatos<sup>[34]</sup> in 1996. After that, more complex DNA nanostructures such as tetramers and hexagons<sup>[35]</sup> were developed to organize AuNPs. In 2010, AuNPs were assembled using a DNA origami structure.<sup>[36]</sup> The fabrication of functional materials with structural hierarchy and increasing complexity requires a synergy of multiple disciplines, structural addressability being one major advantage of DNA origami. By controlling the distance and orientation between NPs, complex NP arrays and assemblies in all three dimensions can be fabricated today with special optical features based on plasmon interactions. One example of these interactions is plasmonic chirality, where a chiral assembly of NPs interacts differently with light depending on its handedness.<sup>[37-38]</sup>

**Table 1. Timeline: Colloidal systems and their controlled assembly using DNA.**

Time	Who/what	What	Outline
4 <sup>th</sup> century	"Lycurgus cup"	Colored glass with Au <sub>0.3</sub> -Ag <sub>0.7</sub> alloy NPs	 [39]
500 – 1450 6 <sup>th</sup> -15 <sup>th</sup>	European Cathedrals	Colored glass with Au, Ag, Cu NPs	
9 <sup>th</sup> -17 <sup>th</sup>	Islamic lusterware	Ag and Cu NPs	
1857	Michael Faraday	"Ruby gold"	 [40]
1871	Black-and-white photography	AgNPs	
1900	Richard Zsigmondy	AuNP synthesis with reducing agents	
1925	Nobel prize Zsigmondy	Heterogenous nature of colloid solutions	 [41]
1950	Viktor LaMer and Robert Dinagal <sup>[42]</sup>	Monodisperse colloidal materials	
1951	Turkevich <sup>[29]</sup>	AuNP synthesis with reduction of HAuCl <sub>4</sub> using citrate	Known as "Turkevich method"
1952	Pines and Bohm <sup>[43]</sup>	Plasmons	
1957	Rufus Richie <sup>[44]</sup>	Surface plasmons	
1994	Brust and Schiffrin <sup>[30]</sup>	AuNP synthesis using alkane thiol as stabilizer; AgNP synthesis	Known as "Brust-Schiffrin method"
1996	Mirkin and Letsinger <sup>[33]</sup> Alivisatos <sup>[34]</sup>	Organizing AuNPs using DNA	 [33]
2000s	Consumer products	AgNPs	
2001	Jana and Murphy <sup>[31]</sup>	AuNP synthesis	"Seeding growth method for NPs"
2001	Murphy <sup>[45]</sup>	AuNR synthesis	
2003	Halas <sup>[46]</sup>	Plasmon hybridization theory	 [46]
2005	Murphy <sup>[47]</sup>	Au and Ag NR synthesis	"Seeding growth method for NRs"

2005	Perez-Juste and Liz-Marzan <sup>[48]</sup>	AuNR synthesis	 [48]
2006	Sleiman <sup>[35]</sup>	AuNP DNA hexagon	
2006	Yan <sup>[49]</sup> Seeman <sup>[50]</sup>	AuNP arrays	 [49] [50]
2008	Mirkin <sup>[51]</sup> Gang <sup>[52]</sup>	AuNP DNA crystals	 f.c.c. [51] b.c.c.
2010	Ding <sup>[36]</sup>	AuNPs on DNA Origami	 [36]
2011	Liedl <sup>[53]</sup>	Chiral AuNP assembly with DNA origami	 [53]

The examples shown in **Table 1** highlight our access to materials with specific electric and magnetic properties. In order to tune these properties for further advancement in this area, the use of distinct NP shapes and materials is required. This includes the organization of anisotropic metal NPs. Driving progress towards the assembly of anisotropically shaped NPs expands our understanding of novel optical phenomena. Rod-shaped AuNPs, for example, have distinct plasmon resonances from the visible to the near infrared range which not only gives access to a variety of colors but also the possibility to shift plasmon phenomena to desired spectral areas, extending their potential application. Silver is proposed as best material with respect to plasmonic behavior including long plasmonic lifetime and narrow resonance bandwidth with strong intensity (discussed in **Ch. 2.2 & 4**). However, the use and functionality of silver nanoparticles (AgNPs) is still limited due to oxidation which involves practical difficulties. Since Au provides excellent chemical stability, the use of a bimetallic NR can provide a combination and synergy of desired features based on the properties of both metals. The work presented here establishes the functionalization and organization of a bimetallic core-shell NR using DNA origami

(Ch. 3.1). The Au core provides stability and supports the Ag shell, while intrinsic plasmonic properties of the Ag shell can be generated that are superior to comparable metal NRs of different materials. Further development may include using the technique to fabricate large periodic 3D structures such as DNA origami crystal lattices decorated with NPs in a periodic geometry. These lattices could have optical properties similar to the ones found in generic photonic crystals – nanostructures with a periodic arrangement of materials having different refractive indices. Photonic crystals are of great interest to the scientific community for several reasons. One of their characteristic features is the so-called photonic bandgap: depending on the spacing between the building blocks, a photonic bandgap is created which describes a range of light frequencies that cannot pass through the material while other frequencies can. Another feature of photonic crystals is their ability to trap light in a cavity or guide it along certain pathways. Further, there is also a great amount of interest in using photonic crystals as a replacement for dyes.

### 1.3 Might DNA Origami Revolutionize Rapid Tests?

Although the DNA origami-based organization of NPs is of great scientific value, the use of such materials is as of yet not commercially viable in terms of large-scale production. Nevertheless, this thesis presents advancements in this field with improvements in making the technology sufficiently sound and dependable for a wide range of applications in the near future.

The ability to make use of the optical properties of individual NPs has shown a great economic and social value. The closest encounter of consumers with commercially used AuNPs is in the context of point-of-care lateral flow assays (LFA), also called “rapid tests” (Ch. 2.3). LFAs are designed for fast detection of biomarkers such as RNA, hormones, antigens, and antibodies.<sup>[54]</sup> Their remarkable commercial success can be attributed to numerous factors including easy operation, low manual input, portability, and low cost.<sup>[55]</sup> Point-of-care is at the time and place of patient care. A typical advertisement slogan for rapid tests is: “**Using the right test in the right place and time.**”. The basic and well-established technology has been used since the 1960’s.<sup>[56-57]</sup> Today, it is used in various disciplines such as medicine, specifically in hospitals and clinical laboratories, as well as in others including agriculture, quality control, food production safety, and environmental safety.<sup>[58-60]</sup> For example, potatoes are screened commercially for pathogens<sup>[61]</sup>, and hundreds of millions of malaria rapid tests are supplied globally per year.<sup>[62]</sup>

However, reliability for diagnosing diseases is lower compared to other analytical techniques established in laboratories such as real-time reverse transcription polymerase chain reaction assay<sup>[63]</sup> (RT-PCR) and enzyme-linked immunosorbent assay<sup>[64]</sup> (ELISA). Both techniques have become indispensable for the health care system since they provide high sensitivity and specificity. In the Third World however, often access to analytical instruments and set-ups is not given; medical laboratories and good infrastructure are scarcely available. Developing countries are struggling to meet the challenges of disease diagnostics and treatment. Since rapid testing provides a fast and cheap solution and sometimes is the only diagnostic tool amenable, they have made a great impact particularly in such low resource settings.<sup>[65]</sup> During the COVID-19 pandemic, in a state of emergency, the developed countries also have learned to appreciate rapid testing as a valid alternative and supplement to the more time-consuming and more expensive PCR testing.<sup>[66]</sup> At high infection rates, other factors than high specificity and sensitivity became essential including easy-access, short turnaround time, and frequency of testing. Antigen tests are an important complement to nucleic acid testing since they can deliver results within minutes by avoiding nucleic acid extraction and amplification steps. The SARS-CoV-2 rapid antigen test has become the most widely known LFA and gained widespread acceptance outside of health care settings. The assay targets the SARS-CoV-2 nucleocapsid protein, the most abundant protein expressed by the virus. Before the pandemic, such LFAs for the diagnosis of different diseases were only allowed to be purchased and operated by trained clinical personnel. However, the COVID-19 pandemic has brought lateral flow tests to the forefront of many healthcare agendas and to the general public. Within a short timeframe, cheap test strips were available for purchase in pharmacies, drugstores, and supermarkets. Its availability reduced the workload in centralized testing facilities during the height of the pandemic and improved health management at an individual level. Home testing allowed people to evaluate individual events and spontaneous action, contributing to the interruption of transmission and eventually giving back a touch of security and freedom to the individual.

Another key application of LFAs and also an example of a test strip that can be purchased over-the-counter is the pregnancy test. The first one-step pregnancy test was introduced in 1988 by Clearblue which was a urine dipstick.<sup>[67-69]</sup> Depending on the hCG (human chorionic gonadotropin) hormone level which rises at the beginning of pregnancy, the appearance of either one or two colored lines encodes for either not pregnant or pregnant,

respectively. It was not only a technical advance but also a social revolution for women as it became available at a time when women were fighting against the male-dominated medical establishment.<sup>[70]</sup> With a minimum of inconvenience and without visiting the doctor, thus revealing their sexual activity, women could obtain instantaneous results and certainty. Home testing granted women more control while protecting their privacy. Although self-diagnosis can potentially bear dangers and risks, the two described examples have proven a good and important alternative or supplement in certain situations, moving triage out of the doctor's office.

The LFA technology is based on molecular interactions such as antigen-antibody interactions (**Ch. 2.3**). Upon binding, the antigen-antibody conjugate is immobilized on the paper-based strip and visualized by so called labels. Typically, the labels consist of AuNPs which appear in a red line on the test strip. As described above, Au colloids are the most popular label since they are stable in liquid as well as in dried state. Au colloids have been used for a long time since they have optical properties that do not need visualizing instruments. Other labels such as fluorescent dyes and quantum dots cannot be detected directly by the naked eye and therefore require dedicated reading devices. Latex beads can be produced in multiple colors; therefore, they can be applied in multiplex assays. Yet, multiplex assays had no lasting commercial success so far compared to single-analyte assays. The technological challenges involve cross-reactivity with related proteins and readouts that are more complex. The LFA technology is still a hot topic in current research aiming at more efficient performances.<sup>[71-73]</sup> This is due to the advances made in nanotechnology, driving creativity to find new strategies to continuously raise the quality of rapid tests. In general, the quality of a LFA is indicated by its sensitivity and selectivity. On a molecular level high specificity means that binding events must happen only between the target and its specific binding partner(s) without interference by other sample components. A blood sample, nasal swab, or saliva contains many other molecules which may interfere with the target interaction and lower the specificity. Right assay conditions, choice of molecule interaction, and engineered affinity can raise specificity. A high specificity leads to less false-positive results.

The sensitivity of LFAs is limited by the  $K_d$  (dissociation constant), which describes the affinity between the two interacting molecules, and by the colorimetric read-out. Therefore, increasing either affinity or read-out signal could lead to a better sensitivity. High sensitivity leads to less false-negative results. The integration of multivalency, a higher number of

binding sites, could address this challenge. However, the complexity of such a system has yet hampered its application. A problem that arises from engineering the tests for higher sensitivity is a potential decrease in specificity since stronger binding and high number of binding events can increase “false” binding.

Since the read-out signal originates from plasmons, strategies for creating strong plasmons for a more sensitive visual read out are required. This could be met by the use of a metal which supports stronger plasmons in the visible range. It is known that the strongest plasmons in the visible range are supported by Ag.<sup>[74]</sup> However, this metal has not yet been used as a label in rapid tests since Au displays a more stable alternative. One could think of using other metals, e.g. aluminum. Once passivated, aluminum is a stable metal (aluminum foil does not oxidize) which supports strong plasmons in the UV. However, this requires specialized readers. Another crucial problem is the limited availability of aluminum nanoparticles (Al NPs).

The sensitivity of human eyes is highest for wavelengths  $\sim 530 - 580$  nm, i.e. people see the color green better than any other color. Therefore, green NPs are favorable for increasing the read-out sensitivity. Since the target molecules usually present a limited number of binding sites to bind NPs, another strategy leading to an enhanced read-out signal involves raising the number of NPs per target molecule.

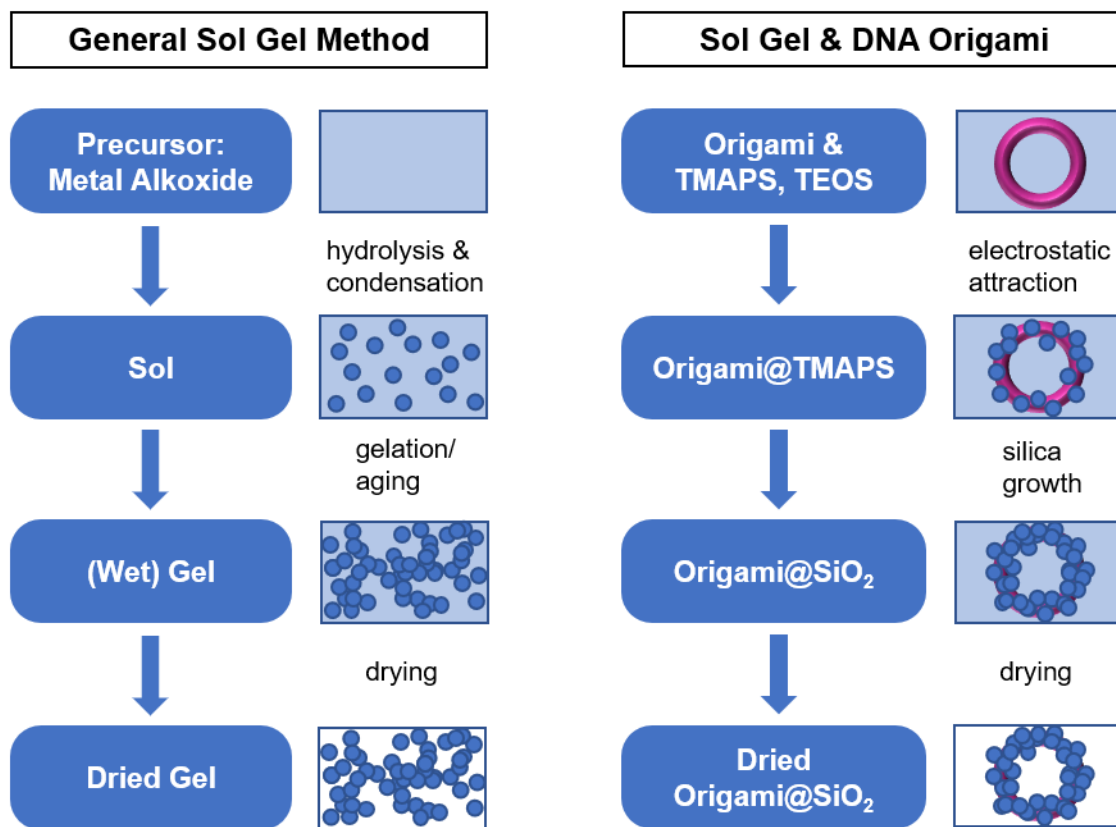
In sum, generating stronger plasmons and green-shifting them, having multiple labels bound per target, increasing binding affinity to promote desired binding, and eliminating false binding will lead to the most efficient performance of LFAs. The practical implementation and feasibility of these aspects are currently studied, with focus on increasing number of NPs bound per target. Since origami nanostructures can be used to bind multiple NPs, dyes and proteins with tunable binding sites, we used a DNA origami structure as a connector between one target and a multitude of NPs. Initial approaches and advances achieved during this work are presented in **Ch. 5**. Owing to the DNA origami structures the number of labels could be increased which lead to a signal amplification at constant target concentration. Technologically, we are stepping towards real-life applications of DNA origami structures in rapid tests. The integration of an engineered function facilitates the response to complex situations, potentially having a great impact on health care and social life.



## 2 Theoretical Background & Methodology

### 2.1 Sol Gel Chemistry

The sol-gel method is widely used for the fabrication of metal oxides, especially the oxides of silicon (silica,  $\text{SiO}_2$ ) and titanium. The process involves converting a molecular precursor (usually metal alkoxide) into a sol (colloidal solution). The sol gradually evolves into a gel containing metal oxides with morphologies ranging from discrete particles to continuous networks (**Figure 3**, left).



**Figure 3.** Sol gel process applied on DNA origami (e.g. ring). Left: the sol gel method involves the formation of a sol (colloidal solution) that gradually converts into a gel based on a continuous network of individual colloids grown together. Through evaporation of the liquid phase, a light weight material with low density and high surface area is obtained. Right: TMAPS is a special precursor used to associate with DNA. The silica growth is constrained to the origami surface. The structural integrity of the origami is preserved upon drying.

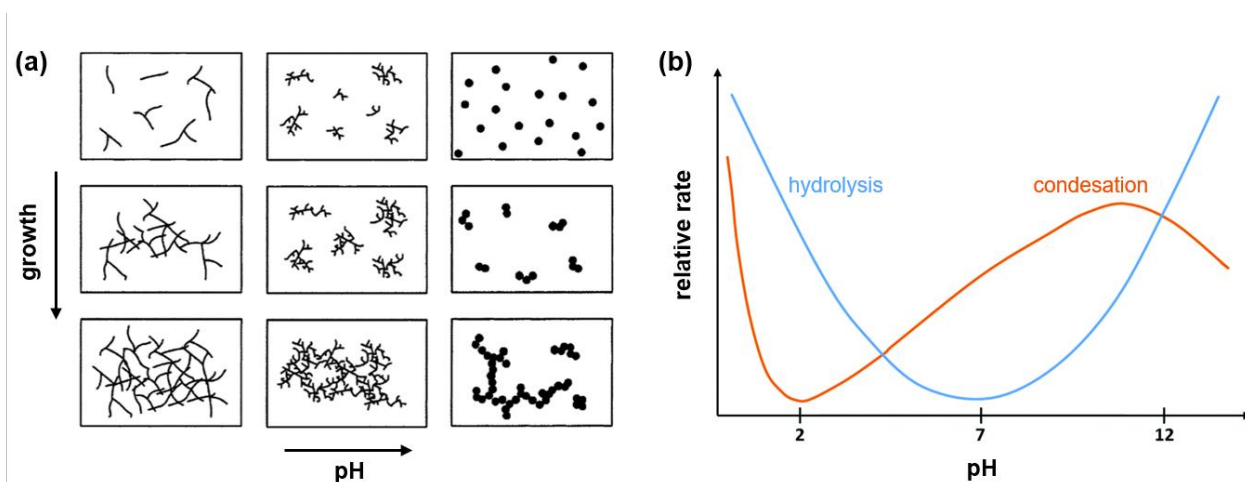
The sol-gel method can be combined with the DNA origami method<sup>[75]</sup> (**Figure 3**, right) to produce more complex silica structures depending on the shape of the DNA origami. The

silica growth on the origami surface provides mechanical support as well as chemical and thermal stability. The molecular growth process and association of silica and DNA nanostructures are described below.

## The Stöber Process

The most widely used sol gel process to produce silica structures was reported by Werner Stöber in 1968.<sup>[76]</sup> Usually, alkoxy silanes such as tetraethyl orthosilicate (TEOS) are hydrolyzed in alcohol (typically methanol or ethanol) in the presence of a catalyst, e.g. ammonia or hydrochloric acid.

The ethoxy groups of TEOS are hydrolyzed which produces ethanol and a mixture of ethoxysilanols ( $\text{Si}(\text{OEt})_3(\text{OH})$ ,  $\text{Si}(\text{OEt})_2(\text{OH})_2$ ,  $\text{Si}(\text{OEt})(\text{OH})_3$ , Et = ethyl) and silicic acid ( $\text{Si}(\text{OH})_4$ ) which can then condense amongst each other with loss of ethanol or water (*cf.* alcohol and water condensation in **Ch. 6.1 Scheme S1**). The condensation reactions lead to crosslinking and the formation of a silica network.

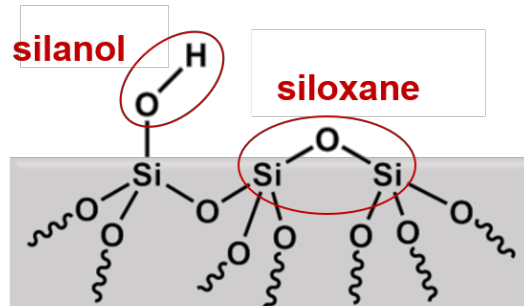


**Figure 4.** (a) pH-dependency of silica growth.<sup>[77]</sup> (b) Hydrolysis and condensation rate at different pH values.<sup>[78-79]</sup> Adapted with permission.

The Stöber method can be performed at either acidic or basic condition. Strongly acidic values (pH 2 – 3) induce a slow gelation which is ideal for the formation of an extended network while basic values (pH 8 – 9) induce a fast gelation, ideal for the formation of NPs (**Figure 4a**). The pH adjustment is essential since at neutral condition the reaction rate is low (**Figure 4b**). Although the condensation rate is higher than the hydrolysis rate at pH 7, an initial hydrolysis step must precede to enable the following condensation. Therefore, the reaction kinetic at pH 7 is determined by the hydrolysis rate.

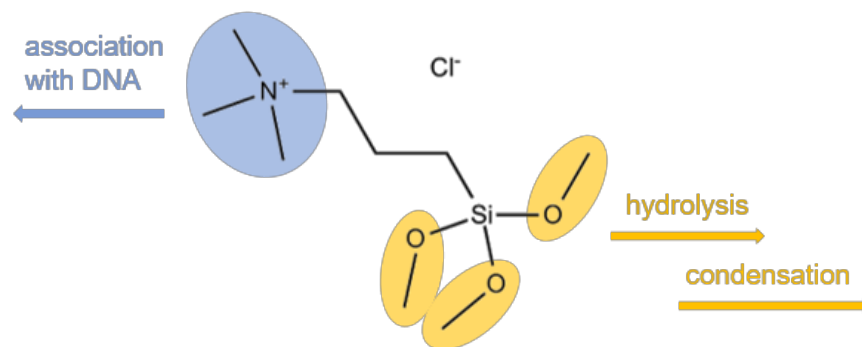
## Silica Association with DNA Origami

Silica comprises an amorphous network of  $\text{SiO}_4$  tetrahedra in the bulk and siloxane ( $\text{Si-O-Si}$ ) and silanol ( $\text{Si-OH}$ ) groups at the surface (**Figure 5**). The silanol groups are deprotonated ( $\text{Si-O}^-$ ) at pH 2 – 14 leading to a net negative charge.



**Figure 5. Silica surface groups.**

Hence, DNA and silica repel each other due to their charge. To facilitate an association between the two, a “co-structure directing agent” was proposed: N-trimethoxysilylpropyl-NNN-trimethylammonium chloride (TMAPS).<sup>[80]</sup> TMAPS is not a commonly used silane in the sol gel process; however, its chemical structure allows for an electrostatic interaction of the quaternary ammonium group and the phosphate group of the DNA backbone while the methoxy groups can undergo hydrolyzation and subsequent condensation with TEOS (**Figure 6**).

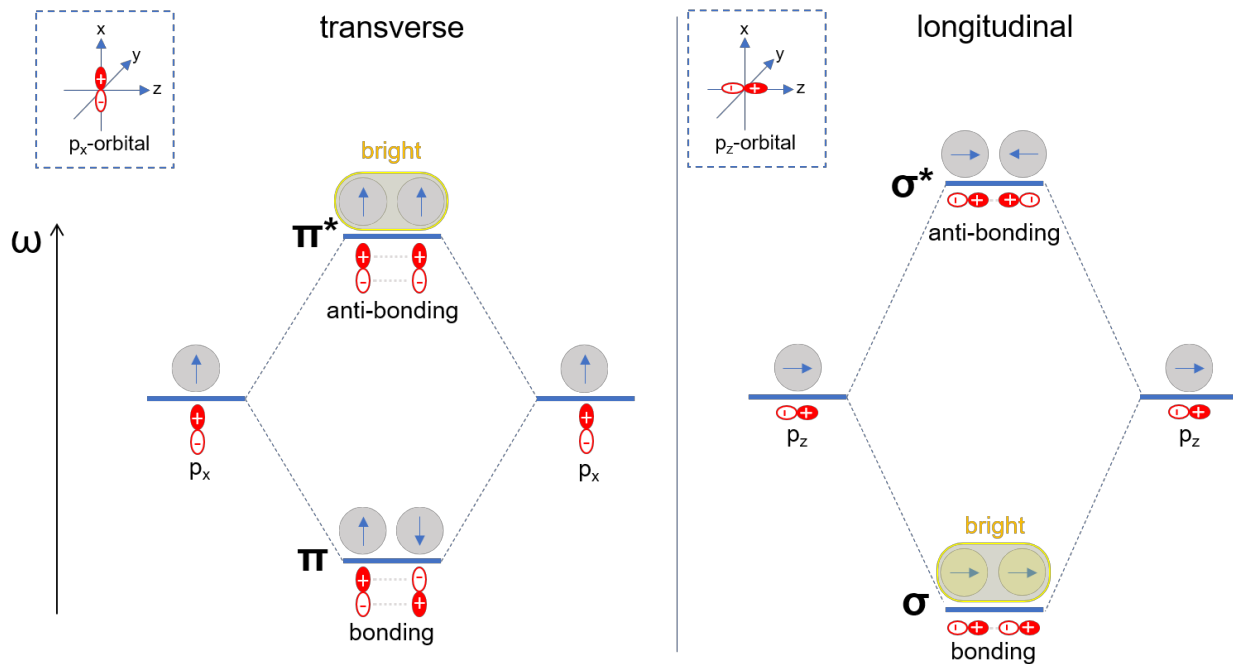


**Figure 6. N-trimethoxysilylpropyl-NNN-trimethylammonium chloride (TMAPS).**

## 2.2 Plasmon Hybridization Model

The plasmon hybridization model was proposed in 2003 by N. Halas *et al.*<sup>[46]</sup> The model describes the plasmon coupling in a similar way to the hybridization of atomic orbitals. The orbital hybridization model was developed in 1931 by L. Pauling to explain molecular geometries of simple molecules such as methane. Both the plasmon and the orbital hybridization model are quantum mechanical approaches that are used to calculate the electron's energy state. Therefore, the plasmon coupling between two metal NPs is viewed as the hybridization of their individual plasmon modes. The theory shows how to classify the hybridized plasmon modes and helps to predict their corresponding energy. The plasmon interaction leads to an energetic splitting of the single particle plasmon modes. Hybridization either in-phase or out-of-phase leads to the formation of a (low energy) bonding and a (high energy) anti-bonding plasmon mode, respectively.

The plasmon energy levels for a dimer of spherical particles can be depicted in a hybridization model diagram (**Figure 7**). Under the excitation of light polarized along the axis of the dimer (longitudinal polarization), the dipoles of the bonding mode  $\sigma$  are arranged parallel ( $\rightarrow \rightarrow$ ) to each other, therefore moving in phase with respect to each other (**Figure 7**, right). This gives rise to a finite total dipole moment unequal to zero. In the anti-bonding mode  $\sigma^*$ , the dipoles are arranged in an anti-parallel configuration ( $\rightarrow \leftarrow$ ) and therefore move out of phase with respect to each other, leading to an extinction of the total dipole moment. The far-field optical properties of the dimer are governed by the modes with a net dipole; therefore, only the  $\sigma$ -mode is 'bright' while the  $\sigma^*$ -mode is 'dark'. In other words, the charge oscillation is canceled out in the anti-bonding mode and without that oscillation a coupled state with a photon cannot arise. Therefore, only the bonding mode can couple with external light leading to a red-shift of the LSPR frequency. Due to the concentration of light within the dimer junction, the electric field is largely enhanced in that spot.



**Figure 7. Hybridization diagram for transverse polarization (left), and longitudinal polarization (right). Single particle modes hybridize to form collective plasmon modes by splitting in low-energy ( $\sigma$ ,  $\pi$ ) and high-energy modes ( $\sigma^*$ ,  $\pi^*$ ); the bright modes  $\sigma$  and  $\pi^*$  have a net dipole moment.**

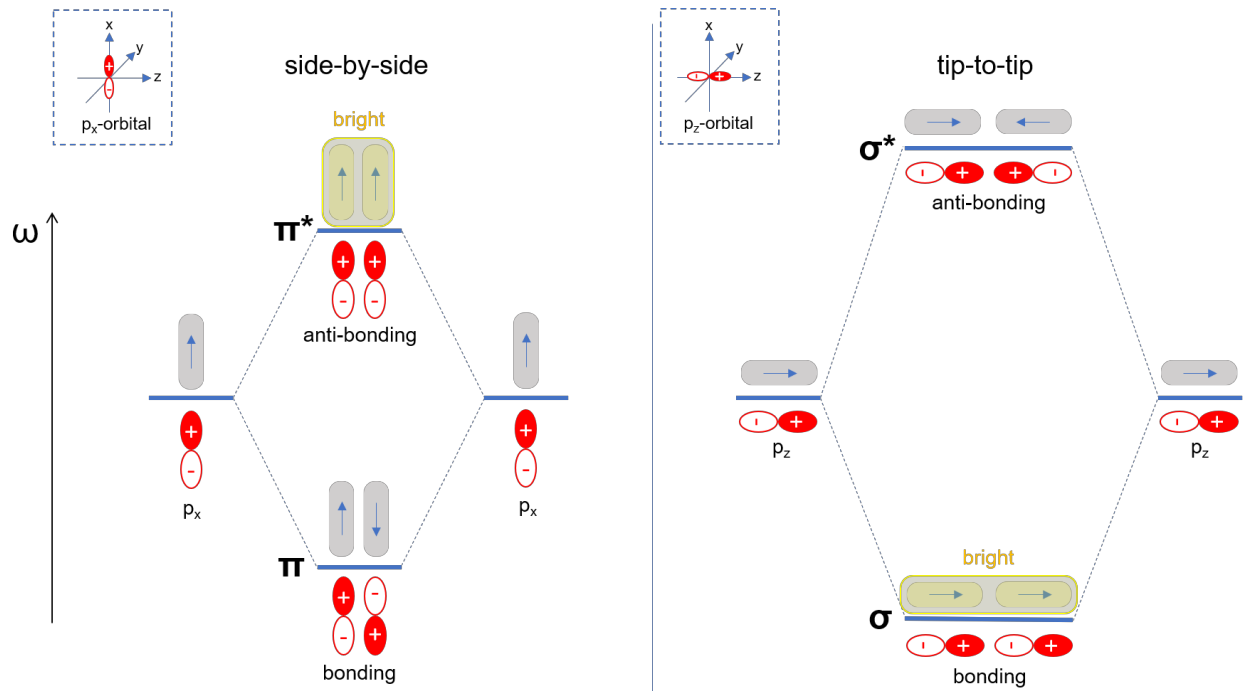
In case of the polarization being perpendicular to the dimer axis (transverse polarization), the situation reverses meaning that the dipoles are anti-parallel ( $\uparrow\downarrow$ ; move out-of-phase) in the bonding mode  $\pi$  and parallel ( $\uparrow\uparrow$ ; move in-phase) in the anti-bonding mode  $\pi^*$  (**Figure 7**, left). Since only the  $\pi^*$ -mode has a finite total dipole moment and can be excited by far-field light, it is bright while the  $\pi$ -mode is dark. Therefore, the plasmon interaction leads to a blue shift of the LSPR frequency.

The frequency splitting is due to electrostatic interaction between the NPs. In the high-energy mode, the dimer dipoles interact repulsively and therefore have an increased restoring force of the charge oscillation which explains the higher resonant frequency compared to a single particle. On the contrary, the low-energy mode supports an attractive interaction which has a lower resonant frequency as a result. The higher energetic splitting of the longitudinal polarization compared to the transverse polarization is based on the closer proximity of the charge oscillation in this direction.

When the geometrical shape of a particle deviates from a sphere, the plasmon resonance are no longer equivalent for all polarization directions (i.e. they become anisotropic). By virtue of the assembly of two AuNRs in close proximity to each other, their plasmon

resonance modes can couple and form collective plasmon modes. The strength of plasmon coupling increases with increasing aspect ratio of the AuNRs.<sup>[81]</sup> Further, it depends on the same structural parameters as for spherical NPs, e.g. the coupling strength increases with decreasing distance between the AuNRs, and increasing number of interacting AuNRs.

The coupling of the longitudinal modes of two AuNRs in the side-by-side assembly is described in a way very similar to the hybridization of  $p_x$ -orbitals, while the tip-to-tip assembly resembles the overlap of  $p_z$ -orbitals in molecular orbital theory (**Figure 8**).<sup>[82]</sup> Hence, regarding the side-by-side assembly, the hybridization of the LSPRs leads to the formation of a bonding mode  $\pi$  and an anti-bonding mode  $\pi^*$ . In case of the tip-to-tip assembly, the bonding and anti-bonding modes are referred to as  $\sigma$  and  $\sigma^*$ . (A bonding state is understood to be more stable than the anti-bonding state from an energetic perspective.) The  $\sigma$ -interaction is stronger than the  $\pi$ -interaction. A stronger LSPR interaction results in a larger energetic splitting; hence, the  $\sigma$ - $\sigma^*$ - energy separation is larger than the one of  $\pi$ - $\pi^*$ .



**Figure 8.** The plasmon coupling in metal NR dimers described by the hybridization model showing the basic picture of the coupled longitudinal plasmon modes of tip-to-tip and side-by-side assembled NRs. The coupling between the transverse modes is described in an analogous way.

As only the modes with a net dipole moment can be excited, the  $\pi^*$ - and the  $\sigma$ -mode are “bright”, while the others are “dark”. As a result, the side-by-side assembly gives rise to a shift towards higher LSPR compared to a single NR, whereas for the tip-to-tip assembly the LSPR is red-shifted. The plasmon coupling between the transverse modes is very weak but can be described in a similar way to the longitudinal modes.<sup>[83]</sup> By increasing the distance between the NRs, bonding and anti-bonding mode converge as the electromagnetic field interaction becomes weaker. When the gap distance becomes smaller than 0.5 nm, the quantum tunneling effect should be taken into account. When the two nanorods get in contact, the coupled bonding plasmon mode undergoes an abrupt large blueshift, and a new charge-transfer plasmon mode, representative to the newly elongated nanorods, appears far redshifted.<sup>[83]</sup>

## 2.3 Rapid Test / Lateral Flow Assay

A rapid test (lateral flow (immuno)assay (LFA, LFIA)) is a simple cellulose-based device which gives information about the content of a sample. It confirms the presence or absence of a target analyte through a visual readout. LFAs are applied, for example, as a tool for environmental monitoring, and quality control of products and raw materials. Further, they are used in clinical settings, e.g. as medical tests such as the home pregnancy test and the SARS-CoV-2 antigen test. They are designed for detecting a large variety of analytes including cardiac and tumor markers, as well as illegal drugs such as cocaine, opiates, cannabinoids, and methamphetamines.<sup>[84-85]</sup> Samples can be body fluids (e.g. saliva or urine) or finger-prick blood. Rapid tests are easy to handle, cost-effective, portable, do not require laboratory resources, and deliver results after only 5 – 15 minutes. Therefore, they are assigned to point-of-care (POC) diagnostics. POC tests include any type of tests that are carried out in the presence of the patient or by the patient himself without the need to send a sample to a laboratory.

A rapid test consists of a test strip which is often encased in a plastic cassette (**Figure 9**). The test strip consists of a porous nitrocellulose membrane which has three different cellulose/glass fiber pads attached: the absorption pad, conjugation pad, and the waste pad (details below). These components are mounted over a flexible backing card.

Once a sample droplet is applied to the absorption pad, the fluid migrates through each component by capillary flow. The reagents involved in the assay are dispersed and immobilized on the strip beforehand. During the flow process, specific interactions of immunoreagents are actuated which results in the staining of certain zones (test line, control line). The presence of the target is indicated by the test line while the control line confirms that the test is working properly. Since the whole flow process involves a separation of molecules which is based on immunochemical reactions and on differences in migration speed, LFA is defined as an immunochromatographic technique.



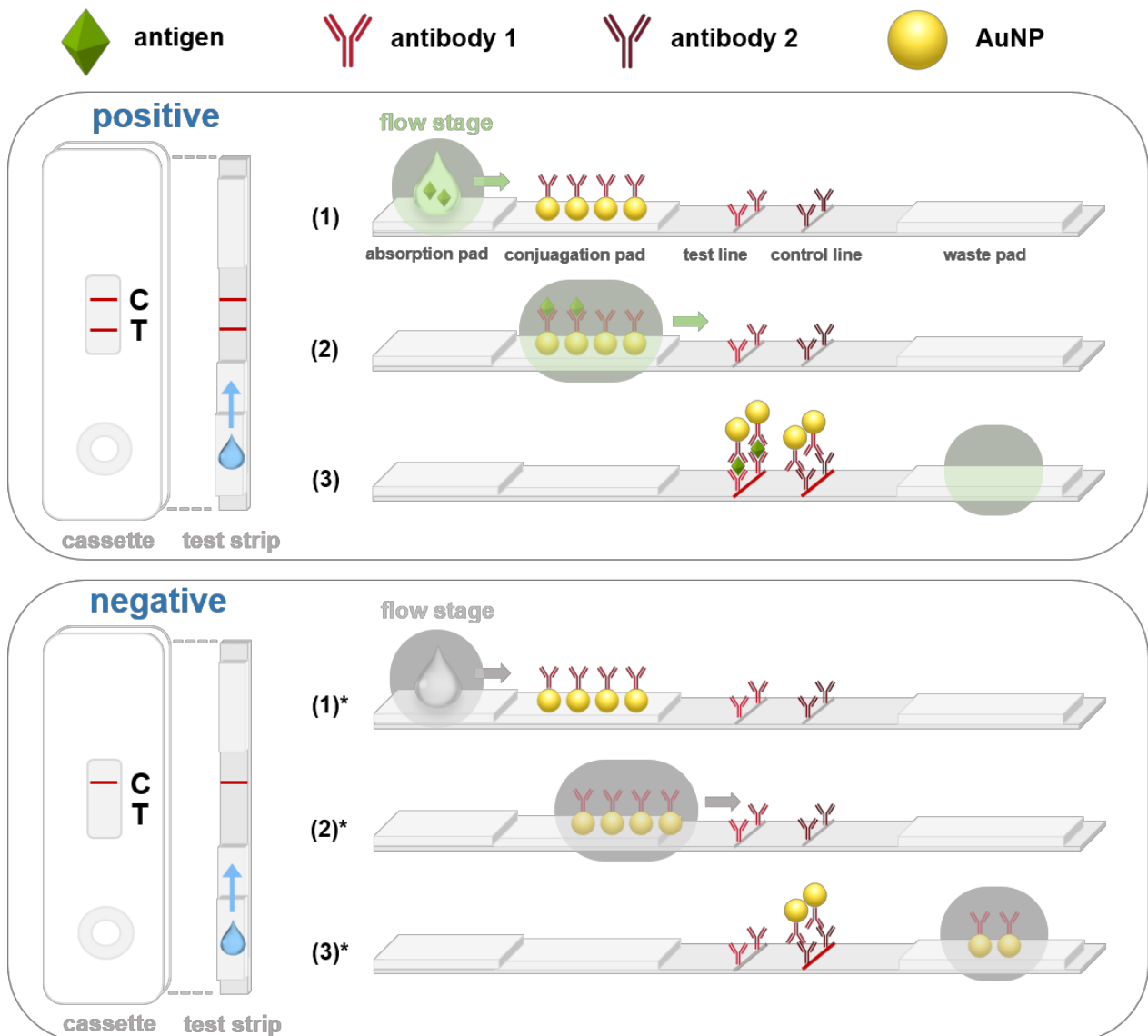


Figure 9. Lateral flow immunoassay (antigen test as example) showing positive (top) and negative result (bottom).

(1) Positive sample is absorbed and migrates through the strip by capillary flow.

(2) Antigen-target binds to an antibody 1 – gold nanoparticle (AuNP) conjugate.

(3) Test line: Antigen – antibody 1 – AuNP conjugates binds specifically to antibodies of type 1 that has been pre-immobilized. Control line: Antibody 1 – AuNP conjugates bind non-specifically to antibodies of type 2 that have been pre-immobilized. (Antibodies 1 and 2 interact non-specifically and independently from presence and absence of antigen.)

(1)\* Negative sample is absorbed and migrates through the strip. There are no antigen-targets that could interact with antibody 1 – AuNP conjugates.

**(2)\* Antibody 1 – AuNP conjugates encounters antibodies of type 1 that are pre-immobilized on strip.**

**(3)\* Test line: Antibody 1 – AuNP conjugates pass test line without binding to antibodies of type 1. There is no interaction between two antibodies of type 1 in absence of an antigen. Control line: Antibody 1 – AuNP conjugates bind non-specifically to antibodies of type 2 that has been pre-immobilized on strip. Waste pad collects unbound antibody 1 – AuNP conjugates.**

Details of the flow process are depicted in **Figure 9**. The absorption pad acts as the first stage of the flow process. It absorbs the sample and ensures a consistent and controlled flow. The conjugation pad contains labeled biorecognition molecules, e.g. antibodies, which (“recognize”) interact with specific target molecules of the sample, e.g. antigens. For example, a SARS-CoV-2 antigen test has anti-SARS-CoV-2 antibodies, and a hCG antigen test (pregnancy test) has anti-hCG antibodies adsorbed to the conjugation pad which interact with their specific antigens. Once the fluid reaches the conjugation pad, specific immunoreactions are initiated, e.g. target-antigens interact with labeled antibodies (**Figure 9 (2)**). When the target molecules are not present in the sample, there will be no interaction with the labeled recognition molecules (**Figure 9 (2)\***). Gold nanoparticles (AuNPs) with a diameter of 40 nm are typically used as labels. Other labels include carbon or colored latex nanoparticles, magnetic beads, and colored polystyrene beads. Due to the AuNPs, the liquid turns into a slightly reddish color after it has passed the conjugation pad. After the conjugation process, the conjugates are carried with the flow into the nitrocellulose membrane until they hit the test zone. At the test zone, “capture” antibodies have been pre-immobilized and fixed to the membrane. Once the antigen-antibody-AuNP conjugates bind to the pre-immobilized recognition molecules, they will be captured at the test zone (**Figure 9 (3)**). Due to the AuNP labels, the test zone turns red and a red line appears. The intensity of the red line varies depending on the quantity of the target. When the antigen-target is not present, the test zone will not turn red since the labeled antibodies pass that zone without being captured (**Figure 9 (3)\***). The next zone of the membrane is the control zone which indicate that the sample has sufficiently migrated. At the control zone, antibodies have been pre-immobilized which are different from the ones at the test zone. These antibodies bind the labelled antibodies from the conjugation pad since there is a non-specific interaction between them, the C-zone antibodies and the labeled antibodies. The binding is independent from the presence of the antigen. Hence, the

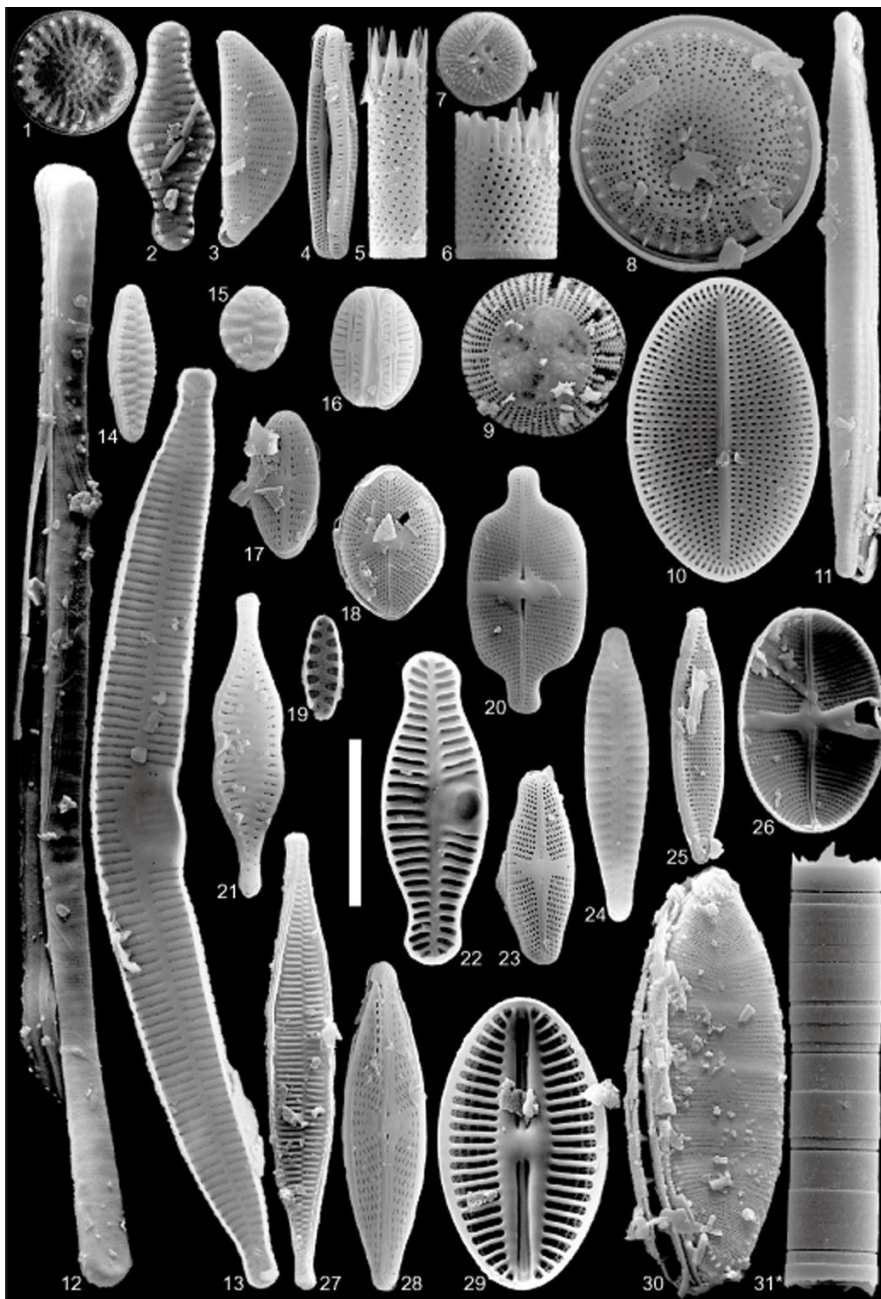
control line turns red for both a negative as well as a positive sample. The last stage of the flow process is the waste pad which collects remaining fluid and molecules. The waste pad also helps maintaining the flow rate and prevents back flow.

### 3 DNA Origami-Directed Silica Mineralization

Silica nanostructures are formed in nature through a biomineralization process. Biominerals are organic-inorganic hybrid materials with exceptional structural features (**Figure 10**). They are synthesized for different purposes including structural stability, rigidity, protection and defense. The structure is precisely controlled over several hierarchical orders from nano to micro scale resulting in complex architectures.

#### **“Form is function”**

Diatoms, for example, are aquatic organisms which use silicates to stiffen and protect their tissue providing them with resilience for viability. The silica walls have openings and slits for the diatom to interact with its environment. For example, light-sensitive species reduce their exposure through elaborate patterning. There are hundreds of thousands of diatoms species with distinct silica patterns providing multiple functionalities.



**Figure 10.** Scanning electron micrographs of most of the dominant diatom species in the investigated sediment core of Lake Sokoch. Scale bar represents 10  $\mu\text{m}$  for all of the shown species, except for number 31 marked with an asterisk. For this single species, the scale bar represents 100  $\mu\text{m}$ .<sup>[86]</sup> Adapted with permission.

Since biomineralization has been a process for more than 500 million years, it has been highly optimized through evolution. Therefore, mimicking the biomineralization process is a great motivation for researchers in the field of biomimetic materials chemistry. Although the naturally occurring structures are still extremely difficult to replicate, they give an inspiration to follow the biomimetic approach. Understanding and abstracting the

mechanisms allows us to design and fabricate new architectures with defined physical properties. Pioneering work in biomimetic mineralization was made especially by Seiji Shinkai<sup>[6]</sup>, Stephen Mann<sup>[87]</sup>, Jeffrey Brinker<sup>[88]</sup>, and Shunai Che<sup>[89]</sup>.

Examples for biomimetic nanostructures are DNA-silica fibers, multi-helical DNA-silica fibers, helical DNA-silica impellers, polypeptide-silica spheres, polypeptide-silica fibers, chiral peptide-silica complex with ordered lamellar structure, PLL-silica platelets, cellulose-silica with birefringence patterns, chiral cellulose-silica films, virus (TMV)-silica showing hexagonally ordered mesoporous structure, *pili*-silica lattices.<sup>[90]</sup> From today's point of view the shapes were simple and fairly irregular. Yet, there is a limited selection of template patterns used for mineralization and hence a lack of nanoscopic inorganic material with special structural features.

DNA nanotechnology provides new opportunities for biomimetic materials chemistry. Especially, the DNA origami technique gives access to a plethora of structures in 1, 2, and 3 dimensions. DNA origami structures are customized and provide an unlimited degree of structural complexity which makes them ideal candidates to be used as templates for defining new silica patterns.

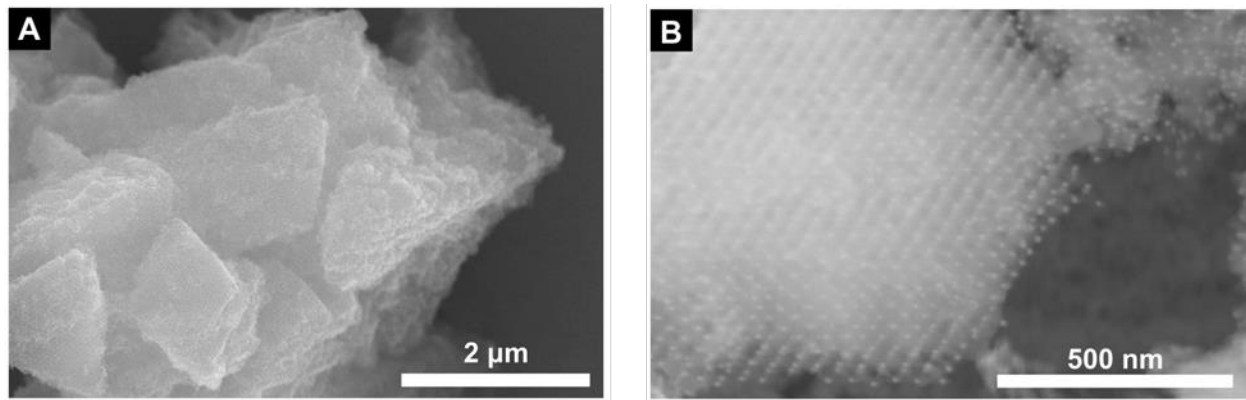
At the same time, the silica mineralization provides stability and rigidity for the DNA origami nanostructures. Without the silica protection the DNA origami structures would decompose once they were exposed to extreme conditions such as heat, low/high pH, and low salt buffers. Further, the nanostructures are prone to deformation and loss of dimensionality upon drying. Especially, 3-dimensional DNA origami lattices are very delicate and fragile. For example, they would collapse under their weight and mechanical stress upon transition to the dry state. Hence, with respect to both perspectives, DNA origami mineralization does not only raise structural variety but also stability, integrity, functionality, and applicability. The work presented here is interdisciplinary; it provides an approach to solving challenges in biomimetic chemistry as well as in DNA nanotechnology.

#### **DNA Origami Meets Silica Mineralization**

The main goal of this work was to transcribe DNA origami shapes into silica structures by templating and directing the silica growth. The first DNA origami-templated silica structures (immobilized on a surface) were reported in July 2018 by the group of Chunhai Fan.<sup>[7]</sup> The work presented in this dissertation was published shortly after, in November

of the same year, presenting origami-silica structures which are dispersed in water. In the so-called sol gel process to grow silica, silanes are used as precursor. TMAPS (N-trimethoxysilylpropyl-NNN-trimethylammonium chloride) is not a commonly used precursor. However, it is used here as it is important for the association with DNA in order to transcribe the origami shape. The approach of using TMAPS as a linking molecule between the DNA-silica interface was first reported in 2003 by Shunai Che in the context of making silica structures using single stranded DNA as templates.<sup>[80]</sup> In their publication the crucial role of a “co-structure-directing agent” was demonstrated since DNA and silica repel each other due to their opposite charge. Three years later, in 2006, the DNA origami technique was introduced for folding single stranded DNA into arbitrary shapes. Using DNA origami one can access any desired 1, 2 and 3D shape with varying sizes. However, it took more than one decade for the silica mineralization process and DNA origami to meet each other. This could be due to difficulties in growing silica in a controlled manner and exclusively on the DNA origami surface which is highly dependent on parameters such as temperature, amount of precursor, pH and mixing speed. Synthesis and growth conditions need to be precisely adjusted to overcome random silica growth and to obtain a smooth silica layer. Moreover, better research exchange might have promoted the encounter of both disciplines.

After the presentation of our interdisciplinary approach, various publications followed introducing new silica patterns and objects including highly ordered, distinct, and elaborate crystalline structures.<sup>[9-11, 14-16]</sup> Especially fragile and delicate DNA crystals benefit from the rigid silica support layer (**Figure 11**). Two further publications followed presenting calcium phosphate mineralization on DNA origami.<sup>[13, 17]</sup> The calcium phosphate shell can provide rigidity and support as well, however, it has a higher degree of unevenness and less stability against extreme pH and heat.



**Figure 11. Structural and elemental characterization of silica-AuNP replica lattice by electron microscopy. (A) Scanning electron microscopy (SEM) images of grains of SiO<sub>2</sub>-coated FCC DNA-AuNP superlattice. (B) High-resolution SEM reveals that each grain is a monodomain with sharply terminated grain boundaries and dihedral angles corresponding to the symmetry of the lattice.<sup>[16]</sup> Adapted with permission.**

The silica encapsulation of DNA origami provides an effective experimental method for the controllable fabrication of functional inorganic materials. As of yet, potential applications of such silica structures have not been exploited to the full. The biomaterials' structure is as yet superior to artificially produced ones. It results from a very specific interaction at the organic-inorganic interface involving specific proteins. Therefore, the development of next generation biomimetic systems may involve these kinds of proteins. Further, as presented by our method the DNA origami mineralization method helps overcoming stability and deformation issues of soft DNA structures. Prospectively, using this method, the structure variety of DNA origami will shift towards stable, and at the same time, intricate and delicate structures such as 3D lattices with even thinner struts and larger cavities.



## 3.1 Associated Publication 1



## DNA Nanotechnology

International Edition: DOI: 10.1002/anie.201811323

German Edition: DOI: 10.1002/ange.201811323

## DNA-Origami-Templated Silica Growth by Sol-Gel Chemistry

Linh Nguyen, Markus Döblinger, Tim Liedl, and Amelie Heuer-Jungemann\*

**Abstract:** Improving the stability of DNA origami structures with respect to thermal, chemical, and mechanical demands will be essential to fully explore the real-life applicability of DNA nanotechnology. Here we present a strategy to increase the mechanical resilience of individual DNA origami objects and 3D DNA origami crystals in solution as well as in the dry state. By encapsulating DNA origami in a protective silica shell using sol-gel chemistry, all the objects maintain their structural integrity. This allowed for a detailed structural analysis of the crystals in a dry state, thereby revealing their true 3D shape without lattice deformation and drying-induced collapse. Analysis by energy-dispersive X-ray spectroscopy showed a uniform silica coating whose thickness could be controlled through the precursor concentrations and reaction time. This strategy thus facilitates shape-controlled bottom-up synthesis of designable biomimetic silica structures through transcription from DNA origami.

DNA nanotechnology allows for the fabrication of nanometer-sized objects with high precision and selective addressability as a result of the programmable hybridization of complementary DNA strands.<sup>[1]</sup> In particular, the introduction of the DNA origami technique<sup>[2]</sup> has resulted in a plethora of objects of different shapes, sizes, and complexities with nanoscale control, many of which have been site-specifically modified with a variety of functional moieties such as proteins or nanoparticles.<sup>[3–9]</sup> Potential fields of applications of these DNA nanoobjects include biophysics, plasmonic metamaterials,<sup>[10,11]</sup> nanomedicine,<sup>[12,13]</sup> and material sciences. Compared to many other biomolecules, such as proteins or RNA, DNA displays high chemical stability and a very simple relationship between complementary sequence and double-helical structure, which is the basis of DNA self-assembly.<sup>[14]</sup> Nevertheless, DNA is highly susceptible to hydrolysis, depurination, depyrimidination, oxidation, alkylation, and degradation by nucleases.<sup>[14]</sup> Moreover, DNA origami structures often require high salt concentrations and ambient temperatures to maintain their structural integrity, which in turn reduces their potential for real-life applications. A severe drawback for material applications potentially operating in

air or vacuum is the necessity of aqueous surroundings to maintain structural rigidity. Therefore, new methods to improve the stability of DNA origami structures are required. Some recently developed strategies to address this issue include cross-linking strategies,<sup>[15–17]</sup> coating origami structures with a lipid bilayer, similar to enveloped viruses,<sup>[18]</sup> or a cationic poly(ethylene glycol)-polylysine block copolymer, which increases their stability with respect to low salt environments or nuclease degradation.<sup>[19]</sup>

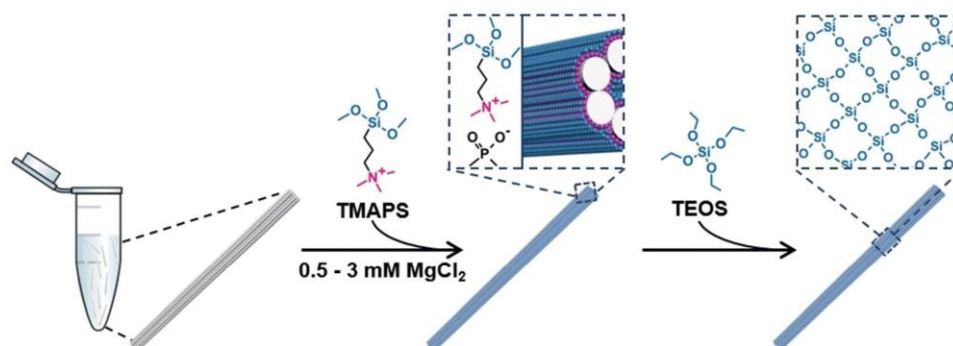
In nature, DNA can be chemically and physically preserved for millennia, as can be seen in fossils, where DNA is hermetically sealed by biomineralization. Such a process is also often used by organisms to stiffen their tissues, for example, diatoms or corals. The most common materials used in biomineralization processes include calcium compounds (e.g. CaCO<sub>3</sub>, Ca<sub>3</sub>(PO<sub>4</sub>)<sub>2</sub>) and silica (SiO<sub>2</sub>). Silica exhibits excellent biocompatibility, nontoxicity, thermal stability, as well as chemical inertness and, therefore, has found widespread applications, especially in the form of mesoporous nanoparticles in biomedical research, particularly in targeted drug delivery.<sup>[20–23]</sup> The physicochemical properties of silica have also made it an attractive coating agent for inorganic nanoparticles to achieve water solubility, enhanced stability, and biocompatibility.<sup>[24–28]</sup> Considering these advances, silica is a suitable compound to use for biomaterial encapsulation. There have been reports on the silica encapsulation of large biomolecules such as genomic DNA, polypeptides, viruses, collagen fibers, and yeast cells.<sup>[29]</sup> However, published studies on the silicification of nanometer-sized biomolecules have been extremely rare, presumably as the silica growth in solution must be more precisely and critically controlled. Furthermore, the shapes and geometries of existing nanostructured silica often lack complexity compared to self-assembled biological molecules. Therefore, general strategies are needed for the fabrication of complex, predesigned, and on the nanoscale controllable structures. The use of DNA templates for the growth of silica structures offers a solution to these aspects, since the advantages of straightforward DNA origami design can be combined with the favorable properties of an inorganic material.

Liu et al. recently demonstrated that small DNA origami structures and 2D lattices, when adsorbed onto a surface, can be coated with a silica shell.<sup>[30]</sup> Here we show that single DNA origami objects can also undergo silicification in solution without the need for prior adsorption onto a surface, thereby resulting in highly stable silica-encapsulated structures (origami@SiO<sub>2</sub>) as a result of the inertness and thermal robustness of SiO<sub>2</sub>. Furthermore, we demonstrate that our method can also be applied to large 3D DNA origami crystals,<sup>[31]</sup> where the increased structural rigidity provided by the silica shell allows for more in-depth structural analysis than was previously possible.

[\*] L. Nguyen, Prof. Dr. T. Liedl, Dr. A. Heuer-Jungemann  
Faculty of Physics and Center for NanoScience (CeNS)  
Ludwig-Maximilians-University  
Geschwister-Scholl-Platz 1, 80539 Munich (Germany)  
E-mail: A.Heuerjungemann@physik.lmu.de

Dr. M. Döblinger  
Department of Chemistry and Center for NanoScience (CeNS)  
Ludwig-Maximilians-University  
Butenandtstrasse 5–13, 81377 Munich (Germany)

Supporting information and the ORCID identification numbers for the authors of this article can be found under:  
<https://doi.org/10.1002/anie.201811323>.



**Scheme 1.** Illustration of the strategy for encapsulating DNA origami in silica. The structures are dispersed in solutions containing low concentrations of  $\text{MgCl}_2$  before the addition of TMAPS. After physisorption of the cationic TMAPS head groups to the polyanionic DNA backbone, TEOS is added to promote growth of the silica shell, directed by the DNA origami template.

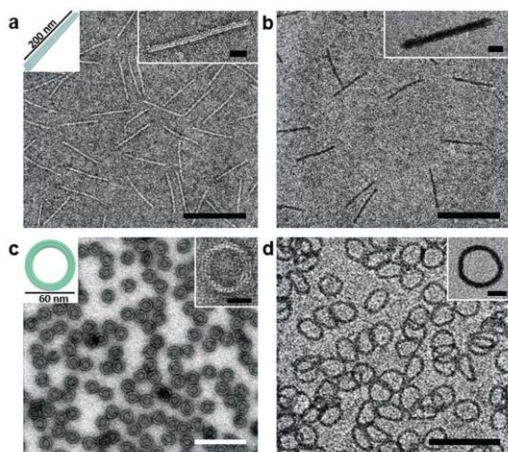
Our synthetic approach is based on the well-known Stöber method for the formation of silica nanostructures.<sup>[32]</sup> The synthesis of silica involves a simple hydrolysis and condensation reaction of silanes (sol-gel reaction). The silanol groups (Si-OH) can then undergo either water or alcohol condensation to form connective siloxane bridges (Si-O-Si) under partial loss of water (see Scheme S1 in the Supporting Information). The silica species involved in this reaction are negatively charged, which poses a problem when considering reactions with anionic DNA. Different methods have emerged to overcome the electrostatic repulsion, for example, making DNA cationic<sup>[33]</sup> or employing a positively charged co-structure directing agent (CSDA), capable of electrostatic attraction to the polyanionic DNA backbone.<sup>[30,34]</sup> Inspired by several literature procedures, we used *N*-trimethoxysilylpropyl-*N,N,N*-trimethylammonium chloride (TMAPS) as a CSDA. This compound contains a quaternary ammonium group that imparts a net positive charge, as well as siloxane groups (illustrated in Scheme 1 in pink and blue, respectively), which present co-condensation sites for the silica precursor tetraethoxy orthosilicate (TEOS), thereby enabling silica growth directly on the DNA structure.

Although this method works well for double-stranded DNA (see Figure S1 for initial studies on salmon testes dsDNA), another factor needs to be considered in the case of DNA origami: To efficiently stabilize DNA origami structures, high concentrations of cations ( $\text{Mg}^{2+}$ ,  $\text{Na}^+$ ) are generally required to shield the repulsive negative charges of neighboring DNA phosphate backbones. This in turn prevents the efficient adsorption of the cationic TMAPS. Liu et al. showed in their study that clusters of prehydrolyzed silica precursors (TMAPS + TEOS) can overcome the electrostatic potential barrier and efficiently adsorb on the phosphate groups ( $\text{PO}_4^{3-}$ ) on the DNA backbone of origami structures.<sup>[50]</sup> On the other hand, it was recently shown that while high cation concentrations are required during origami folding, fully assembled structures can remain stable for some time in buffers containing only very low cation concentrations.<sup>[35]</sup> Taking this into account, we dispersed our origami

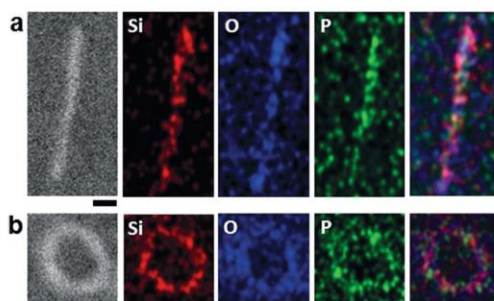
structures—a 14 helix-bundle (HB) and a 14 HB ring (Figures S2 and S3)—in water containing 0.5–3 mM  $\text{MgCl}_2$ . This was found to be a sufficiently high concentration to stabilize the structures, but low enough to still allow efficient adsorption of TMAPS when mixed in a 1:1–1:8 molar ratio (phosphate group/TMAPS) with DNA origami under shaking (see Figures S4 and S5 for optimization studies). This makes the requirement for precluster formation obsolete. In our experiments, the sol-gel condensation occurs upon the addition of TEOS in a 1:26 to 1:104 molar ratio (phosphate group/TEOS) to the origami-TMAPS mixture. After hydrolysis, the silanol groups of TMAPS and TEOS can condense into siloxane bridges.

We furthermore observed that the reaction is very sensitive to movement of the liquid. Control experiments revealed that silica encapsulation was unsuccessful when the sample was shaken for the whole duration of the sol-gel synthesis (see Figure S5). Hence, after shaking the reagents for 15 min to ensure good mixing, the sample was left undisturbed for up to 7 days, after which a silica shell had grown around the origami structures. The thickness of the silica shell can be easily tuned by means of the concentration of the reactants, reaction time, and temperature. By using low concentrations of the silica precursors, the sol-gel reaction kinetics can be slowed down to fine-control the silica growth and thus the final shell thickness (see Figures S6 and S7). Furthermore, since no excess amounts of precursors are available, the nucleation of spurious spherical silica particles in solution can be minimized. The origami@ $\text{SiO}_2$  structures can be isolated by centrifugation and redispersion in water at any time during the silica growth to obtain the final nanostructures with the required thickness of the silica shell. After encapsulation in silica, the origami structures were imaged by transmission electron microscopy (TEM) without additional staining. Whereas bare origami structures required staining with uranyl formate (Figure 1 a,c), the increased contrast provided by the higher electron density of the Si atoms allowed us to identify the structures and evaluate the success of the coating strategy (Figure 1 b,d). To demonstrate the

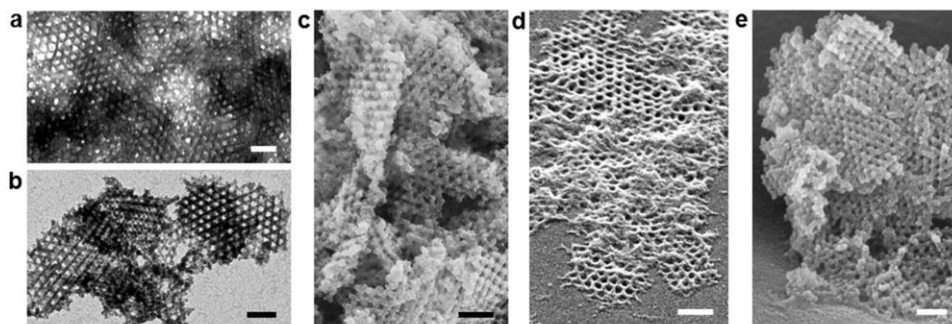




**Figure 1.** TEM images and corresponding schematic representation of the 14 HB rod and the 14 HB ring origami structures. a, c) Bare origami structures (stained with uranyl formate), with high magnification insets. b, d) Origami@SiO<sub>2</sub> without staining. Here, only the DNA and the silica shell provide the contrast. Scale bars are 300 nm for the low magnification images and 30 nm for the insets.



**Figure 2.** STEM and EDX analysis of a) the 14 HB and b) ring origami structures after silica encapsulation. Scale bars are 25 nm. The last image in each row shows an overlay of the Si, O, and P signal maps.



**Figure 3.** Silica growth on DNA origami crystals. a) TEM images of bare crystals, stained with uranyl formate. b) DNA crystals after 4 days of silica growth imaged by TEM without staining. c) Same sample imaged with SEM after a short Au/Pd sputtering. d) 60° tilted view of bare DNA origami crystals. The crystals flatten upon adsorption to the grids. e) 60° tilted view of silica-coated DNA origami crystals. The 3D structure is preserved. Scale bars are 200 nm.

thermal stability of origami@SiO<sub>2</sub>, the structures were heated to 100 °C for 5 min followed by quick cooling on ice. Uncoated DNA origami structures completely dissociated at this temperature, whereas the silica-coated structures remained intact (Figure S8). The stability of origami@SiO<sub>2</sub> with respect to digestion by DNase was tested by incubating them with 1 mg mL<sup>-1</sup> DNase I for 1.5 h at room temperature, after which the structures maintained their structural integrity (Figure S9), unlike uncoated origami structures (Figure S10). The increased stability of the silica-coated structures against high-temperature degradation and DNase digestion further supports the success of our encapsulation strategy. Energy-dispersive X-ray spectroscopy (EDX) mapping in STEM imaging mode was carried out on individual origami@SiO<sub>2</sub> structures to verify the deposition of SiO<sub>2</sub> on the DNA structures and to gain deeper insight into the sample composition. Mappings of both the 14 HB and the ring structure show a uniform Si signal throughout the respective structures, thus indicating a successful silica coating (Figure 2).

We further applied the silica mineralization method to our recently developed 3D DNA origami crystals.<sup>[31]</sup> The silicification of the crystals is an important concept, as the unprotected lattices collapse and deform upon drying (Figure 3) and in salt-free environments, thus preventing applications of such crystals in air and hindering in-depth structural analysis of their true 3D shapes. Encapsulation in silica can provide such stability and thus allows a more detailed structural analysis while preserving the lattice spacing and symmetry.<sup>[36]</sup>

Crystals with rhombohedral lattice geometry were grown through blunt-end stacking interactions of triangular monomers as previously reported (Figure 3 a,c).<sup>[31]</sup> As-grown crystals were then mixed with TMAPS followed by TEOS, as for single origami structures, and left undisturbed for up to 9 days. To monitor the growing thickness of the silica shell, crystals@SiO<sub>2</sub> were analyzed by TEM and SEM after 8 h as well as after 1, 2, 4, 7, and 9 days of silica growth (Figure 3 b,c,e and Figure S11). As expected, silica encapsulation increased the stability of the lattices in the dry state

significantly, which allowed us to clearly visualize the three-dimensional structure by top view and 60° tilt mode SEM imaging (Figure 3c,e and Figure S11). The collapse of bare DNA lattices becomes apparent in Figure 3d. Estimation of the shell thickness by TEM revealed that a thin silica shell was already present after 8 h. The diameter of each 14 HB strut making up the triangular monomer had increased from  $12.1 \pm 1.5$  nm to  $13.5 \pm 1.5$  nm, which indicates a shell thickness of around 0.7 nm. After 1 day, the thickness was already about 1.2 nm, and further increased to about 1.7 nm after 4 days (Figure S11 and Table S1). Analysis of the corresponding SEM images evidenced thicknesses of 1.5, 2.3, and 3.3 nm after 8 h, 1 day, and 4 days, respectively. We attribute this discrepancy to the comparatively low resolution of SEM and the additional deposition of conducting material (Au/Pd mixture), which is necessary to prevent charge accumulation on the samples during SEM imaging. After 7 days, the silica shell reached a thickness that made imaging by TEM difficult due to the high density of silica. Nevertheless, SEM analysis still revealed the overall shape of the encapsulated lattices (Figure S11).

In conclusion, we have presented a universal method to overcome stability issues of DNA origami, which have so far limited their real-life application as 3D materials. In this synthetic approach, DNA origami structures were encapsulated with a protective silica shell through sol-gel chemistry in a silica mineralization process. The chemical, mechanical, and thermal stability of the DNA origami structures was drastically increased by transforming them from the solution to the solid phase. This enabled the DNA origami objects to maintain their structural integrity even in conditions that are generally detrimental, such as low salt concentrations, high temperatures, and the presence of DNase. Our method is not limited to single structures and can even be applied to large 3D DNA origami crystals. The silica mineralization of 3D origami crystals enabled the preservation of their large, otherwise very fragile, structures in a dry state, which also allowed detailed structural analysis of their actual three-dimensionality. Our strategy paves the way to the fabrication of tailored complex silica structures that are otherwise inaccessible through conventional synthetic routes. We believe that our method will contribute to the emergence of highly complex but stable materials that could find application as porous scaffolds for catalysis or as functional coatings with designed optical properties.

### Acknowledgements

This work was supported by the DFG through the SFB grant 1032 (TP A6) and the European Research Council (Grant Agreement No. 336440) for ORCA (Optical Responses Controlled by DNA Assembly) and the Nanosystems Initiative Munich. We would also like to thank Susanne Kempter and Philipp Altpeter for help with TEM and SEM imaging.

### Conflict of interest

The authors declare no conflict of interest.

**Keywords:** 3D DNA origami crystals · DNA nanotechnology · DNA origami · encapsulation · mineralization

**How to cite:** *Angew. Chem. Int. Ed.* **2019**, *58*, 912–916  
*Angew. Chem.* **2019**, *131*, 924–928

- [1] N. C. Seeman, H. F. Sleiman, *Nat. Rev. Mater.* **2018**, *3*, 17068.
- [2] P. W. K. Rothemund, *Nature* **2006**, *440*, 297–302.
- [3] S. M. Douglas, H. Dietz, T. Liedl, B. Högberg, F. Graf, W. M. Shih, *Nature* **2009**, *459*, 414–418.
- [4] A. Kuzyk, R. Schreiber, Z. Y. Fan, G. Pardatscher, E. M. Roller, A. Hoge, F. C. Simmel, A. O. Govorov, T. Liedl, *Nature* **2012**, *483*, 311–314.
- [5] S. M. Douglas, J. J. Chou, W. M. Shih, *Proc. Natl. Acad. Sci. USA* **2007**, *104*, 6644–6648.
- [6] B. Saccà, R. Meyer, M. Erkelenz, K. Kiko, A. Arndt, H. Schroeder, K. S. Rabe, C. M. Niemeyer, *Angew. Chem. Int. Ed.* **2010**, *49*, 9378–9383; *Angew. Chem.* **2010**, *122*, 9568–9573.
- [7] H. Dietz, S. M. Douglas, W. M. Shih, *Science* **2009**, *325*, 725–730.
- [8] W. Liu, M. Tagawa, H. L. Xin, T. Wang, H. Emamy, H. Li, K. G. Yager, F. W. Starr, A. V. Tkachenko, O. Gang, *Science* **2016**, *351*, 582–586.
- [9] S. Loescher, S. Groeër, A. Walther, *Angew. Chem. Int. Ed.* **2018**, *57*, 10436–10448; *Angew. Chem.* **2018**, *130*, 10594–10607.
- [10] A. Kuzyk, R. Jungmann, G. P. Acuna, N. Liu, *ACS Photonics* **2018**, *5*, 1151–1163.
- [11] N. Liu, T. Liedl, *Chem. Rev.* **2018**, *118*, 3032–3053.
- [12] Q. Zhang, Q. Jiang, N. Li, L. R. Dai, Q. Liu, L. L. Song, J. Y. Wang, Y. Q. Li, J. Tian, B. Q. Ding, Y. Du, *ACS Nano* **2014**, *8*, 6633–6643.
- [13] J. B. Liu, L. L. Song, S. L. Liu, Q. Jiang, Q. Liu, N. Li, Z. G. Wang, B. Q. Ding, *Nano Lett.* **2018**, *18*, 3328–3334.
- [14] D. Paunescu, M. Puddu, J. O. B. Soellner, P. R. Stoessel, R. N. Grass, *Nat. Protoc.* **2013**, *8*, 2440–2448.
- [15] A. Rajendran, M. Endo, Y. Katsuda, K. Hidaka, H. Sugiyama, *J. Am. Chem. Soc.* **2011**, *133*, 14488–14491.
- [16] T. Gerling, M. Kube, B. Kick, H. Dietz, *Sci. Adv.* **2018**, *4*, eaau1157.
- [17] V. Cassinelli, B. Oberleitner, J. Sobotta, P. Nickels, G. Grossi, S. Kempter, T. Frischmuth, T. Liedl, A. Manetto, *Angew. Chem. Int. Ed.* **2015**, *54*, 7795–7798; *Angew. Chem.* **2015**, *127*, 7905–7909.
- [18] S. D. Perrault, W. M. Shih, *ACS Nano* **2014**, *8*, 5132–5140.
- [19] N. P. Agarwal, M. Matthies, F. N. Gür, K. Osada, T. L. Schmidt, *Angew. Chem. Int. Ed.* **2017**, *56*, 5460–5464; *Angew. Chem.* **2017**, *129*, 5552–5556.
- [20] F. Q. Tang, L. L. Li, D. Chen, *Adv. Mater.* **2012**, *24*, 1504–1534.
- [21] J. G. Croissant, Y. Fatieiev, A. Almalik, N. M. Khashab, *Adv. Healthcare Mater.* **2018**, *7*, 1700831.
- [22] K. Möller, T. Bein, *Chem. Mater.* **2017**, *29*, 371–388.
- [23] H. Y. Chiu, D. Goss, L. Haddick, H. Engelke, T. Bein, *Chem. Mater.* **2018**, *30*, 644–654.
- [24] M. Darbandi, R. Thomann, T. Nann, *Chem. Mater.* **2005**, *17*, 5720–5725.
- [25] M. Aslam, S. Li, V. P. Dravid, *J. Am. Chem. Soc.* **2007**, *90*, 950–956.
- [26] O. Tomohiko, W. Nodoka, S. Toshio, H. Tetsuji, M. Shoji, *Chem. Lett.* **2011**, *40*, 106–107.
- [27] H. M. Joshi, M. De, F. Richter, J. He, P. V. Prasad, V. P. Dravid, *Contrast Media Mol. Imaging* **2012**, *7*, 460–468.
- [28] G. Cheng, Y. Wang, Z.-G. Wang, X.-J. Sui, J.-L. Zhang, J.-Z. Ni, *RSC Adv.* **2014**, *4*, 7694–7702.



- [29] B. Liu, Y. Y. Cao, Z. H. Huang, Y. Y. Duan, S. N. Che, *Adv. Mater.* **2015**, *27*, 479–497.
- [30] X. Liu, F. Zhang, X. Jing, M. Pan, P. Liu, W. Li, B. Zhu, J. Li, H. Chen, L. Wang, J. Lin, Y. Liu, D. Zhao, H. Yan, C. Fan, *Nature* **2018**, *559*, 593–598.
- [31] T. Zhang, C. Hartl, K. Frank, A. Heuer-Jungemann, S. Fischer, P. C. Nickels, B. Nickel, T. Liedl, *Adv. Mater.* **2018**, *30*, 6.
- [32] W. Stöber, A. Fink, E. Bohn, *J. Colloid Interface Sci.* **1968**, *26*, 62–69.
- [33] M. Numata, K. Sugiyasu, T. Hasegawa, S. Shinkai, *Angew. Chem. Int. Ed.* **2004**, *43*, 3279–3283; *Angew. Chem.* **2004**, *116*, 3341–3345.
- [34] C. Y. Jin, H. B. Qiu, L. Han, M. H. Shu, S. A. Che, *Chem. Commun.* **2009**, 3407–3409.
- [35] C. Kiehl, Y. Xin, B. Shen, M. A. Kostianen, G. Grundmeier, V. Linko, A. Keller, *Angew. Chem. Int. Ed.* **2018**, *57*, 9470–9474; *Angew. Chem.* **2018**, *130*, 9614–9618.
- [36] E. Auyeung, R. J. Macfarlane, C. H. J. Choi, J. I. Cutler, C. A. Mirkin, *Adv. Mater.* **2012**, *24*, 5181–5186.

Manuscript received: October 2, 2018

Accepted manuscript online: November 6, 2018

Version of record online: December 11, 2018

## 4 One-Pot Synthesis of Gold-Silver Nanorods for Plasmonic Application

Plasmonic nanoparticles have interesting optical properties which depend on their material, size and shape. They come in a variety of colors and were used since ancient times to stain the windows of churches.<sup>[91]</sup> Their plasmonic behavior originates from a strong interaction between incident light and the free electrons giving rise to collective electron vibrations that are defined as plasmons.<sup>[92-93]</sup> Depending on the boundary condition there are bulk plasmons, propagating and localized surface plasmons (PSP and LSP). As in this case the plasmons are confined to the surface and volume of the NP; they are localized on the particle's surface. The LSP can be excited by external light with an energy corresponding to the nanoparticle's resonance wavelength. The metal NP can be seen as an antenna that converts the light into strong localized electric fields and as a waveguide routing the light to desired locations with nanometer precision. There has been growing interest in using strong field enhancement and light localization in plasmonic nanostructures to control the polarization properties of light.

Today, a wide application of metal NPs includes the detection of biomarkers in so-called rapid tests (see **Chapter 2.3**). The collection of individual and randomly oriented gold nanospheres with no special interparticle interaction (e.g. plasmonic coupling) are used to give a visual impression as read out. Besides the unique properties of individual NPs multiple plasmonic NPs with defined inter-particle distance (of a few nanometers) and orientation to each other have a synergistic physical effect called plasmonic coupling. The plasmon coupling of particle dimers was described in 2004<sup>[82]</sup> similarly to the well-established atomic orbital hybridization theory by Pauling<sup>[94]</sup> (see **Chapter 2.2 Plasmon Hybridization Model**). Plasmon coupling is used to concentrate the light in the gap between the NPs giving rise to an extremely enhanced electric field within that small area - the "hot spot". From the hot spot very specific and strong optical responses can be obtained. For example, the interaction of the near-field with a chiral molecule that is placed in the hot spot can be used to optimize the selective light absorption by the molecule. Chiral molecules are molecules whose mirror images cannot be superimposed by any translation or rotation. These molecules are ubiquitous in nature and play a key role in

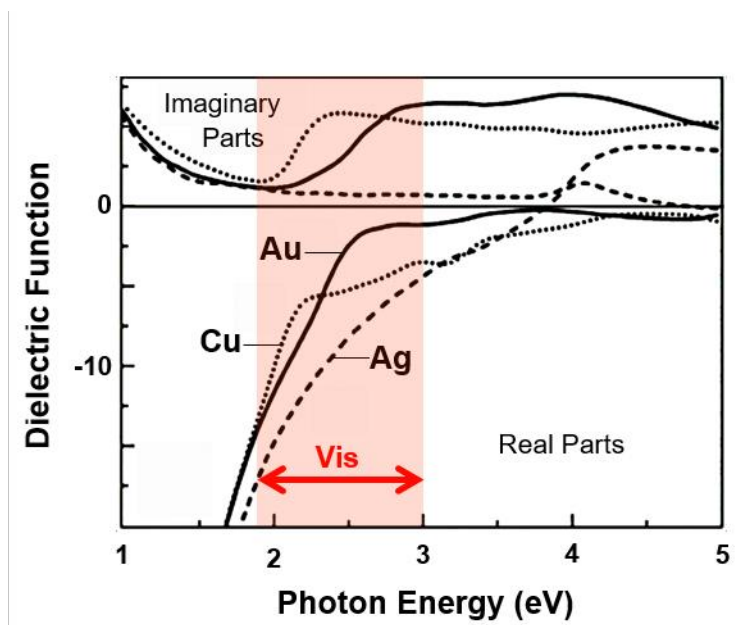
chemical and biological processes. For example, the therapeutic effects of chiral drugs can diverge strongly depending on their chiral properties.

As in case of chiral geometrical assemblies of NPs chiral plasmons are generated through the coupling of plasmon modes of the interacting NPs.<sup>[95]</sup> Chiral plasmonic structures exhibit significantly large optical activity since they interact strongly and differently with right- and left-handed circularly polarized light leading to enhanced chiroptical responses.<sup>[96]</sup> Therefore, they are of great practical interest for chemical and biological research.<sup>[97]</sup>

For the arrangement of nanoparticles in a controlled manner DNA origami has proven to be a great tool.<sup>[98]</sup> Yet, the method has been applied to a limited number of different plasmonic nanoparticles. Although metals supporting plasmons in the visible and near infrared include gold, silver, copper, aluminum, and lithium (**Table 2, Plasmonic ability**), their practical use is rather dependent on their stability, availability, and optical losses (free electron losses). The loss mechanism originates from interband electronic transitions. This means that electrons jump to higher, empty energy levels caused by absorption of incident photons. Bound electrons can also shift to the Fermi surface or to the next higher energy levels. Both processes result in significant losses.

Gold has high interband losses at wavelengths below or about 500 nm. Although the plasmon resonances of Au nanospheres cover a small range (510 – 570 nm), they are still widely used owing to their chemical stability, non-reactivity, and commercial availability. Copper has large losses over most of the visible spectrum and aluminum has interband transitions around 800 nm, both giving rise to plasmon damping in the visible. However, Al is an attractive plasmonic material in the UV range. The application of Cu and Al is further restricted by their colloidal instability. Moreover, progress and advances in synthesizing Cu and Al NPs with sufficient quality are still to be made.<sup>[99]</sup>

Alkali metals such as Li have very poor stability under atmospheric condition, hence are not suitable for practical use.



**Figure 12.**<sup>[100]</sup> Dielectric function  $\epsilon$  of Au, Ag, and Cu. The imaginary part  $\epsilon''$  is associated with the losses in the metal; the dissipation of energy into the medium. The losses of Ag are the lowest. The real part  $\epsilon'$  represents the ability to permit the electric field. The real part is an indication of the degree to which a material can be polarized. Negative values mean that the excited field is in opposite direction to the external field. From Vis to NIR Ag shows the best polarization ability. Adapted with permission.

Here, we emphasize on plasmonic applications of silver NPs as they are very promising in terms of property, stability, and quality. Silver is known to exhibit superior plasmonic properties including long plasmonic lifetime, sharp resonance band, and large plasmon tunability range.<sup>[74]</sup> According to theoretical studies Ag is considered the best material for plasmonics due to its lowest optical loss in the visible and NIR spectral range.<sup>[101]</sup> Silver is able to support strong surface plasmons from 300 – 1200 nm since its interband transitions lie outside that region.

The dielectric function  $\epsilon = \epsilon' + i\epsilon''$  (**Figure 12**) describes how a material's optical properties are dependent on the incident wavelength of light. The real part  $\epsilon'$  describes the strength of polarization by an external electric field. The imaginary part  $\epsilon''$  indicates the material's losses and is related to interband transitions. It describes the losses encountered when polarizing the material. Thus, a low loss material is associated with small values of  $\epsilon''$ .



**Table 2. Stability of different metals and their ability to support plasmons.**<sup>[102]</sup>

<b>Metal</b>	<b>Stability</b>	<b>Plasmonic ability</b>
Aluminum	Easy oxidation; Stable after surface passivation	Good in UV region
Copper	Easy oxidation	Good; interband transition below 600 nm
Gold	Very stable	Good; interband transition below 500 nm
Lithium	extremely reactive	Good
Silver	oxidation	Very good; low optical loss

Although the chemical synthesis of silver NPs of different shapes were reported, the literature lacks reliable protocols for the fabrication of silver NPs that are functionalized with DNA and have a prolonged stability for further utilization and long-term application. As indicated above, the chemical properties such as stability and reactivity of a metal are very crucial for its practical exploration (**Table 2, Stability**). Therefore, to study plasmonics in a broader (spectral) range and to extend its applicational scope there is an urgent need to ensure the metal's stability during and after synthesis. After the synthesis the subsequent functionalization with DNA is essential for the defined assembly using DNA origami to study the interparticle plasmon coupling effects. Conventional DNA functionalization methods were optimized only for gold spheres. Further, the reported methods involve an exchange process where the stabilizing capping agent is replaced by the DNA which is time consuming and inconvenient and meanwhile during that process the NPs are susceptible to aggregation and decomposition. Therefore, the great challenge includes stability preservation during and after DNA adsorption on the surface as well as after the assembly with DNA origami and after the final purification process.

Our idea includes having a supportive and stable gold nanorod core and a thick shell out of silver providing the desired plasmonic features mentioned above. We present a simple procedure for the fabrication and functionalization of gold-silver core-shell nanorods, their subsequent geometrical arrangement using DNA origami, and their use for optical signal enhancement. The implementation works under normal condition and it is extremely fast and convenient; since it excludes the exchange process, stability issues cannot arise. Instead, the Au/Ag core-shell rods are instantaneously functionalized with thiol modified DNA during the reduction of silver nitrate on the gold surface. The growing silver shell is immediately covered by the DNA owing to the strong silver-sulfur bond.<sup>[103]</sup> The excess thiols are removed to hinder subsequent reactions such as sulfidation which would lead

to the production of a silver sulfide ( $\text{Ag}_2\text{S}$ ) shell. During sulfidation the S-C bonds are broken and the S atoms are shifted below the surface while Ag atoms are brought to the surface which leads to a cleavage of the linked DNA.<sup>[104]</sup> Hence, the removal of excess thiols is essential to avoid that process, leading to an enhanced shelf life of the Au/Ag core-shell NRs.

Subsequent arrangement of the fabricated bimetallic nanoparticles into a chiral structure using DNA origami enabled us to study their plasmonic behavior and relate them to our theoretical studies.<sup>[105]</sup> We anticipated and observed stronger plasmon interactions and optical activity induced by the silver-shell. For quantification the anisotropy factor was determined. The anisotropy factor  $g$  is often used as a measure of optical activity and characterizes the strength of interactions between light and particle.<sup>[106]</sup> It quantifies the relative strength of the CD signal over extinction and is given by the following equation:  $g = 2(\sigma_L - \sigma_R)/(\sigma_L + \sigma_R)$ , where  $\sigma_L$  and  $\sigma_R$  are extinction cross-sections with left and right circularly polarized light, respectively. The silver shell raised the  $g$ -factor of the core AuNRs by a factor of 7 which is considered high compared to other chiral systems.<sup>[107]</sup>

The presented practical method enabled us to generate and enhance chiral plasmonic interactions. The results promote a deeper understanding and set the foundation for future studies of more complex chiral plasmonic structures. Chiroptical systems have great potentials for use in e.g. detection of diseases, photocatalysis and chemical sensing.<sup>[97]</sup>

## 4.1 Associated Publication 2

ACS NANO

www.acsnano.org

## Chiral Assembly of Gold–Silver Core–Shell Plasmonic Nanorods on DNA Origami with Strong Optical Activity

Linh Nguyen, Mihir Dass, Martina F. Ober, Lucas V. Besteiro, Zhiming M. Wang, Bert Nickel, Alexander O. Govorov, Tim Liedl, and Amelie Heuer-Jungemann\*

Cite This: *ACS Nano* 2020, 14, 7454–7461

Read Online

ACCESS

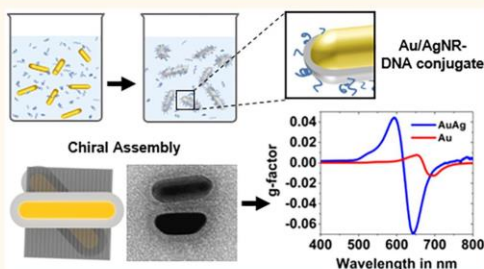
Metrics &amp; More

Article Recommendations

Supporting Information

**ABSTRACT:** The spatial organization of metal nanoparticles has become an important tool for manipulating light in nanophotonic applications. Silver nanoparticles, particularly silver nanorods, have excellent plasmonic properties but are prone to oxidation and are therefore inherently unstable in aqueous solutions and salt-containing buffers. Consequently, gold nanoparticles have often been favored, despite their inferior optical performance. Bimetallic, *i.e.*, gold–silver core–shell nanoparticles, can resolve this issue. We present a method for synthesizing highly stable gold–silver core–shell NRs that are instantaneously functionalized with DNA, enabling chiral self-assembly on DNA origami. The silver shell gives rise to an enhancement of plasmonic properties, reflected here in strongly increased circular dichroism, as compared to pristine gold nanorods. Gold–silver nanorods are ideal candidates for plasmonic sensing with increased sensitivity as needed in pathogen RNA or antibody testing for nonlinear optics and light-funneling applications in surface enhanced Raman spectroscopy. Furthermore, the control of interparticle orientation enables the study of plasmonic phenomena, in particular, synergistic effects arising from plasmonic coupling of such bimetallic systems.

**KEYWORDS:** DNA origami, self-assembly, plasmonic nanoparticles, circular dichroism, bimetallic nanoparticles



Downloaded via LMU MUEENCHEN on March 16, 2021 at 17:50:23 (UTC).  
See <https://pubs.acs.org/sharingguidelines> for options on how to legitimately share published articles.

Metal nanoparticles (NPs) exhibit excellent optical properties of particular interest in a variety of fields of research including photonics, imaging,<sup>1</sup> medicine,<sup>2</sup> catalysis,<sup>3</sup> biosensing,<sup>4</sup> and optical data storage.<sup>5</sup> Anisotropic particles exhibit additional, strongly shape-dependent optical behavior, including localized field enhancement and optical nonlinearities.<sup>6</sup> The accessibility of different shapes and morphologies by wet chemical synthesis rather than through lithographic techniques has led to high-throughput fabrication and commercialization of such NPs. This led to a wide range of potential users and thus allowed for a fast progress in their general application. In particular, the seed-mediated growth method, which was first applied only to nanospheres but later revolutionized the field of anisotropic NPs (*e.g.*, NRs or nanostars), has led to synthesis protocols for the production of near-monodisperse particles at high yields.<sup>7,8</sup>

In order to manipulate light on the nanoscale, controlling interparticle distance and particle orientation is key. For example, so-called plasmonic hot spots in the gaps between metal particles can lead to strong enhancement of the radiative properties of molecules inside such hot spots by orders of

magnitude allowing surface enhanced Raman scattering<sup>9</sup> on the single-molecule level.<sup>10</sup> The DNA origami technique provides such precise control over metal NPs organization, as demonstrated, *e.g.*, for plasmon-induced circular dichroism, a phenomenon based on the near-field coupling of chiral assemblies of NPs<sup>11</sup> that can be employed for sensitive analyte detection.<sup>12–16</sup>

While the general plasmonic behavior of gold (Au) and silver (Ag) NPs is similar,<sup>17</sup> a Ag shell induces larger near-field enhancement<sup>18</sup> and narrower plasmon line width compared to that of pure Au nanorods (NRs) of the same resonance wavelength.<sup>19</sup> Furthermore, Ag exhibits a vastly greater extinction cross-section<sup>20</sup> and has the lowest losses of

Received: April 14, 2020

Accepted: May 27, 2020

Published: May 27, 2020



ACS Publications

© 2020 American Chemical Society

7454

<https://dx.doi.org/10.1021/acsnano.0c03127>  
ACS Nano 2020, 14, 7454–7461



metals in the visible and near-infrared (NIR), which is generally beneficial for plasmonic applications.<sup>21,22</sup> Nevertheless, the high chemical stability of Au NPs is often decisive for practical use in spite of better optical properties for Ag NPs. Consequently, research thus far focused on Au NPs. While spherical Ag NPs have been successfully incorporated into DNA-based assemblies,<sup>23–25</sup> AgNRs hitherto refused to cooperate with DNA origami. Also, bimetallic Au/Ag NPs—which are distinct from a simple combination of the two individual components—and their controlled self-assembly have remained virtually unstudied.

Primarily the chemical instability of Ag-containing NPs has hampered their widespread use in self-assembly based plasmonics. In particular, oxidation, disintegration, and fast aggregation are troublesome when ligand-exchange reactions need to be performed, which is often required to infer further functionality. DNA is a widely used ligand for the controlled assembly of metal NPs; however, preparing DNA–Ag NP conjugates is not trivial since phosphines, commonly used to produce thiol reactive groups in DNA, interact with Ag ions hindering the conjugation process.<sup>26</sup> Moreover, the preparation of AgNRs, with a reliable control over aspect ratio and monodispersity, has thus far been strongly limited. Au/Ag core–shell NRs, which offer stability through the Au core as well as cooperative and superior plasmonic behavior,<sup>19,27,28</sup> represent the best compromise so far in synergistic effects for stability and optical performance.

In Au/Ag core–shell systems, the use of large polymeric stabilizing agents, such as polyvinylpyrrolidone (PVP), has been suggested to avoid aggregation and increase stability in order to resolve issues with conventional stabilizing agents such as cetyltrimethylammonium bromide (CTAB).<sup>29</sup> However, while the resulting steric effects provide efficient stabilization, they also prevent functional molecules from interacting with the particle surface. We speculate that, therefore, the functionalization of Au/Ag core–shell NRs with DNA and the controlled assembly of such NRs on a DNA origami substrate could not be explored to date.

Here, we abandon the concept of a two-step reaction, *i.e.*, initial synthesis of a Ag shell and subsequent functionalization. We conduct a simple one-pot reaction (Scheme 1) that yields stable DNA-coated Au/AgNRs with good monodispersity.

We show that the particles' aspect ratio as well as their core and shell sizes and, thus, the respective localized surface plasmon resonance (LSPR) can be fine-tuned as desired. The particle's biocompatibility increases further by *in situ* conjugation to DNA. Since thiolated DNA is used as the initial stabilizing ligand, further ligand replacement steps

become obsolete. We demonstrate that these particles can easily be assembled on DNA origami templates for studying and understanding cooperative and synergistic effects of such bimetallic plasmonic systems. We furthermore show that, besides DNA, other thiol-containing ligands can be incorporated in the ligand shell, rendering our approach simple and universal.

## RESULTS AND DISCUSSION

The Ag shells on the AuNRs were synthesized using a protocol by Guyot-Sionnest and co-workers,<sup>27</sup> which was modified with the rationale of achieving instantaneous functionalization with thiolated DNA, limiting particle disintegration and oxidation over time. In order to ensure that the NRs are sufficiently stabilized, the thiol–DNA is added in excess. During Ag shell growth, using AgNO<sub>3</sub> as precursor and L-ascorbic acid as reducing agent, the thiol–DNA binds to the Ag surface, imparting instantaneous stabilization and functionalization. The lattice constants of Au and Ag have 0.2% mismatch only, allowing for epitaxial Ag growth and formation of monocrystalline Au/AgNRs.<sup>27</sup> The Ag-layer thickness can be tuned by the ratio between AuNR and AgNO<sub>3</sub> concentration, *i.e.*, a lower ratio leads to thicker shells. It should also be noted that our method is not limited to rod-shaped particles but can also be further extended to other shapes, *e.g.*, spheres, yielding highly stable DNA-coated Au/Ag NPs (Figure S2).

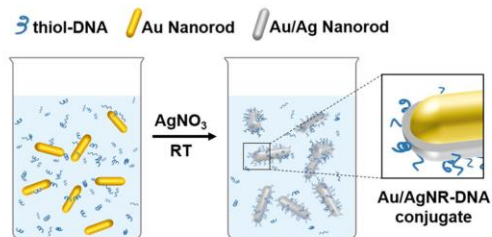
Au/Ag core–shell NRs with varying thicknesses of Ag shell were subsequently analyzed by UV–vis spectroscopy and transmission electron microscopy (TEM) (Figure 1). The individual batches exhibited good monodispersity at high production yields resulting in sharp resonance signals in the absorption spectrum (Figure 1 and Figure S3). UV–vis spectra of the Ag/AuNRs were experimentally recorded and simulated theoretically, *cf.* Figure 1a,b.

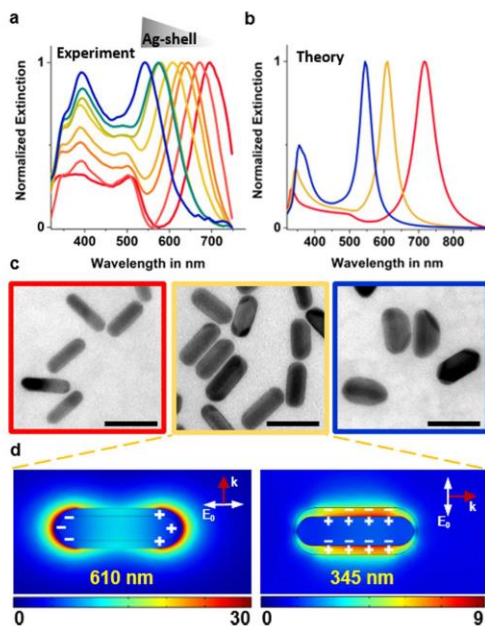
Prominent features of these spectra are the gradual blue-shift of the longitudinal mode of the LSPR and the overall enhancement of the signal strength with increasing Ag shell thicknesses (Figure 1a and Figure S4). These results can be explained by a combination of two effects, namely the increase in effective carrier mobility of the bimetallic NR, when excited longitudinally, as the Au is progressively covered by Ag and the decreased aspect ratio of the Ag-shelled NRs for thicker shells.<sup>29</sup> We also observe the appearance of a new plasmonic mode at short wavelengths, strongly localized at the Ag shell layer. The thickness of the Ag shell depends on the Ag<sup>+</sup> ion concentration during synthesis;<sup>18</sup> therefore, the blue-shift of the resonance wavelength of the longitudinal mode can be easily and accurately tuned over a wide spectral range from the visible to the NIR. Here we demonstrate a stepwise shift of the longitudinal plasmon mode from 834 nm for the pristine AuNRs (39.2 × 9.8 nm), *cf.* Figure S1, to a resonance at 545 nm by using ~5 nM AuNRs and AgNO<sub>3</sub> concentrations ranging from 10 to 40 mM which resulted in Ag shell thicknesses ranging from ~1.1 to 5.4 nm (Figure 1c).

Molar extinction coefficients of Au/AgNRs@DNA were experimentally deduced through the relative rise of absorption intensity of the initial AuNRs, which are in good accordance with theoretically calculated values (Table S1).

The optical behavior can be qualitatively described with the Au core being gradually electrically screened by the Ag shell. Numerical simulations reproduce the spectral behavior of the Ag-shelled Au nanorods extremely well (Figure 1b), not only tracking the progressive blue-shift of the main plasmonic peak

**Scheme 1. One-Pot Synthesis of DNA-Functionalized Au/Ag Core-Shell Nanorods Denoted Au/AgNRs@DNA**





**Figure 1.** (a) Experimental extinction spectra of Au/AgNRs@DNA synthesized using different  $\text{AgNO}_3$  concentrations (10–40 mM) resulting in distinct Ag shell thicknesses from  $\sim 1.1$  (red line) to  $\sim 5.4$  nm (blue line), cf. Figure S4 for the respective non-normalized extinction spectra. (b) Calculated theoretical extinction spectra of Au/AgNRs in water for the Ag shells of 1.1 (red line), 3.1 (yellow line), and 5.4 nm (blue line). (c) TEM images of Au/AgNRs@DNA with different Ag shell thicknesses ( $\sim 1.1$ ,  $\sim 3.1$ , and  $\sim 5.4$  nm) tuned by raising  $\text{AgNO}_3$  ratio (10, 25, 40 mM). Scale bars are 40 nm. (d) Field maps of Au/AgNRs synthesized with 25 mM  $\text{AgNO}_3$  with a 3.1 nm shell, showing values of  $|E|/E_0$ , or the near-field enhancement of the particles. The left panel shows the stronger longitudinal modes, while the right panel depicts the transversal modes. Here we also show schematically the charges induced by the plasmonic modes.

but also showcasing the increasing relative amplitude of the secondary plasmonic peak, found at higher frequencies. This secondary peak results from the excitation of a transversal mode on the Ag-shelled nanorods and increases its amplitude as the Ag shell thickens. The field enhancement of this resonant mode is localized in the Ag shell, as it is apparent by observing the field maps in Figure 1d. This implies the formation of charge dipoles between the Au/Ag interface and the outer Ag surface, as we illustrate with schematic charge signs in the right panel of Figure 1d. This does not occur when exciting the longitudinal modes in which the main peak polarizes the whole structure. Thus, even though for both modes the relevance of the plasmonic properties of Ag increase as the thickness of the shell grows, their qualitative responses differ. Under longitudinal polarization, the most apparent change is the blue-shift of the plasmonic resonance as more Ag is available to carry the longitudinally oscillating currents, due to the higher plasma frequency of Ag with respect to Au. Under a transversal polarization we see the appearance of a

resonant mode localized at the shell at a wavelength that is far from the unscreened transversal resonance of Au at 515 nm (Figure S5).

These differences highlight the interest of studying bimetallic systems with nonspherical geometries, as they can offer richer scenarios for tuning their optical properties. Clearly, the spectra do not arise as the simple sum of the individual components, *i.e.*, nonlinear effects occur. Similar observations have been reported previously, *e.g.*, Ag-involving metallic systems display additional absorption behavior at 340–350 nm, and this includes bipyramidal Au NPs with a rod-shaped Ag shell,<sup>30</sup> AuNRs with an octahedral Ag shell,<sup>31</sup> as well as AgNRs,<sup>32</sup> wires,<sup>33</sup> prisms,<sup>34</sup> cubes,<sup>35</sup> and more complex shapes.<sup>9</sup> Opinions are divided over the detailed origin of this signal;<sup>36–38</sup> therefore, it still remains a topic of investigation to date and more effort needs to be expended in order to understand and particularly to manipulate plasmons in such Ag systems.

Transmission electron microscopy (TEM) analysis reveals the DNA shell as a bright halo around the NRs when stained with uranyl formate, and the Au core can be distinguished from the Ag shell due to the difference in electron density of the two metals (Figure 1c,d). Previous studies have shown that the deposition of Ag preferentially occurs on certain Au crystal facets and that two of the four (110) side facets of the freshly growing Ag crystal build up more quickly than the remaining two facets.<sup>27,39</sup> Consequently, the position of the Au core becomes geometrically less central as the shell thickness increases (Figure 1c, right panel). Although the microscopic origin of this behavior is not fully understood, it is believed that a selective adsorption of CTAB on different crystal planes of fcc Ag leads to the resulting morphology of the particles.<sup>39</sup> Notably, without CTAB, no Ag shell could be grown around the AuNR.<sup>31</sup> A possible explanation is that the formation of AgBr, where the  $\text{Br}^-$  ions are provided by CTAB which adsorb onto the facets of Au, is essential for the Ag growth.<sup>40</sup>

As mentioned above, a further stabilizing ligand besides CTAB is required to ensure colloidal NR stability. DNA provides additional functionality, such as sequence-specific binding. Therefore, we focus in our report primarily on this versatile ligand. In all of the coating procedures presented here, DNA was added in large excess; *i.e.*, the reaction solution contains many unbound DNA molecules after completion of the Ag shell growth. This excess amount of DNA can either be removed by centrifugation or alternatively be used to achieve higher DNA loading on the particles. Recently, Liu *et al.* showed that very high DNA loading on Au NPs could be achieved by simply freezing the particles with thiolated DNA.<sup>41</sup> We adapted this strategy for our Ag/AuNRs by optionally freezing the whole reaction mixture after completion of the Ag coating for increased DNA loading as well as for long-term storage and retaining quality. It is noteworthy that after a removal of the excess DNA, performed after completion of the synthesis, the Au/AgNRs@DNA can withstand at least 10 freeze–thaw cycles without any changes in colloidal quality and optical properties (Figure S7). Storing of the Au/AgNRs in the frozen state ensures colloidal stability over a very long period of time as the oxidation process of the silver is slowed down, which in turn greatly improves the stability and ease of use of the NPs. In contrast, conventionally stabilized NPs aggregate immediately and irreversibly upon freezing.

At ambient conditions, a variety of DNA sequences provide colloidal and chemical stability for at least one month (Figure



S8). In order to investigate the impact of sequence length and base content of the coating DNA on the stability of the particles in detail, we employed eight different sequences of varying strand lengths: polyA<sub>19</sub>, polyT<sub>19</sub>, polyT<sub>15</sub>, polyT<sub>8</sub>, polyG<sub>19</sub>, and polyC<sub>19</sub> as well as two “random” sequences, *i.e.*, sequences of heterogeneous base composition (Table S2). For all sequences, the Ag-coating process was successful, verified by a blue-shift of the extinction signal of the longitudinal mode, which was also visible by eye through a color change of the colloidal solution. However, we find that different DNA sequences yield very different degrees of stability, ranging from quickly aggregating to highly stable dispersions (Figure S8).

For particles with Ag shells grown in the presence of polyA<sub>19</sub>, aggregation occurred under ambient conditions within 2 h (Figure S8g). This could be attributed to adenine generally exhibiting a high affinity to metal surfaces.<sup>42</sup> The adenine bases likely adsorb to the NR surface, thus hindering thiol–Ag interactions and thus efficient DNA loading, which would be required for colloidal stability. Similarly, cytosine also displays a high affinity to metal NPs albeit not as strongly as adenine. Additionally, it has been reported that polyC DNA has the ability to etch Ag,<sup>43</sup> which may also shorten the stability time frame. Consequently, Au/AgNRs@polyC<sub>19</sub> aggregated within 30 min under ambient conditions (Figure S8h). For polyG<sub>19</sub>, no aggregation was observed and only a small change in the absorption spectrum became visible after 1–2 weeks (Figure S8f). However, repeated centrifugation and redispersion gradually resulted in Au/AgNRs@polyG<sub>19</sub> aggregation. We attribute this to the fact that polyG sequences are prone to forming G-quadruplexes. If G-quadruplexes are formed intramolecularly, the surface density should be higher than that of “random coil” DNA; thus, higher loading would be possible. However, we hypothesize that intermolecular G-quadruplex formation may also occur leading to cross-linking of the particles. For polyT<sub>8,15,19,30</sub> and the two random sequences, no aggregation was observed for at least one month (end of observation time) and even after multiple centrifugation and freeze–thaw cycles (Figure S7). Further, we did not observe any significant difference in stability over time at ambient conditions for the different polyT lengths (Figure S8). The Au/AgNRs@polyT<sub>19</sub> and Au/AgNRs@random could also be run on agarose gels where both samples displayed good electrophoretic mobility and striking monodispersity in case of the polyT coating (Figure S10).

In order to test if the thiol reactive group is essential for effective particle stabilization, we employed nonthiolated polyT<sub>19</sub> and random sequences in the synthesis. As expected, using nonthiolated DNA did not result in stable particles as can be clearly seen by the formation of aggregates in the wells of the agarose gel (Figure S10).

To access the homogeneity of the surrounding DNA shell and to obtain the structural details including crystallinity of the Au/AgNRs@DNA, we performed small-angle and wide-angle X-ray scattering (SAXS and WAXS) experiments on 15 nm × 7 nm AuNRs with a thin Ag shell of 5 Å, and a polyT<sub>19</sub> as the stabilizing ligand. SAXS probes particle size and particle–particle distances. The SAXS intensity as a function of the scattering vector  $q = \frac{4\pi}{\lambda} \sin\theta$ , where  $\lambda$  is the wavelength of the X-rays and  $\theta$  the half of the scattering angle  $2\theta$ , is shown in Figure 2a. From this data one can readily infer that the particles are well dispersed; *i.e.*, formation of clusters of particles can be excluded based on the presence of the intensity plateau at small  $q$  and the absence of correlation or cluster

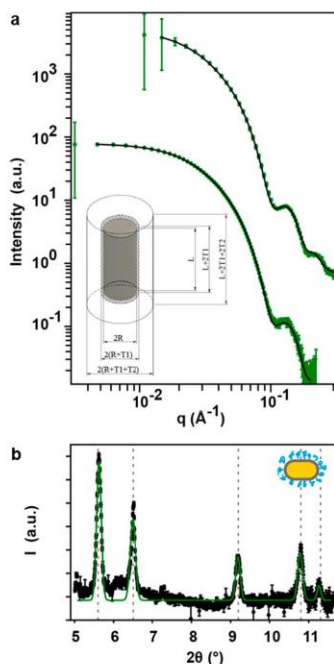


Figure 2. (a) Small-angle X-ray scattering (SAXS) intensities (dots), with model fits based on cylindrical core–shell–shell particles (lines). Intensities were recorded at two detector positions, 5.1 and 2.0 m from the sample, and the model was refined to both data sets simultaneously. Data were scaled for clarity. Inset: Schematic sketch of a core–shell–shell cylinder particle. (b) Wide-angle X-ray scattering (WAXS) data.

peaks. Furthermore, the presence of interference effects indicates a well-defined particle shape. For quantitative analysis, we employed a model fit assuming cylindrical particles with two concentric shells, representing Ag and DNA, respectively. The model for the SAXS intensities is described in detail in Note S1 of the Supporting Information. From the SAXS measurements, we obtain an Au core radius  $R_{Au} = 3.4$  nm with a variance of the size distribution of  $\sim 0.4$  nm corresponding to a polydispersity (PD) of  $\sim 0.12\%$  and a length  $L_{Au} = 15.5$  nm with a variance of the size distribution of  $\sim 4.5$  nm corresponding to a polydispersity (PD) of  $\sim 0.29\%$ . The Ag and DNA shell thicknesses are  $d_{Ag} = 5$  Å and  $d_{DNA} = 2.9$  nm, respectively. The shell thickness  $d_{DNA} = 2.9$  nm is close to the Flory radius of polyT<sub>19</sub> DNA (4 nm) and somewhat smaller than the highly dense brush regime as observed for DNA on Au NPs (5.7 nm).<sup>44</sup> Furthermore, all parameters obtained in solvent conditions are in good agreement with the dimensions obtained from TEM images and the NR synthesis design.

Crystal structure and crystallinity of the Au/AgNRs@DNA were obtained from WAXS experiments. The WAXS diffraction pattern for different particle compositions (Figure S11) are shown as intensity  $I$  vs scattering angle  $2\theta$  in Figures S2b and S12. The WAXS profiles show fcc diffraction peaks with a refined lattice parameter of  $a_{Au} = 4.0745$  Å,  $a_{Au} = 4.0756$

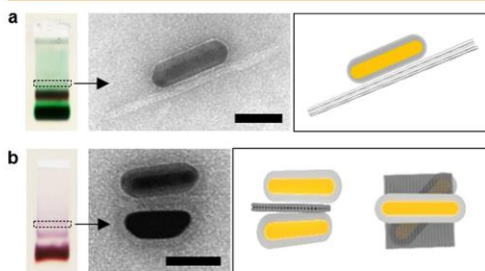
Å, and  $a_{\text{Au}} = 4.0770$  Å for AuNRs, Au/AgNRs, and Au/AgNRs@DNA, respectively. The obtained lattice parameters are in good agreement with the literature lattice constant  $a_{\text{Au}} = 4.0704$  Å and  $a_{\text{Ag}} = 4.07778$  Å.<sup>45</sup>

Importantly, we observe no features in our SAXS or WAXS data, which would indicate a permeation of DNA through the Ag shell. From this, we derive the DNA being conjugated only on the Ag surface through the thiol–Ag bond (cf. Figure S10).

We hypothesized that our method is not restricted to using thiolated DNA as a ligand but can be applied more universally using other ligands displaying a thiol group. To demonstrate this, we used mercaptopropionic acid (MPA) and *O*-(2-mercaptoethyl)-*O'*-methylhexa(ethylene glycol) (mPEG thiol) as ligands. For both ligands, formation of the Ag shell was successful; however, differences in stability of the resulting particles could be observed. The Ag/AuNRs@mPEG-thiol display a slight change in quality after several freeze–thaw cycles as evidenced by UV/vis spectroscopy (Figure S7e). The optical behavior was also monitored over several weeks at ambient condition (Figure S8k) where the Ag/AuNRs display slight changes in the UV/vis spectrum after 7 days. The MPA-functionalized Ag/AuNRs lose their quality upon freezing (Figure S7d). However, they can be stored under ambient conditions for 3 weeks after which they show slight changes in their optical behavior (Figure S8l).

Although such stable Au/AgNRs already possess excellent optical properties as single particles, studying their behavior in controlled assemblies is of immediate interest. Our method of creating stable DNA-coated Au/AgNRs now gives access to assemble such bimetallic particles on DNA origami structures. For conjugating particles to DNA origami, it is essential that all components are stable in buffers containing salt. In order to verify that our particles are stable under typical conjugation conditions, Ag/AuNRs@DNA were dispersed in Tris acetate (TA) or Tris acetate EDTA (TAE) buffer containing increasing amounts of MgCl<sub>2</sub>. Both the polyT<sub>19</sub> and random DNA sequence modified Au/AgNRs displayed good stability in 1 × TA buffer containing MgCl<sub>2</sub> (Figure S9).

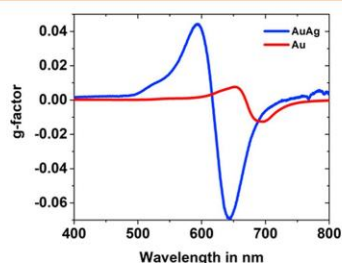
As a proof-of-principle we used two origami templates; a rod-shaped origami (14-helix bundle, 14 HB) with anchor strands along the long axis, and a flat square origami (44 HB, double-layer sheet), designed to align two Ag/AuNRs@DNA in a cross-like geometry as illustrated in Figure 3. Each origami



**Figure 3.** Agarose gel electrophoresis and TEM image of DNA-functionalized (a)  $78 \times 25$  nm Au/AgNRs conjugated with a 14 HB DNA origami rod and (b)  $64 \times 25$  nm Au/AgNRs conjugated with a 44 HB double-layered sheet DNA origami and the respective illustration of the Au/AgNRs@DNA@origami conjugates. Scale bars are 50 nm.

template was mixed with the Ag/AuNRs@DNA in a ratio of  $\sim 15$  rods per binding site in 1 × TA buffer containing 6 mM MgCl<sub>2</sub> to ensure hybridization of the anchor strands. The mixture was exposed to a temperature ramp, and the Au/AgNRs@DNA@origami conjugates were subsequently purified from excess NRs by agarose gel electrophoresis (Figure 3, left panels). The two fastest moving bands were assigned to excess Au/AgNRs@DNA and NR dimers, respectively. The slowest band contained the desired Au/AgNR@DNA conjugated with the DNA structure as confirmed by TEM (Figure 3, middle panels, and Figure S13). In each assembly, one can discern the Ag shell on the AuNR as well as the dense DNA shell surrounding the rod and connecting it to the respective DNA origami.

Assemblies such as the ones shown in Figure 3b furthermore display interesting optical properties in the form of circular dichroism (CD), owing to their chiral arrangement (Figure 4).



**Figure 4.** CD spectra of chiral AuNRs ( $55 \times 20$  nm, red curve) and Au/AgNRs ( $\sim 65 \times 30$  nm, Ag shell thickness  $\sim 5$  nm, blue curve), assembled on a 44 HB double-layered sheet DNA origami (cf. Figure 3b) displaying the characteristic bisignate shape. The signal is blue-shifted and strongly increased for the Au/AgNR assembly compared to the AuNR assembly.

The characteristic bisignate spectra arise from the plasmon interactions of the individual NRs in each assembly when excited by circularly polarized light, resulting in the rise of two distinct modes with opposite chirality. Corresponding with the shift in the longitudinal resonance peak of individual NRs, the CD spectra as a whole was also blue-shifted for structures assembled with Au/AgNR compared to AuNR assemblies (N.B.: The same AuNRs were used for the assembly and the formation of the Au/AgNRs).

The anisotropy factor, also known as the *g*-factor, is used as a measure of the structural asymmetry of chiral structures<sup>46,47</sup> (for further details, see the Supporting Information). As seen in Figure 4, the *g*-factor of Au/AgNR assemblies exceeds that of uncoated AuNR assemblies by a factor of 7 (see Figure S13 for representative TEM images) and is most importantly also 3× stronger than current state-of-the-art for colloidal systems in solution,<sup>48</sup> which proves both the excellent assembly capability as well as strong plasmonic capabilities of the bimetallic rods.

## CONCLUSION

We have presented a simple and fast one-pot method to synthesize monodisperse Au/AgNRs and their instantaneous functionalization with DNA. The size and aspect ratio of the Au/AgNRs and especially the Ag shell thickness can be precisely controlled, allowing us to tune the LSPR as desired.



Their improved shelf life and storability make them an ease-of-use product in the laboratory. Further, the DNA functionality of Au/AgNRs@DNA allows for their organization on a DNA origami platform, which as of yet has not been accessible using such bimetallic NPs or AgNRs. With this methodology, plasmonic structures built with DNA origami will be extended from mono- to bimetallic systems. In particular, the cooperative and synergistic effects of bimetallic structures will not only be of fundamental interest but also essential for optical applications. The bimetallic chiral assemblies shown here display strongly increased CD responses in comparison to their Au counterparts, which could hold great promise for plasmonic sensing with increased sensitivity as urgently required for antibody or pathogen RNA testing. In prospective work, our presented method may be also employed to create other particle geometries to further expand the variety of such ordered plasmonic systems.

## METHODS

**Synthesis of AuNRs.** The synthesis of AuNRs was carried out following the protocol by Murray *et al.*<sup>49</sup>

**Ag Coating of AuNRs and DNA Functionalization.** AuNRs were redispersed in 0.1 M CTAB resulting in a concentration of 5–50 nM of AuNRs. To 5 mL of this AuNR solution were added 22.5 mL of 0.1 M CTAB and 2.5 mL of 100  $\mu$ M of thiol-modified DNA (for chiral Au/AgNRs assemblies a mixture of polyT<sub>19</sub> and polyT<sub>8</sub> DNA in the ratio of 1:9 was used). Note that tris(2-carboxyethyl)phosphine (TCEP) is often used to cleave the disulfide bond of thiol-modified DNA; however, it strongly interacts with Ag and disturbs the Ag-coating process. Since CTAB crystallizes at room temperature, the mixture was stirred and heated to 35 °C and kept at this temperature during the entire procedure to ensure the dissolution of CTAB. Subsequently, 4 mL of 10–40 mM AgNO<sub>3</sub> and 625  $\mu$ L of freshly prepared 0.2 M L-ascorbic acid were added. In a last step, 1.25 mL of 0.2 M NaOH was injected under vigorous stirring to increase the pH and the reduction potential of L-ascorbic acid and thus to initiate the reaction. To obtain a high degree of monodispersity the formation of foam by CTAB needs to be avoided. Immediately a color change can be observed. The reaction is completed a few minutes to an hour after the color change depending on the AgNO<sub>3</sub> concentration that influences the Ag growth rate. The obtained Au/Ag core-shell nanorods were isolated from the reaction solution by 4 $\times$  centrifugation and redispersion in 0.1% SDS. Optionally, the NRs can be redispersed in 1  $\times$  TA buffer or water.

To further increase the DNA loading, the Au/AgNRs@DNA were not isolated from the reaction mixture but frozen at –20 °C. After thawing, the NRs were purified by centrifugation and redispersion in 0.1% SDS or 1  $\times$  TA buffer. For a long-term storage the Au/AgNRs@DNA were kept in the frozen state.

**Conjugation of DNA-Functionalized Au/AgNRs with DNA Origami.** The NRs were added in a ~10 $\times$  excess per binding site to the origami solution with a final concentration of 1–2 nM origami and 6 mM MgCl<sub>2</sub> in 1  $\times$  TA buffer. Under gentle shaking, the mixture was exposed to a temperature ramp starting at 45 °C followed by slow cooling to 20 °C (rate: 1 °C/10 min), repeated a total of four times. The Au/AgNRs@origami structures were isolated from excess Au/AgNRs by gel electrophoresis (Figure 3).

## ASSOCIATED CONTENT

### Supporting Information

The Supporting Information is available free of charge at <https://pubs.acs.org/doi/10.1021/acsnano.0c03127>.

WAX/SAXS data analysis methods and theoretical models; UV/vis data displaying stability of Au/AgNRs (PDF)

## AUTHOR INFORMATION

### Corresponding Author

Amelie Heuer-Jungemann – Faculty of Physics and Center for NanoScience (CeNS), Ludwig-Maximilians-University, 80539 Munich, Germany; [orcid.org/0000-0003-3630-6389](https://orcid.org/0000-0003-3630-6389); Email: [a.heuerjungemann@physik.uni-muenchen.de](mailto:a.heuerjungemann@physik.uni-muenchen.de)

### Authors

Linh Nguyen – Faculty of Physics and Center for NanoScience (CeNS), Ludwig-Maximilians-University, 80539 Munich, Germany

Mihir Dass – Faculty of Physics and Center for NanoScience (CeNS), Ludwig-Maximilians-University, 80539 Munich, Germany

Martina F. Ober – Faculty of Physics and Center for NanoScience (CeNS), Ludwig-Maximilians-University, 80539 Munich, Germany

Lucas V. Besteiro – Institute of Fundamental and Frontier Sciences, University of Electronic Science and Technology of China, Chengdu 610054, China; Centre Énergie Matériaux et Télécommunications, Institut National de la Recherche Scientifique, Varennes, QC J3X 1S2, Canada; [orcid.org/0000-0001-7356-7719](https://orcid.org/0000-0001-7356-7719)

Zhiming M. Wang – Institute of Fundamental and Frontier Sciences, University of Electronic Science and Technology of China, Chengdu 610054, China

Bert Nickel – Faculty of Physics and Center for NanoScience (CeNS), Ludwig-Maximilians-University, 80539 Munich, Germany

Alexander O. Govorov – Institute of Fundamental and Frontier Sciences, University of Electronic Science and Technology of China, Chengdu 610054, China; Department of Physics and Astronomy, Ohio University, Athens, Ohio 45701, United States; [orcid.org/0000-0003-1316-6758](https://orcid.org/0000-0003-1316-6758)

Tim Liedl – Faculty of Physics and Center for NanoScience (CeNS), Ludwig-Maximilians-University, 80539 Munich, Germany; [orcid.org/0000-0002-0040-0173](https://orcid.org/0000-0002-0040-0173)

Complete contact information is available at: <https://pubs.acs.org/doi/10.1021/acsnano.0c03127>

### Notes

The authors declare the following competing financial interest(s): A patent application (19210989.0) was submitted.

## ACKNOWLEDGMENTS

L.N. acknowledges financial support from the Deutsche Forschungsgemeinschaft (DFG) through the excellence cluster “e-conversion”. T.L. acknowledges funding through the European Research Council under the European Union’s Horizon 2020 research and innovation program (Grant Agreement No. 818635, DNA Funs). M.D. has received funding from the European Union’s Horizon 2020 research and innovation program under the Marie Skłodowska-Curie Grant Agreement No. 765703. M.O., B.N., T.L., and A.H.-J. acknowledge the financial support of the DFG through SFB1032 “Nanoagents”, projects A06/A07. We acknowledge DESY (Hamburg, Germany), a member of the Helmholtz Association HGF, for the provision of experimental facilities. Parts of this research were carried out at Petra III, and we thank Ann-Christin Dippel, Olof Gutowski, Oleh Ivashko, Pallavi Pandit, Stephan Roth, and Martin von Zimmermann for assistance in using P21.1 and P03. The research leading to this



result has been supported by the project CALIPSOplus under the Grant Agreement No. 730872 from the EU Framework Programme for Research and Innovation Horizon 2020. This work benefited from SasView software, originally developed by the DANSE project under NSF award DMR-0520547. A.O.G. acknowledges the support from the United States–Israel Binational Science Foundation (BSF). L.V.B. was supported by the Institute of Fundamental and Frontier Sciences, University of Electronic Science and Technology of China and China Postdoctoral Science Foundation (2017M622992 and 2019T120820). Z.M.W. was funded by the National Key Research and Development Program (No. 2019YFB2203400) and the “111 Project” (B20030). We also thank Maximilian Urban for synthesis and imaging of spherical Au/Ag NPs and Susanne Kempter for help with TEM imaging.

## REFERENCES

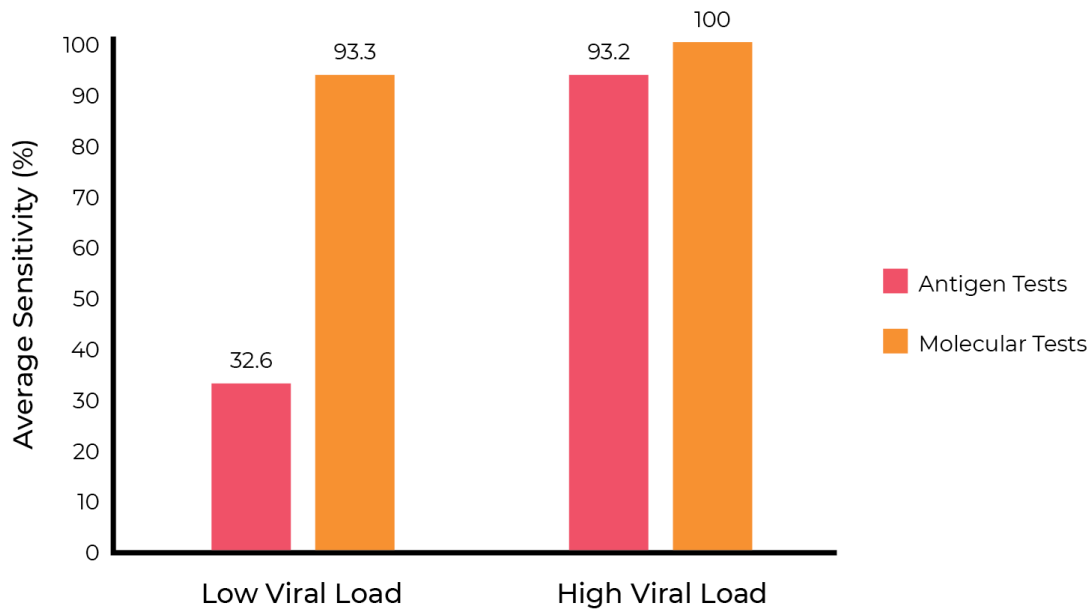
- (1) Cognet, L.; Tardin, C.; Boyer, D.; Choquet, D.; Tamarat, P.; Lounis, B. Single Metallic Nanoparticle Imaging for Protein Detection in Cells. *Proc. Natl. Acad. Sci. U. S. A.* **2003**, *100*, 11350–11355.
- (2) Boca, S. C.; Potara, M.; Gabudean, A.-M.; Juhem, A.; Baldeck, P. L.; Astilean, S. Chitosan-Coated Triangular Silver Nanoparticles as a Novel Class of Biocompatible, Highly Effective Photothermal Transducers for *In Vitro* Cancer Cell Therapy. *Cancer Lett.* **2011**, *311*, 131–140.
- (3) Prielcel, P.; Salami, H. A.; Padilla, R. H.; Zhong, Z.; Lopez-Sanchez, J. A. Anisotropic Gold Nanoparticles: Preparation and Applications in Catalysis. *Chin. J. Catal.* **2016**, *37*, 1619–1650.
- (4) Nath, N.; Chilkoti, A. Label Free Colorimetric Biosensing Using Nanoparticles. *J. Fluoresc.* **2004**, *14*, 377–389.
- (5) Gu, M.; Zhang, Q.; Lamon, S. Nanomaterials for Optical Data Storage. *Nat. Rev. Mater.* **2016**, *1*, 16070.
- (6) Lamarre, J.-M.; Billard, F.; Kerboua, C. H.; Lequime, M.; Roorda, S.; Martinu, L. Anisotropic Nonlinear Optical Absorption of Gold Nanorods in a Silica Matrix. *Opt. Commun.* **2008**, *281*, 331–340.
- (7) Jana, N. R.; Gearheart, L.; Murphy, C. J. Wet Chemical Synthesis of Silver Nanorods and Nanowires of Controllable Aspect Ratio. *Chem. Commun.* **2001**, 617–618.
- (8) Jana, N. R.; Gearheart, L.; Murphy, C. J. Wet Chemical Synthesis of High Aspect Ratio Cylindrical Gold Nanorods. *J. Phys. Chem. B* **2001**, *105*, 4065–4067.
- (9) Mulvihill, M. J.; Ling, X. Y.; Henzie, J.; Yang, P. Anisotropic Etching of Silver Nanoparticles for Plasmonic Structures Capable of Single-Particle SERS. *J. Am. Chem. Soc.* **2010**, *132*, 268–274.
- (10) Lim, D.-K.; Jeon, K.-S.; Kim, H. M.; Nam, J.-M.; Suh, Y. D. Nanogap-Engineered Raman-Active Nanodumbbells for Single-Molecule Detection. *Nat. Mater.* **2010**, *9*, 60–67.
- (11) Fan, Z.; Govorov, A. O. Plasmonic Circular Dichroism of Chiral Metal Nanoparticle Assemblies. *Nano Lett.* **2010**, *10*, 2580–2587.
- (12) Kuzyk, A.; Schreiber, R.; Fan, Z.; Pardatscher, G.; Roller, E.-M.; Högele, A.; Simmel, F. C.; Govorov, A. O.; Liedl, T. DNA-Based Self-Assembly of Chiral Plasmonic Nanostructures with Tailored Optical Response. *Nature* **2012**, *483*, 311.
- (13) Schreiber, R.; Luong, N.; Fan, Z.; Kuzyk, A.; Nickels, P. C.; Zhang, T.; Smith, D. M.; Yurke, B.; Kuang, W.; Govorov, A. O. Chiral Plasmonic DNA Nanostructures with Switchable Circular Dichroism. *Nat. Commun.* **2013**, *4*, 2948.
- (14) Yan, W.; Xu, L.; Ma, W.; Liu, L.; Wang, L.; Kuang, H.; Xu, C. Pyramidal Sensor Platform with Reversible Chiroptical Signals for DNA Detection. *Small* **2014**, *10*, 4293–4297.
- (15) Kuzyk, A.; Schreiber, R.; Zhang, H.; Govorov, A. O.; Liedl, T.; Liu, N. Reconfigurable 3D Plasmonic Metamolecules. *Nat. Mater.* **2014**, *13*, 862–866.
- (16) Funck, T.; Nicoli, F.; Kuzyk, A.; Liedl, T. Sensing Picomolar Concentrations of RNA Using Switchable Plasmonic Chirality. *Angew. Chem.* **2018**, *130*, 13683–13686.
- (17) Link, S.; El-Sayed, M. A. Spectral Properties and Relaxation Dynamics of Surface Plasmon Electronic Oscillations in Gold and Silver Nanodots and Nanorods. *J. Phys. Chem. B* **1999**, *103*, 8410–8426.
- (18) Becker, J.; Zins, I.; Jakab, A.; Khalavka, Y.; Schubert, O.; Sönnichsen, C. Plasmonic Focusing Reduces Ensemble Linewidth of Silver-Coated Gold Nanorods. *Nano Lett.* **2008**, *8*, 1719–1723.
- (19) Fernanda Cardinal, M.; Rodríguez-González, B.; Alvarez-Puebla, R. A.; Pérez-Juste, J.; Liz-Marzán, L. M. Modulation of Localized Surface Plasmons and SERS Response in Gold Dumbbells through Silver Coating. *J. Phys. Chem. C* **2010**, *114*, 10417–10423.
- (20) Thompson, D. G.; Enright, A.; Faulds, K.; Smith, W. E.; Graham, D. Ultrasensitive DNA Detection Using Oligonucleotide-Silver Nanoparticle Conjugates. *Anal. Chem.* **2008**, *80*, 2805–2810.
- (21) Huang, X.; Neretina, S.; El-Sayed, M. A. Gold Nanorods: From Synthesis and Properties to Biological and Biomedical Applications. *Adv. Mater.* **2009**, *21*, 4880–4910.
- (22) West, P. R.; Ishii, S.; Naik, G. V.; Emani, N. K.; Shalae, V. M.; Boltasseva, A. Searching for Better Plasmonic Materials. *Laser Photonics Rev.* **2010**, *4*, 795–808.
- (23) Pal, S.; Deng, Z.; Ding, B.; Yan, H.; Liu, Y. DNA-Oriami-Directed Self-Assembly of Discrete Silver-Nanoparticle Architectures. *Angew. Chem., Int. Ed.* **2010**, *49*, 2700–2704.
- (24) Weller, L.; Thacker, V. V.; Herrmann, L. O.; Hemmig, E. A.; Lombardi, A.; Keyser, U. F.; Baumberg, J. J. Gap-Dependent Coupling of Ag-Au Nanoparticle Heterodimers Using DNA Origami-Based Self-Assembly. *ACS Photonics* **2016**, *3*, 1589–1595.
- (25) Roller, E.-M.; Besteiro, L. V.; Pupp, C.; Khorashad, L. K.; Govorov, A. O.; Liedl, T. Hotspot-Mediated Non-Dissipative and Ultrafast Plasmon Passage. *Nat. Phys.* **2017**, *13*, 761.
- (26) Yu, D.; Tian, W.; Sun, B.; Li, Y.; Wang, W.; Tian, W. Preparation of Silver-Plated Wool Fabric with Antibacterial and Anti-Mould Properties. *Mater. Lett.* **2015**, *151*, 1–4.
- (27) Liu, M.; Guyot-Sionnest, P. Synthesis and Optical Characterization of Au/Ag Core/Shell Nanorods. *J. Phys. Chem. B* **2004**, *108*, 5882–5888.
- (28) Pande, S.; Ghosh, S. K.; Praharaj, S.; Panigrahi, S.; Basu, S.; Jana, S.; Pal, A.; Tsukuda, T.; Pal, T. Synthesis of Normal and Inverted Gold-Silver Core-Shell Architectures in  $\beta$ -Cyclodextrin and Their Applications in SERS. *J. Phys. Chem. C* **2007**, *111*, 10806–10813.
- (29) Chen, H.; Shao, L.; Li, Q.; Wang, J. Gold Nanorods and Their Plasmonic Properties. *Chem. Soc. Rev.* **2013**, *42*, 2679–2724.
- (30) Xu, H.; Kan, C.; Miao, C.; Wang, C.; Wei, J.; Ni, Y.; Lu, B.; Shi, D. Synthesis of High-Purity Silver Nanorods with Tunable Plasmonic Properties and Sensor Behavior. *Photonics Res.* **2017**, *5*, 27–32.
- (31) Cho, E. C.; Camargo, P. H.; Xia, Y. Synthesis and Characterization of Noble-Metal Nanostructures Containing Gold Nanorods in the Center. *Adv. Mater.* **2010**, *22*, 744–748.
- (32) Pietrobon, B.; McEachran, M.; Kitaev, V. Synthesis of Size-Controlled Faceted Pentagonal Silver Nanorods with Tunable Plasmonic Properties and Self-Assembly of These Nanorods. *ACS Nano* **2009**, *3*, 21–26.
- (33) Ramasamy, P.; Seo, D.-M.; Kim, S.-H.; Kim, J. Effects of TiO<sub>2</sub> Shells on Optical and Thermal Properties of Silver Nanowires. *J. Mater. Chem.* **2012**, *22*, 11651–11657.
- (34) Sasikumar, T.; Ilanchelian, M. Colorimetric Detection of Hypochlorite Based on the Morphological Changes of Silver Nanoprisms to Spherical Nanoparticles. *Anal. Methods* **2017**, *9*, 3151–3158.
- (35) Wiley, B. J.; Im, S. H.; Li, Z.-Y.; McLellan, J.; Siekkinen, A.; Xia, Y. Maneuvering the Surface Plasmon Resonance of Silver Nanostructures through Shape-Controlled Synthesis. *J. Phys. Chem. B* **2006**, *110*, 15666–15675.
- (36) Sun, Y.; Yin, Y.; Mayers, B. T.; Herricks, T.; Xia, Y. Uniform Silver Nanowires Synthesis by Reducing AgNO<sub>3</sub> with Ethylene Glycol in the Presence of Seeds and Poly (Vinyl Pyrrolidone). *Chem. Mater.* **2002**, *14*, 4736–4745.

- (37) Park, K.; Vaia, R. A. Synthesis of Complex Au/Ag Nanorods by Controlled Overgrowth. *Adv. Mater.* **2008**, *20*, 3882–3886.
- (38) Kottmann, J. P.; Martin, O. J.; Smith, D. R.; Schultz, S. Plasmon Resonances of Silver Nanowires with a Nonregular Cross Section. *Phys. Rev. B: Condens. Matter Mater. Phys.* **2001**, *64*, 235402.
- (39) Xiang, Y.; Wu, X.; Liu, D.; Li, Z.; Chu, W.; Feng, L.; Zhang, K.; Zhou, W.; Xie, S. Gold Nanorod-Seeded Growth of Silver Nanostructures: From Homogeneous Coating to Anisotropic Coating. *Langmuir* **2008**, *24*, 3465–3470.
- (40) Jana, N. R.; Gearheart, L.; Murphy, C. J. Seed-Mediated Growth Approach for Shape-Controlled Synthesis of Spheroidal and Rod-Like Gold Nanoparticles Using a Surfactant Template. *Adv. Mater.* **2001**, *13*, 1389–1393.
- (41) Liu, B.; Liu, J. Freezing Directed Construction of Bio/Nano Interfaces: Reagentless Conjugation, Denser Spherical Nucleic Acids, and Better Nanoflakes. *J. Am. Chem. Soc.* **2017**, *139*, 9471–9474.
- (42) Koo, K. M.; Sina, A. A.; Carrascosa, L. G.; Shiddiky, M. J.; Trau, M. DNA-Bare Gold Affinity Interactions: Mechanism and Applications in Biosensing. *Anal. Methods* **2015**, *7*, 7042–7054.
- (43) Hu, S.; Huang, P.-J. J.; Wang, J.; Liu, J. Phosphorothioate DNA Mediated Sequence-Insensitive Etching and Ripening of Silver Nanoparticles. *Front. Chem.* **2019**, DOI: 10.3389/fchem.2019.00198.
- (44) Hartl, C.; Frank, K.; Amenitsch, H.; Fischer, S.; Liedl, T.; Nickel, B. Position Accuracy of Gold Nanoparticles on DNA Origami Structures Studied with Small-Angle X-Ray Scattering. *Nano Lett.* **2018**, *18*, 2609–2615.
- (45) Jette, E. R.; Foote, F. Precision Determination of Lattice Constants. *J. Chem. Phys.* **1935**, *3*, 605–616.
- (46) Berova, N.; Di Bari, L.; Pescitelli, G. Application of Electronic Circular Dichroism in Configurational and Conformational Analysis of Organic Compounds. *Chem. Soc. Rev.* **2007**, *36*, 914–931.
- (47) Guerrero-Martinez, A.; Auguie, B.; Alonso-Gómez, J. L.; Džolić, Z.; Gómez-Graña, S.; Žinić, M.; Cid, M. M.; Liz-Marzán, L. M. Intense Optical Activity from Three-Dimensional Chiral Ordering of Plasmonic Nanoantennas. *Angew. Chem., Int. Ed.* **2011**, *50*, 5499–5503.
- (48) Lee, H.-E.; Ahn, H.-Y.; Mun, J.; Lee, Y. Y.; Kim, M.; Cho, N. H.; Chang, K.; Kim, W. S.; Rho, J.; Nam, K. T. Amino-Acid- and Peptide-Directed Synthesis of Chiral Plasmonic Gold Nanoparticles. *Nature* **2018**, *556*, 360–365.
- (49) Ye, X.; Jin, L.; Caglayan, H.; Chen, J.; Xing, G.; Zheng, C.; Doan-Nguyen, V.; Kang, Y.; Engheta, N.; Kagan, C. R.; Murray, C. B. Improved Size-Tunable Synthesis of Monodisperse Gold Nanorods through the Use of Aromatic Additives. *ACS Nano* **2012**, *6*, 2804–2817.

## 5 Using DNA Origami in Rapid Tests for Signal Amplification

Rapid tests (also lateral flow (immuno)assays (LFAs, LFAs) or point-of-care tests (POC-tests)) are assays which are used to detect analytes such as pathogens, toxins, and biomarkers with a visual read-out.<sup>[54]</sup> The enzyme troponin for instance is a standard biomarker for detecting an acute myocardial infarction (heart attack, AMI).<sup>[108-109]</sup> When a patient has an AMI, time is of the essence. The great advantages of a LFA such as the troponin rapid test include fast detection (5 – 15 min), easy access, low cost, and minimum inconvenience for the patient. Rapid tests can help to rule-in AMI earlier than laboratory-based assays.<sup>[108]</sup> However, laboratory-based assays have lower cut-off values (lowest amount of analyte that can be detected and that is defined as the limit of detection (LOD)) which contributes to a better sensitivity.<sup>[110]</sup>

A viral infection is another example which can be diagnosed using either lateral flow or analytical laboratory assays.<sup>[111]</sup> Particularly at an early stage of the infection when the viral load is still low nucleic acid detection assays such as the real-time reverse transcription polymerase chain reaction (rRT-PCR) are principally more reliable than antigen tests (**Figure 13**).<sup>[112-113]</sup> Here, the virus RNA is transcribed to DNA (reverse transcription) which is then amplified by PCR to achieve a detectable amount. The amount of RNA is determined by monitoring the amplification reaction (in real-time) using fluorescence.<sup>[114]</sup>



**Figure 13.**<sup>[113]</sup> Test sensitivity for low and high sample viral load. Adapted with permission.

The limit of detection for rRT-PCR lies between 100-200 copies/mL. That analytic sensitivity is several orders of magnitude greater than for antigen rapid tests.<sup>[112]</sup> As elaborated in the introduction (**Ch. 1**), there are benefits and drawbacks for both diagnostic tools. Nevertheless, antigen tests are an important complement to rRT-PCR. They are generally faster and require less specialized equipment enabling wider deployment and high throughput screening. Therefore, LFAs can be beneficial in time-critical situations in which the contagiousness of a person must be assessed easily and rapidly on site. The significance of this point has become clear to the majority of people during the Severe Acute Respiratory Syndrome Corona Virus 2 (SARS-CoV-2) pandemic since analytical laboratory tests could not deliver results at the point-of-care.<sup>[66, 113]</sup> Even when time is not critical, being able to move on with diagnosis and treatment is beneficial to the patient.

The lengthy turn-around-time of analytical laboratory tests is because many steps are involved: The process involves sample collection, transportation to laboratory, RNA extraction, rRT-PCR, and last, results communication.<sup>[115]</sup> Further requirements include special biochemical compounds, refrigeration, lab equipment and maintenance, quality control programs and trained personnel. These factors lead to the absence of analytical tests in many areas of the world with less well-developed infrastructure. Therefore,

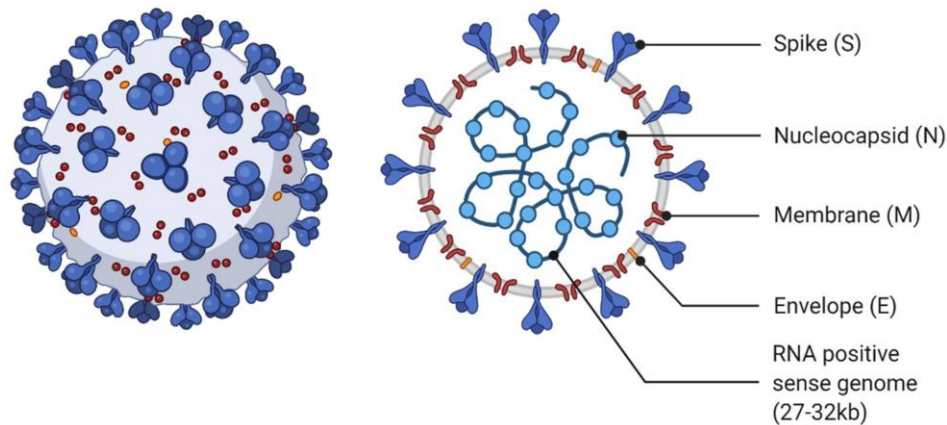
research is constantly focusing on widening the scope and raising the specificity and sensitivity in order to improve the quality and applicability of rapid tests.<sup>[73]</sup>

The general performance of a rapid test is described by its sensitivity and specificity number which is given as a percentage. A test that identifies 98 of 100 infected people has a 98% sensitivity. When 5 of 100 healthy people are identified as false-positive the specificity is 95%. The analytical sensitivity of rRT-PCR varies between laboratories but is almost 100% under optimal laboratory condition however the Robert Koch Institute does not publish these numbers.<sup>[116]</sup> As for rapid tests the clinical numbers must be given by each manufacturer. The World Health Organization (WHO) stated that SARS-CoV-2 antigen rapid tests must have a minimum performance of  $\geq 80\%$  sensitivity and  $\geq 97\%$  specificity.<sup>[117]</sup>

The quality of rapid tests strongly depends on the manufacturer and on what its target is (e.g. drugs, tumor markers).<sup>[112, 118]</sup> As for a SARS-CoV-2 infection the nucleocapsid protein (N protein) has been confirmed as an ideal target for an early diagnostic detection by means of LFA since it is predominantly expressed and produced at high levels within infected cells.<sup>[66, 119]</sup> However, LFAs give no quantitative results of the N protein. rRT-PCR can deliver quantitative results, since the nucleic acid amplification cycle (Ct value) gives an indication of the initial amount of RNA (virus and RNA have a one-to-one relation, cf. **Figure 14**).<sup>[114]</sup> The virus is expected to be abundant in respiratory samples when the rRT-PCR cycle threshold (Ct) is below Ct = 25 (which corresponds to  $\sim 10^6$  RNA copies/mL), and the rapid test sensitivity correspondingly high.<sup>[120]</sup> Therefore, the performance of LFA is best within the first 5 – 7 days of symptoms.

Since viral specific proteins are more abundant and easier to detect than the virus RNA, they are usually favored as biomarkers in rapid tests.<sup>[66]</sup> However, the protein concentration is not sufficient for an early detection of an infection.



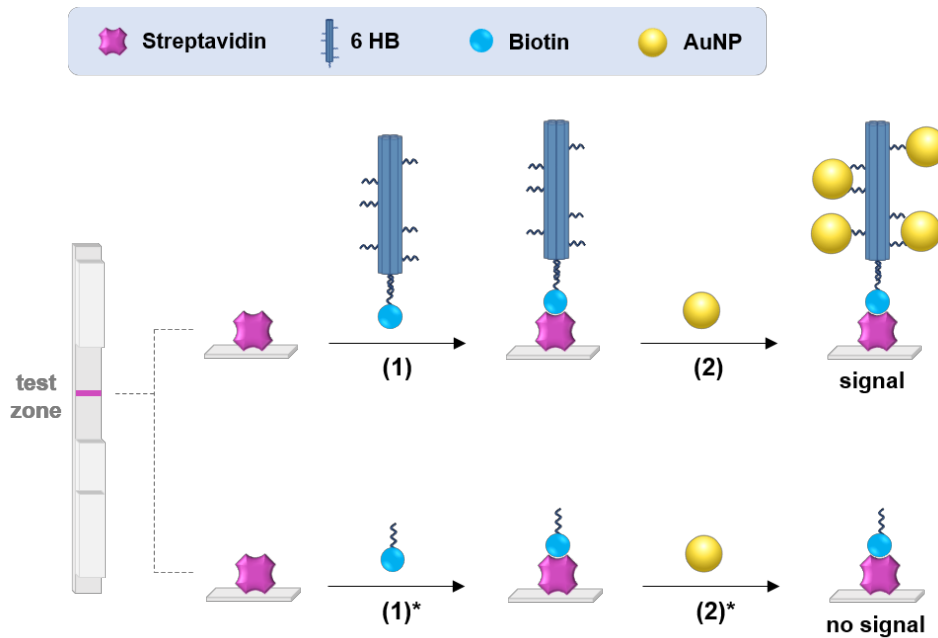


**Figure 14. Scheme of SARS-CoV-2.**<sup>[121]</sup> Adapted with permission.

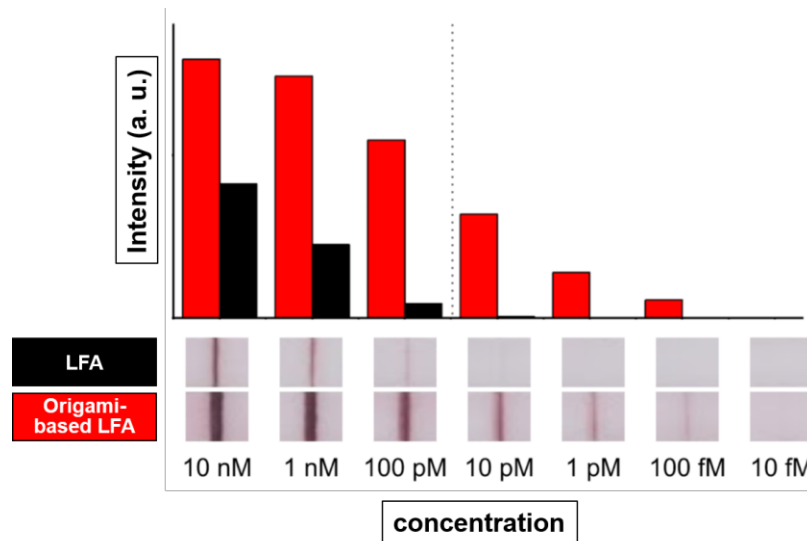
Due to advances in nanotechnology new strategies are steadily developed and employed in lateral flow assays.<sup>[73]</sup> The general technology of LFAs which is simple, at the same time sophisticated and effective, is described in detail in **Ch. 2.3**. In short, the target migrates through a membrane where it binds specifically to a label present in the membrane. Once the target-label conjugate reaches the test zone of the membrane it is immobilized there. Only the labels that are bound to the targets accumulate at the test zone. Labels which did not bind to a target pass the test zone. The labels send a signal with an intensity that is dependent on the nature of the label. The more labels accumulate, the more intense is the signal that is emitted at the test zone. Labels can be for example metal nanoparticles, latex beads, or fluorophores.<sup>[73]</sup> Colloidal gold has proven an excellent label to detect and visualize the presence of biomarkers.<sup>[122]</sup> The most commonly used ones are 40 nm gold nano spheres.<sup>[54]</sup>

The signal and thus the optical behavior of colloidal gold originates from plasmons which are collective electron vibrations (vibrations of the electron plasma).<sup>[93]</sup> The type of metal and the particle's size and shape defines the plasmonic properties and thus the vibration frequency. Plasmons can propagate along the surface of a bulk metal for which they are also called surface plasmons. Surface plasmons of NPs however are confined to the particle, thus they are localized. The plasmon frequency that is specific to each particle size is called the resonance frequency. The localized surface plasmon resonance (LSPR) of 40 nm gold spheres lies in the visual spectral range at  $\sim 510$  nm giving us a red color impression. The LSPR red-shifts and its intensity raises with increasing particle size. The ability to perceive the red color with our eyes is limited by the LSPR intensity which is

dependent on the dielectric constant of gold. The net optical response is a sum of the individual nanoparticle's response. Hence, the higher the nanoparticle concentration, the more intense is the color line and a minimum analyte concentration is required to bind and immobilize a detectable number of NPs at the test zone. However, often the analyte is immersed in a migration solution before being loaded on the test strip which further decreases the analyte concentration.



**Figure 15.** Scheme of DNA origami-based LFA to detect a biotin-labeled DNA target with specific sequence. Streptavidin is pre-immobilized at the test zone of the strip. (1) 6 HB-biotin conjugate (hybridized beforehand) binds to streptavidin. (2) DNA-functionalized AuNPs bind to 6 HB via DNA hybridization. (1)\* and (2)\* control assay without 6 HB to rule out unspecific binding of AuNPs at the test zone.



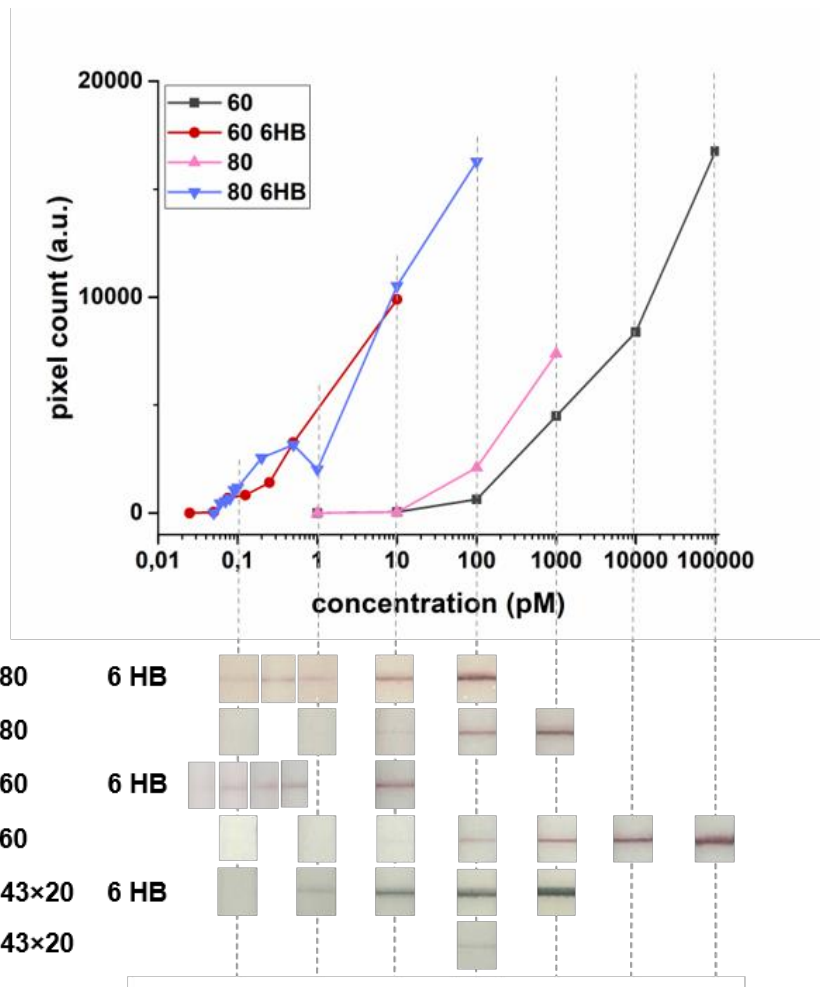
**Figure 16. LFA vs. origami-based LFA. Comparison of signal intensity using 40 nm AuNPs from BBI Solutions and test strips from Milenia Biotech (c.f. Figure 17). Assay design and flow process are shown in Figure 15. Figure by courtesy of Maximilian Urban.**

To improve the rapid test sensitivity, we employed DNA origami to increase the number of AuNPs that were captured at the test zone. Using DNA origami, the target could bind not only one but multiple AuNPs (depending on AuNP size and number of binding sites on the origami). Through the use of a low ratio of NPs, multiple origami could be linked together to form clusters (**Figure 22**) which further increased the number of NPs per target molecule. These large origami-NP clusters showed even stronger signals. The read-out signals were 1000-times enhanced. Without enhancement a minimal analyte concentration of 100 pM was detected. Using the enhancement strategy, a minimal analyte concentration of 100 fM was detected (**Figure 16**). Control tests ensured that there was no signal enhancement in the absence of the analyte in order to rule out unspecific binding.

The signal enhancement strategy is designed to be applied in commercially available rapid tests by simply adding the origami to the flow process. In initial studies commercial test strips “Hybri 2T” were used from Milenia Biotech. Since the company offered strips with pre-immobilized streptavidin at the test zone, a biotin-DNA target was employed in the assay (streptavidin has four binding sites for biotin). An origami structure (6-helix-bundle (6 HB), 3 anchor strands for conjugation with the biotin-DNA target at the tip, 55 anchor strands for conjugation of NPs distributed over the “lateral” origami surface, *cf.* **5.1 Associated Manuscript, Figure 2**) was conjugated to the target via DNA hybridization



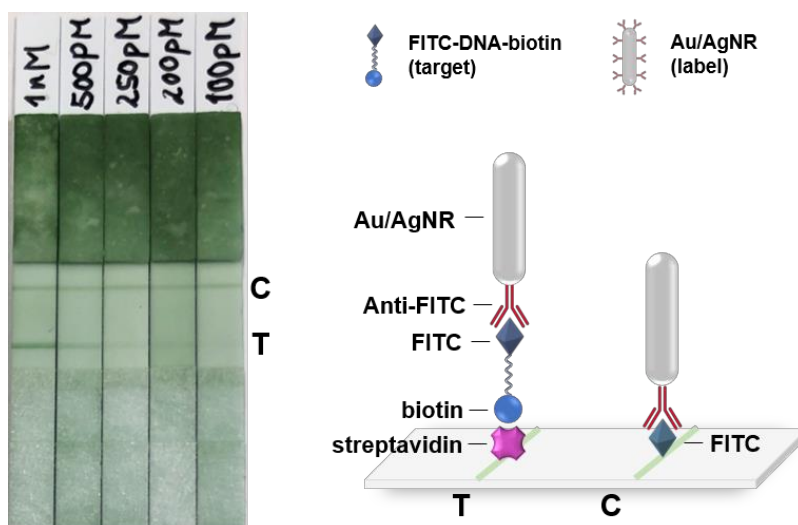
and the whole conjugate was captured at the test zone during the flow process. Finally, 40 nm-AuNPs (other NP sizes see below) were conjugated to the 6 HB for the optical signal. Later, we employed different sizes of spherical and rod-shaped NPs (stated in figure caption) which were captured by the 6 HB (**Figure 17**). A signal enhancement by 2 – 3 orders of magnitude was obtained.



**Figure 17.** LFA detection of 0.1 pM – 10 nM biotin-DNA using 60 nm and 80 nm AuNPs (Sigma Aldrich) and 43 × 20 nm Au/AgNRs with and without 6 HB enhancement (*c.f.* Figure 16). Assay design and flow process are shown in Figure 15.

A detailed protocol is described in the following: The 6 HB was mixed with the biotin-DNA to allow hybridization. For this, a buffer solution containing a final concentration of 20 mM Tris, 100 mM NaCl, 0.1% SDS, and 1 mg/mL BSA with pH 8 was prepared. To 5.5  $\mu$ L of that solution, 3  $\mu$ L of 0.1 M  $MgCl_2$  and 20  $\mu$ L of 2.5 nM 6 HB (in 1 $\times$ TAE, 11 mM  $MgCl_2$ ) was added. Then, 1.5  $\mu$ L of 10, 5, 2.5, 1, 0.5 pM biotin-DNA was added resulting in final concentrations of 250, 125, 75, 50, 25 fM (for other concentrations the biotin-DNA concentration was adjusted keeping the volume constant). The final  $MgCl_2$  concentration

in each sample was 10 mM. The mixture was transferred to the absorption pad and allowed to migrate through the LFA strip which had streptavidin pre-immobilized at the test zone. The 6 HB-DNA-biotin conjugate was captured by the streptavidin via streptavidin-biotin interaction. A washing step was carried out using 40  $\mu\text{L}$  of the initially prepared buffer to wash off residuals and unbound 6 HBs from the membrane. In a last step, 10  $\mu\text{L}$  of  $\sim 10$  nM polyT functionalized NPs (40, 60, 80, 43  $\times$  20 nm) were allowed to migrate through the membrane which were captured by the 6 HB via DNA hybridization (of poly A and poly T strands) which resulted in a colored line at the test zone.

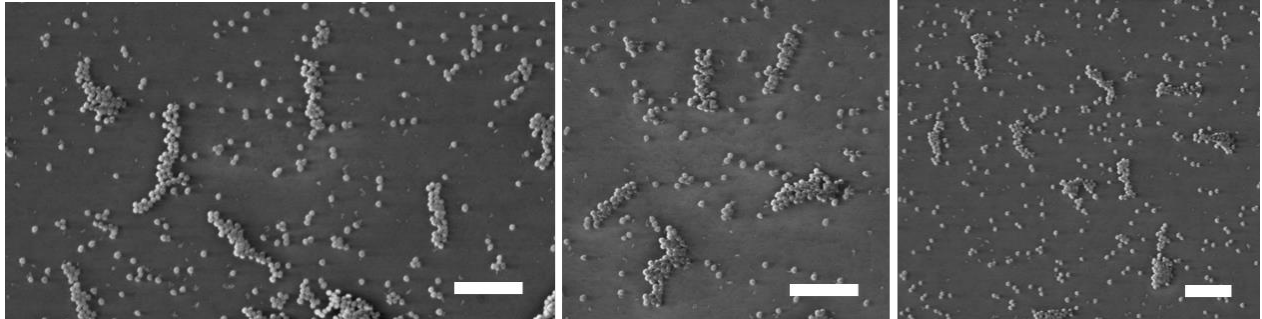


**Figure 18.** LFA detecting FITC-DNA-biotin. Label: 0.8 nM Au/AgNRs (LSPR 680 nm). Test zone with streptavidin pre-immobilized. Control zone with FITC pre-immobilized. Test strips from Microcoat Biotechnology.

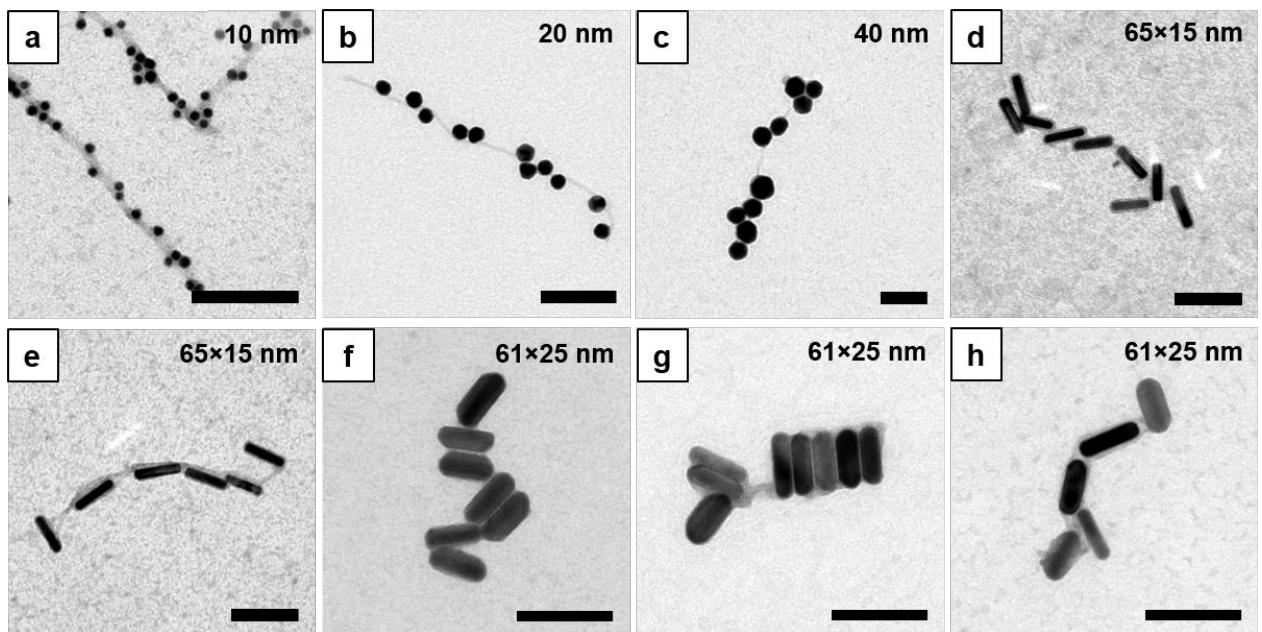
In previous studies, we incorporated our reported bimetallic Au/AgNRs ( $\sim 71$  nm  $\times$  14 nm; LSPR 680 nm) (**Ch. 4.1 Associated Publication 2**) into the lateral flow assay without using the 6 HB for enhancement yet (**Figure 18**). Test strips from Microcoat Biotechnology were used. The assay was designed to detect a FITC-DNA-biotin target (FITC = fluorescein isothiocyanate). Streptavidin was pre-immobilized at the test zone (**T**), while FITC was pre-immobilized at the control zone (**C**). The Au/AgNRs were functionalized with anti-FITC (purchased from Jackson ImmunoResearch) by the passive adsorption method.<sup>[123]</sup> This system showed a detection limit at around 200 pM target concentration. The Microcoat strips had a third zone with pre-immobilized anti-digoxigenin

between the test and control zone. No unspecific binding between anti-FITC and anti-digoxigenin was observed at that zone indicating good specificity.

Au/AgNRs of different colors could be applied in multianalyte testing (multiplex assays).<sup>[59]</sup>



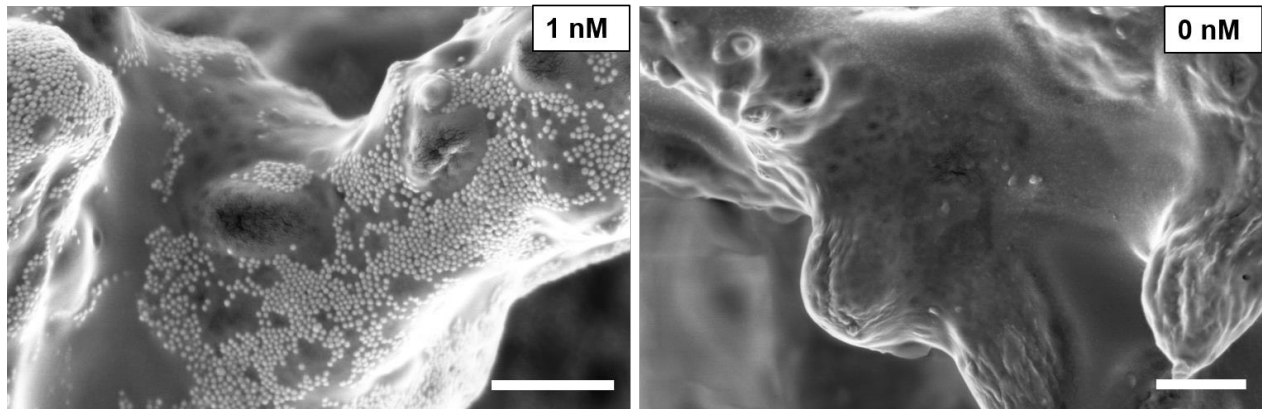
**Figure 19.** SEM micrographs of 40 nm-AuNPs on a glass surface which accumulate to rod-like shapes indicating a successful conjugation between DNA origami and AuNPs. Scale bars are 500 nm. Images by courtesy of Christoph Sikeler.



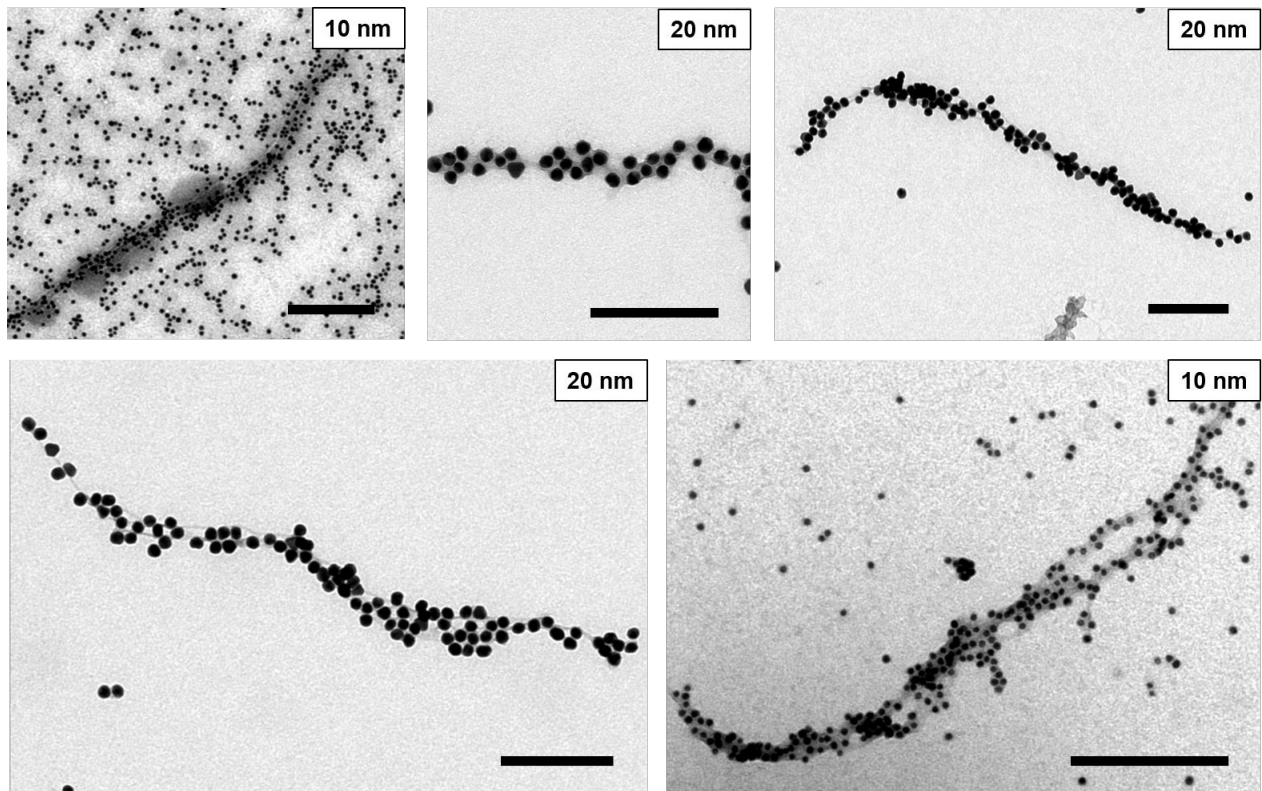
**Figure 20.** TEM micrographs of spherical and rod-shaped NPs attached to 6 HB. (a) – (c) Gold spheres (d) – (e) Gold rods (f) – (h) Gold/silver rods. Scale bars are 100 nm.

To verify the hybridization between the 6 HB and AuNPs, the flow process was mimicked on a glass surface. The 6-helix-bundles were pre-immobilized on the surface via BSA-streptavidin. 40 nm-AuNPs functionalized with DNA were incubated. SEM micrographs show that the AuNPs accumulate on the surface indicating the shape of the DNA origami (**Figure 19**). Further, the hybridization was carried out on a TEM copper grid in order to

subsequently perform TEM analysis (**Figure 20**). Spherical and rod-shaped AuNPs of different sizes as well as Au/AgNRs were used for conjugation.



**Figure 21.** SEM micrographs of the target zone (cellulose membrane). Sample with 1 nM and 0 nM biotin-DNA target. Scale bars are 1  $\mu\text{m}$ . Images by courtesy of Christoph Sikeler.



**Figure 22.** TEM micrographs of 6 HBs and AuNPs forming clusters. Scale bars are 200 nm.

LFA may not replace molecular testing, but their combination will substantially improve diagnostic capabilities. An increased sensitivity can help to provide convenient medical assessment, effective decision making, and early treatment. An early diagnosis reduces

mortality and transmission. The scientific advancement in LFA technology must also meet economic and commercial requirements. Eventually, it must align with the most beneficial features of LFA (low-cost, ease of use, and rapid) to generate a real impact.

## 5.1 Associated Manuscript

# Picomolar Analyte Detection in Lateral Flow Immunoassays by DNA Origami Signal Amplification

Linh Nguyen,<sup>[a]</sup> Christoph Sikeler,<sup>[a]</sup> Stefan van Rest,<sup>[a]</sup> Tim Liedl,<sup>[a]</sup> Philipp Nickels,<sup>[a],\*</sup> Maximilian Urban<sup>[a].\*</sup>

<sup>[a]</sup> Faculty of Physics and Center for NanoScience (CeNS), Ludwig-Maximilians-University, Geschwister-Scholl-Platz 1, 80539 Munich, Germany.

E-mail: urban.max@physik.uni-muenchen.de

KEYWORDS: DNA origami, self-assembly, lateral flow immunoassay, plasmonic nanoparticles

### **Abstract**

*The COVID-19 pandemic has revealed the urgent need for quick, reliable, easy to handle, and sensitive diagnostic methods. Lateral flow assays (rapid tests) have proven to be a powerful tool in the combat against the spread of COVID-19. Their cheap and easy application and direct read-out make them ideal for point-of-care (POC) diagnostics. However, the advantages of these tests still come at the cost of reliability and analytical performance while more time-consuming laboratory tests are still the gold-standard in the field. Here, we present a strategy for improving the reliability of rapid tests by employing DNA origami to provide high control over target recognition and sensitivity. By virtue of this strategy, the detection limit of a rapid test could be shifted from the nanomolar to the picomolar concentration region.*

Rapid tests (also referred to as lateral flow (immuno)assays, LFA) were first commercially launched in 1984 by Unipath.<sup>[1]</sup> They are a simple, yet very sophisticated system to detect and quantify analytes.<sup>[2-3]</sup> Rapid tests are used for clinical analysis, the detection of

toxins<sup>[4-5]</sup> and pathogens<sup>[6-8]</sup> as well as pesticides<sup>[9-11]</sup> and drugs<sup>[12-14]</sup>. Small sample volumes and no sample preparation are required while an easy to analyze visual read-out is obtained after a few minutes. Ecological factors such as low material cost and energy consumption add to their unparalleled advantages as an analytic method for sample containing analytes with nanomolar concentration.<sup>[15]</sup>

However, for low target concentrations (picomolar region) the reliability of rapid tests decreases dramatically with decreasing target concentration. The development of rapid tests capable of detecting targets within the picomolar range would be greatly beneficial to global healthcare providers.<sup>[16]</sup> LFAs can provide point-of-care diagnostics making sample processing and transportation and difficult lab set-ups obsolete, particularly improving diagnostic services in the developing world due to suboptimal infrastructure and resources. Therefore, increasing the sensitivity of rapid while ensuring safety and reliability addresses a real-world problem.

The design of a rapid test is simple.<sup>[17]</sup> A paper-based test strip is encased by a plastic cassette (**Figure 1, right**). The sample can be applied to the hole in the cassette which gives access to the absorption pad of the test strip. It then sequentially moves through several compartments on the strip by virtue of capillary forces. After passing the conjugation pad and migrating through the nitrocellulose membrane, the sample finally gets absorbed by the waste pad. The system is based on specific binding events between biomolecules: While migrating through the strip, the analyte interacts with particles and molecules which are dispersed and pre-immobilized on the strip. The qualitative read-out consists of a colored line that is observed by naked eye. The target concentration at which a distinct line can still be observed determines the level of sensitivity. The colored line consists of so-called “labels” which are responsible for the color impression. The target itself is not visible; therefore, it is marked with the label for the visual detection. The label is dispersed on the conjugation pad and conjugates the target once it passes through. The most common labels are gold nanoparticles (AuNPs) which appear as a red line at the test zone. Once the target-label conjugate reaches the test zone, it is captured by pre-immobilized molecules. Hence, target and label concentrate at the test zone during the flow process.

Usually, a target molecule has one binding site for binding one label. By increasing the number of labels per target molecule, the intensity of the red line can be increased. This strategy to improve assay sensitivity has recently been implemented in different ways.<sup>[15]</sup>

For example, complementary oligonucleotides were used to conjugate multiple AuNPs to the target which led to a 2.5-fold improved sensitivity in HIV nucleic acid LFA.<sup>[18]</sup> Further, using dendrimers to assemble gold multimers led to a 20-fold higher sensitivity<sup>[19]</sup> and using silica nanorods coated with colloidal gold achieved a 50-fold signal enhancement in the detection of rabbit IgG.<sup>[20]</sup> A label, composed of many small (16 nm) gold labels bound to individual chitosan-coated Fe<sub>2</sub>O<sub>3</sub> nanoparticles improved sensitivity 3-fold in an aflatoxin B<sub>2</sub> assay.<sup>[21]</sup>

The significance of this work is to introduce a DNA origami structure which can bind to the target as well as to a multitude of AuNPs improving the detection limit by four orders of magnitude. The DNA structure is assembled using the DNA origami technique<sup>[22]</sup> that is capable of arranging inorganic nanoparticles with specific distance, direction, and order which is beneficial for tuning the optical signal.<sup>[23]</sup> The enhancement system is designed to be added to commercially available LFAs.

## Results

For developing our method, a setup for testing for pregnancy was chosen due to convenience, accessibility, and variety. The enhancement strategy was carried out using the pregnancy test One+Step<sup>®</sup>. The pregnancy test detects human chorionic gonadotropin (hCG) which is a hormone elevated during pregnancy. The hCG was produced from a sterile preparation of placental glucoprotein (source: urine of post-menopausal women). The purchased lyophilized powder was reconstituted in MilliQ water with 0.1% bovine serum albumin (BSA).

To improve the rapid test sensitivity, we employ a DNA origami structure to increase the number of AuNPs that are captured at the test zone. By binding to a AuNP-functionalized DNA origami structure, the target can bind not only one but multiple AuNPs (depending on AuNP size and DNA origami design). The DNA structure used consists of a 6-helix-bundle (~ 414 × 7 nm) with 55 DNA anchor strands (poly A<sub>15</sub>) for the conjugation of 40-nm AuNPs functionalized with poly T<sub>8-25</sub> (**Figure 2**).

Before applying the 6 HB origami in the One+Step<sup>®</sup> test, the original One+Step<sup>®</sup> labels (AuNPs) were removed from the conjugation pad. A sample containing hCG was allowed to migrate through the test strip by applying it to the absorption pad. Once the sample reached the test zone, hCG was captured by pre-immobilized anti-hCG (**Figure 3**). Then,



6 HBs that were previously conjugated to anti-hCG were added. The 6 HB-anti-hCG conjugates were captured by hCG at the test zone. In a last step, DNA-functionalized AuNPs were added to the flow process to be subsequently captured by the 6 HBs via base pair hybridization. Between all steps, a washing step was carried out using MilliQ water to flush excess and unbound hCG and 6 HBs from the membrane.

Using DNA origami, a minimal concentration of 0.1 pM was detected (**Figure 1**), whereas without enhancement, a minimal concentration of 1 nM was detected, therefore showing an increase in sensitivity by a factor of  $10^4$ . Control tests ensured that there was no signal enhancement in the absence of the analyte in order to rule out unspecific binding. In reference studies the original testing system was not changed. The process was carried out without addition of our enhancement DNA structure: 5  $\mu$ L of hCG (100 pM, 1 nM, 10 nM, 25 nM) were added to the absorption pad (**Figure 1**). Subsequently, 20  $\mu$ L MilliQ water was added to enable a good flow through the membrane. The original AuNPs of the pregnancy test are responsible for the obtained signal.

Since the hybridization between 6 HB and AuNPs was carried out in a flow process, the incubation time was difficult to control. Hybridization kinetics are an important factor affecting the quality of the assay which can also be influenced by ionic strength of the solution. To confirm the hybridization, the 6 HBs and NPs were mixed and immediately transferred to a TEM grid for analysis. The TEM images of the DNA origami-NPs assemblies (**Figure 2b**) suggest a very fast hybridization process within the time frame of seconds. In addition, hybridization was also performed on a glass surface for SEM analysis (**Figure 2c**). The AuNPs accumulate to rod-like shapes indicating a successful conjugation between DNA origami structures and AuNPs.

## Discussion

A problem that often occurs is non-specific binding between the label and the capture antibody at the test zone. This raises false positive results and lowers the specificity of the assay. Blocking mechanisms using BSA can reduce this issue by saturating the excess protein binding sites making the antibody more affine only to its specific antigen.<sup>[24]</sup> In the presented method AuNPs are coated with DNA which circumvents that problem. There might be a non-specific binding between the anti-hCG at the test zone with the anti-hCG bound to the DNA structure. However, a non-specific binding was not observed. This could

be due to the fact that 0.1% BSA was allowed to first migrate through the membrane along with hCG which blocked the left-over binding sites before anti-hCG was applied to the strip.

It may be discussed if it is of higher clinical relevance to develop signal amplification using e.g. the troponin I rapid test that is used for detecting a myocardial infarction.<sup>[25]</sup> Since only a small number of manufacturers produce troponin I tests, its limited access and variety would have impeded a fast development of the presented technology.

While searching for better detection systems and strategies for signal amplification, attention should also be paid to the strip components. Pregnancy tests of different manufacturers vary in membrane and pad material as well as pore size and texture thereof. These features are very important for obtaining desired diffusion rates, hydrophobicity, and successful conjugation while avoiding undesired interactions and physical adsorption to the membrane. Testing a great variety of manufacturers is important, especially when new parameters are added to a working system. Therefore, the hCG test was favored over the troponin test and other LFAs. Some manufacturers showed poor surface passivation which resulted in suboptimal flow properties and surface interactions, as well as NP aggregation.

Techniques for improving LFA sensitivity often require multiple steps and longer assay times.<sup>[15]</sup> The presented enhancement strategy adds to the assay time, assay complexity, and assay cost, since additional steps must be performed to deliver strong signals. Therefore, balancing further improvement in sensitivity and number of steps involved remains a major challenge. An advantage of sequential flow is that the immunoreactions are faster when the antigen first binds with a capture antibody and then a conjugated label.<sup>[26]</sup> When the label binds the antigen first and before the capturing process happens, in our case meaning a 6 HB covered with AuNPs migrating towards the test zone, diffusion issues can arise. In typical one-step systems large labels have shown limited diffusion.<sup>[27]</sup> A one-step process with our enhancement method led to aggregation of the sample components upon entering the nitrocellulose membrane.

## Materials and Methods

DNA and modified DNA were purchased from Eurofins Genomics (Ebersberg, Germany) and Biomers. HybriDetect lateral flow strips were purchased from Milenia biotec. AuNPs

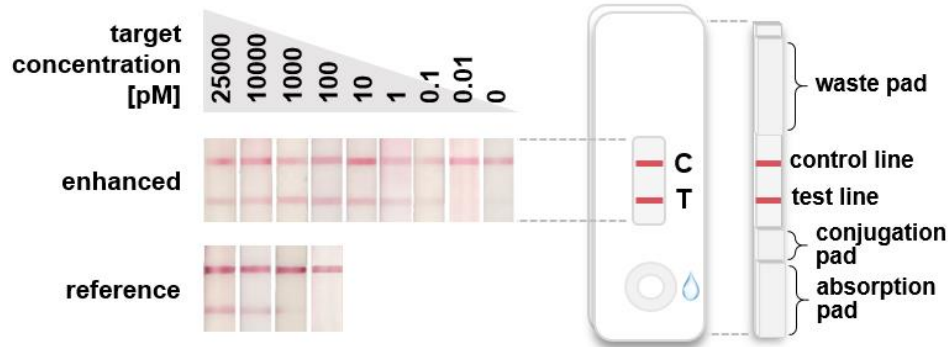
were purchased from BBI. Magnesium chloride, Tris, acetic acid and Ethylenediaminetetraacetic acid (EDTA) were purchased from Carl Roth GmbH & Co. KG (Karlsruhe, Germany). Human chorionic gonadotropin (hCG) was purchased from GENAXXON, Cat# C6051.2500, 36.7 kDa,  $1 \frac{mg}{mL}$ , 27.25  $\mu$ M. Anti-hCG beta subunit was ordered from antibodies-online.com, ABIN6391425, 23 kDa,  $7.11 \frac{mg}{mL}$ , 309  $\mu$ M. One+Step<sup>®</sup> pregnancy test was purchased from time4baby.de. Bovine serum albumin (BSA, BioReagent) was purchased from Sigma Aldrich.

### **Using DNA origami in a lateral flow assay (pregnancy test)**

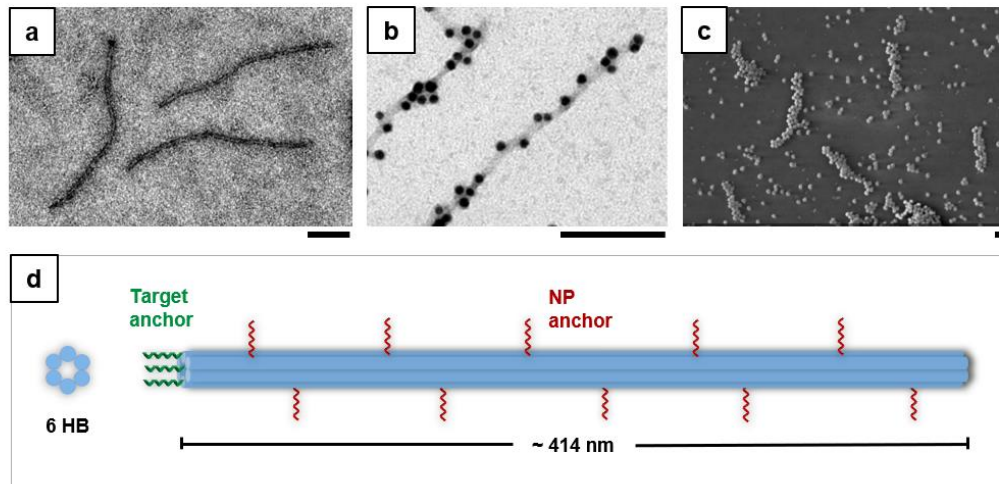
First, the test strip was prepared: The conjugation pad was removed and the absorption pad was moved to create a 1-mm overlap with the remaining nitrocellulose membrane. The following substances were slowly and successively pipetted onto the absorption pad: 5  $\mu$ L hCG (in concentrations of 25 nM, 10 nM, 1 nM, 100 pM, 10 pM, 1 pM, 0.1 pM, and 0.01 pM, respectively; reconstituted in MilliQ water with 0.1% BSA), 5 – 10  $\mu$ L MilliQ H<sub>2</sub>O, 3  $\mu$ L 6HB@anti-hCG (20  $\mu$ L 23 nM 6 HB (in 1×TAE 11 mM MgCl<sub>2</sub>) + 1.5  $\mu$ L 9  $\mu$ M anti-hCG (in PBS buffer pH 7.4)), 5 – 10  $\mu$ L MilliQ H<sub>2</sub>O, 1 – 2  $\mu$ L AuNPs (40 nm, ~ 10 nM in 0.1% SDS), and 15  $\mu$ L 10 mM MgCl<sub>2</sub>. To ensure good flow through the membrane, the liquid must be absorbed by the waste pad completely before the next substance was added.

## **Conclusion**

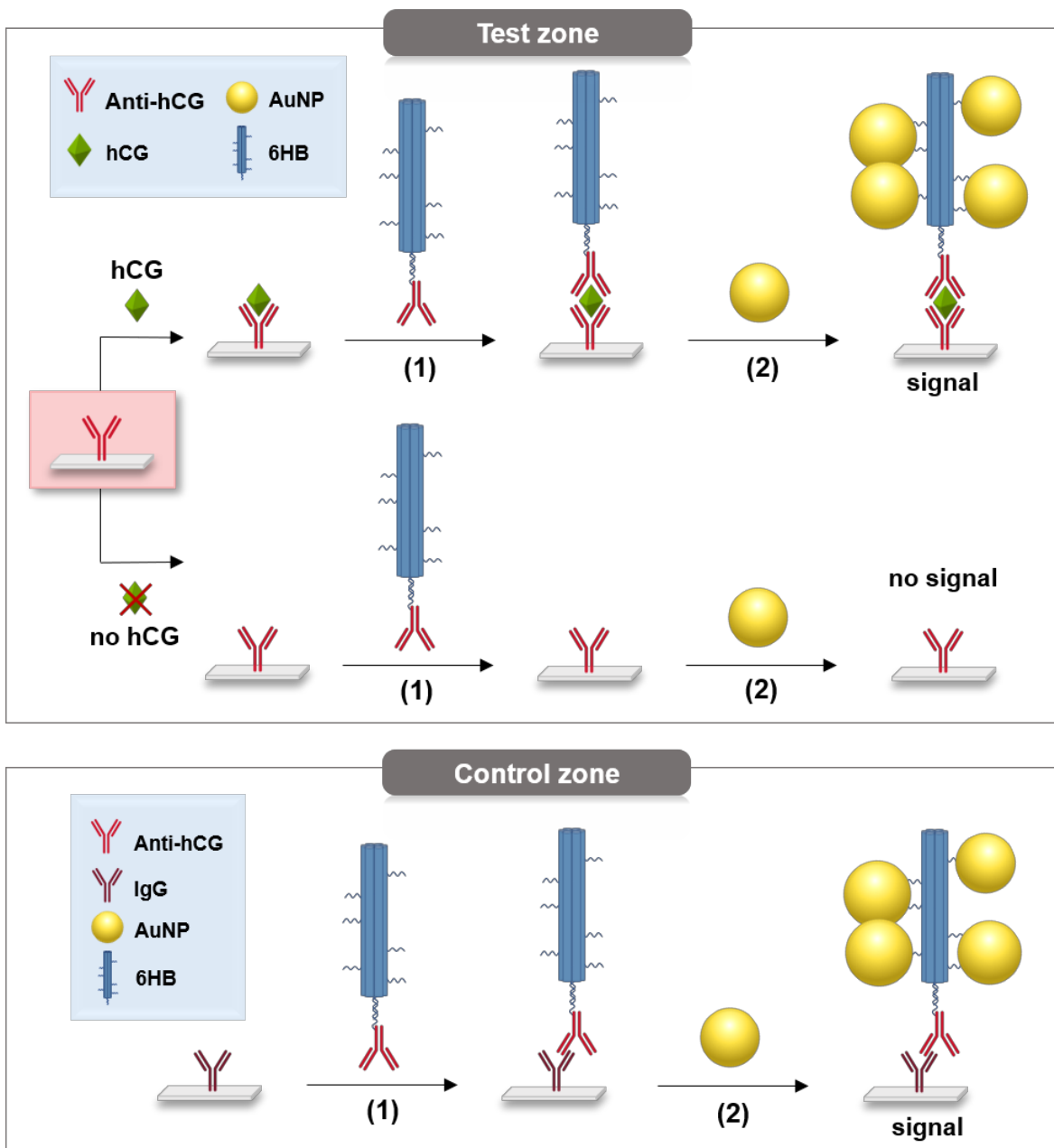
Improving the performance of point-of-care rapid tests towards higher sensitivity is essential for modern health care. It is crucial to overcome the limitations of LFA in regard to early diagnosis. We demonstrated a strategy to enhance the sensitivity of a LFA by using a DNA origami structure for signal amplification. The strategy involves the DNA structure acting as a linker between the target (pregnancy hormone hCG in the presented case) and the label. It captures an increased number of AuNPs at the test zone giving rise to a recognizable red line even at 10<sup>4</sup> times lower target concentrations. This result contributes to the development of high sensitivity LFAs. Future work will include the optimization and application of this strategy for detecting different analytes. Continuing improvements of this technology will expand the overall utility of LFAs.



**Figure 1.** Visual read out of LFA (pregnancy test; target: hCG) with and without signal enhancement using DNA origami. AuNPs from BBI were used for the assay with enhancement. The assay without enhancement corresponds to the original assay from the manufacturer. Right: Test strip components.



**Figure 2.** (a) TEM image of 6 HB. (b) TEM image of 6 HB with 10 nm AuNPs attached. (c) SEM image of 6 HB with 40 nm AuNPs attached. Scale bars are 100 nm. (d) Front and side view of 6 HB (3 DNA anchors for hybridization with anti-hCG and 55 anchors for NP conjugation).



**Figure 3. Test zone (in presence and absence of hCG): Step (1): The 6 HB origami binds via antigen-antibody interaction when hCG is present. No binding when hCG is not present. Step (2): AuNPs bind to the origami via DNA hybridization. Control zone: Step (1): The 6 HB origami binds via non-specific antigen-antigen interaction. Step (2): AuNPs bind to the origami via DNA hybridization.**

## References

- [1] W. C. Mak, V. Beni, A. P. Turner, "Lateral-Flow Technology: From Visual to Instrumental", *Trends in Analytical Chemistry*, **2016**.
- [2] M. Jauset-Rubio, M. Svobodová, T. Mairal, C. McNeil, N. Keegan, A. Saeed, M. N. Abbas, M. S. El-Shahawi, A. S. Bashammakh, A. O. Alyoubi, C. K. O'Sullivan, "Ultrasensitive, Rapid and Inexpensive Detection of DNA Using Paper Based Lateral Flow Assay", *Scientific Reports*, **2016**.
- [3] G. A. Posthuma-Trumpie, J. Korf, A. van Amerongen, "Lateral Flow (Immuno)Assay: Its Strengths, Weaknesses, Opportunities and Threats. A Literature Survey", *Analytical and Bioanalytical Chemistry*, **2009**.
- [4] B. Ngom, Y. Guo, X. Wang, D. Bi, "Development and Application of Lateral Flow Test Strip Technology for Detection of Infectious Agents and Chemical Contaminants: A Review", *Analytical and Bioanalytical Chemistry*, **2010**.
- [5] R. Wong, H. Tse, *Lateral Flow Immunoassay*, Springer Science & Business Media, **2008**.
- [6] S. Shan, W. Lai, Y. Xiong, H. Wei, H. Xu, "Novel Strategies To Enhance Lateral Flow Immunoassay Sensitivity for Detecting Foodborne Pathogens", *Journal of Agricultural and Food Chemistry*, **2015**.
- [7] P. Wu, F. Xue, W. Zuo, J. Yang, X. Liu, H. Jiang, J. Dai, Y. Ju, "A Universal Bacterial Catcher Au-PMBA-Nanocrab-Based Lateral Flow Immunoassay for Rapid Pathogens Detection", *Analytical Chemistry*, **2022**.
- [8] A. Brunauer, R. D. Verboket, D. M. Kainz, F. von Stetten, S. M. Früh, "Rapid Detection of Pathogens in Wound Exudate via Nucleic Acid Lateral Flow Immunoassay", *Biosensors*, **2021**.
- [9] M. D. L. Jara, L. A. C. Alvarez, M. C. C. Guimarães, P. W. P. Antunes, J. P. de Oliveira, "Lateral Flow Assay Applied to Pesticides Detection: Recent Trends and Progress", *Environmental Science and Pollution Research*, **2022**.
- [10] C. Liu, Q. Jia, C. Yang, R. Qiao, L. Jing, L. Wang, C. Xu, M. Gao, "Lateral Flow Immunochromatographic Assay for Sensitive Pesticide Detection by Using Fe<sub>3</sub>O<sub>4</sub> Nanoparticle Aggregates as Color Reagents", *Analytical Chemistry*, **2011**.



- [11] S. Z. Hossain, R. E. Luckham, M. J. McFadden, J. D. Brennan, "Reagentless Bidirectional Lateral Flow Bioactive Paper Sensors for Detection of Pesticides in Beverage and Food Samples", *Analytical Chemistry*, **2009**.
- [12] A. Carrio, C. Sampedro, J. L. Sanchez-Lopez, M. Pimienta, P. Campoy, "Automated Low-Cost Smartphone-Based Lateral Flow Saliva Test Reader for Drugs-of-Abuse Detection", *Sensors*, **2015**.
- [13] N. V. Guteneva, S. L. Znoyko, A. V. Orlov, M. P. Nikitin, P. I. Nikitin, "Rapid Lateral Flow Assays Based on the Quantification of Magnetic Nanoparticle Labels for Multiplexed Immunodetection of Small Molecules: Application to the Determination of Drugs of Abuse", *Microchimica Acta*, **2019**.
- [14] Z. Qriouet, Y. Cherrah, H. Sefrioui, Z. Qmichou, "Monoclonal Antibodies Application in Lateral Flow Immunochromatographic Assays for Drugs of Abuse Detection", *Molecules*, **2021**.
- [15] Y. Liu, L. Zhan, Z. Qin, J. Sackrison, J. C. Bischof, "Ultrasensitive and Highly Specific Lateral Flow Assays for Point-of-Care Diagnosis", *ACS Nano*, **2021**.
- [16] P. Yager, T. Edwards, E. Fu, K. Helton, K. Nelson, M. R. Tam, B. H. Weigl, "Microfluidic Diagnostic Technologies for Global Public Health", *Nature*, **2006**.
- [17] P. Chun, in *Lateral Flow Immunoassay*, Springer, **2009**, pp. 1-19.
- [18] J. Hu, L. Wang, F. Li, Y. L. Han, M. Lin, T. J. Lu, F. Xu, "Oligonucleotide-Linked Gold Nanoparticle Aggregates for Enhanced Sensitivity in Lateral Flow Assays", *Lab on a Chip*, **2013**.
- [19] G. Shen, H. Xu, A. S. Gurung, Y. Yang, G. Liu, "Lateral Flow Immunoassay with the Signal Enhanced by Gold Nanoparticle Aggregates Based on Polyamidoamine Dendrimer", *Analytical Sciences*, **2013**.
- [20] H. Xu, J. Chen, J. Birrenkott, J. X. Zhao, S. Takalkar, K. Baryeh, G. Liu, "Gold-Nanoparticle-Decorated Silica Nanorods for Sensitive Visual Detection of Proteins", *Analytical Chemistry*, **2014**.
- [21] D. Tang, J. Saucedo, Z. Lin, S. Ott, E. Basova, I. Goryacheva, S. Biselli, J. Lin, R. Niessner, D. Knopp, "Magnetic Nanogold Microspheres-Based Lateral-Flow Immunodipstick for Rapid Detection of Aflatoxin B<sub>2</sub> in Food", *Biosensors Bioelectronics*, **2009**.
- [22] P. W. Rothmund, "Folding DNA to Create Nanoscale Shapes and Patterns", *Nature Communications*, **2006**.

- [23] B. Ding, Z. Deng, H. Yan, S. Cabrini, R. N. Zuckermann, J. Bokor, "Gold Nanoparticle Self-Similar Chain Structure Organized by DNA Origami", *Journal of the American Chemical Society*, **2010**.
- [24] Y. Xiao, S. N. Isaacs, "Enzyme-Linked Immunosorbent Assay (ELISA) and Blocking with Bovine Serum Albumin (BSA)—Not All BSAs are Alike", *Journal of Immunological Methods*, **2012**.
- [25] D. Lou, L. Fan, Y. Cui, Y. Zhu, N. Gu, Y. Zhang, "Fluorescent Nanoprobes with Oriented Modified Antibodies to Improve Lateral Flow Immunoassay of Cardiac Troponin I", *Analytical Chemistry*, **2018**.
- [26] T. Liang, R. Robinson, J. Houghtaling, G. Fridley, S. A. Ramsey, E. Fu, "Investigation of Reagent Delivery Formats in a Multivalent Malaria Sandwich Immunoassay and Implications for Assay Performance", *Analytical Chemistry*, **2016**.
- [27] L. Zhan, S.-z. Guo, F. Song, Y. Gong, F. Xu, D. R. Boulware, M. C. McAlpine, W. C. W. Chan, J. C. Bischof, "The Role of Nanoparticle Design in Determining Analytical Performance of Lateral Flow Immunoassays", *Nano Letters*, **2017**.

## 6 Appendix

### 6.1 Supporting Information for Publication 1



Supporting Information

#### **DNA-Origami-Templated Silica Growth by Sol–Gel Chemistry**

*Linh Nguyen, Markus Döblinger, Tim Liedl, and Amelie Heuer-Jungemann\**

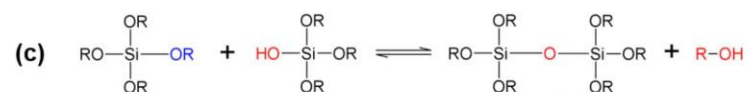
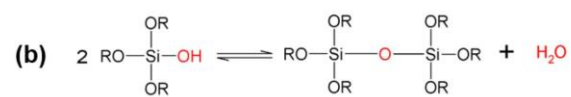
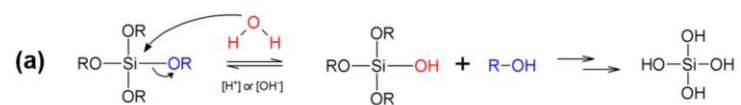
anie\_201811323\_sm\_miscellaneous\_information.pdf

## Supporting Information

SUPPORTING INFORMATION FOR ACCEPTED ARTICLE

### Reaction mechanism of Silica Synthesis

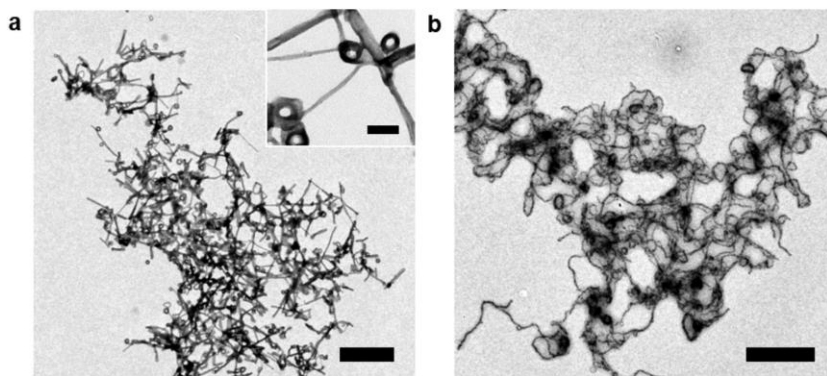
The sol-gel process of alkoxy silanes is described in three reactions:



**Scheme S1.** Chemical reactions describing the sol-gel mechanism. (a) Hydrolysis (b) Water condensation (c) Alcohol condensation.

### Initial Silica Coating Studies

Silica growth was first performed on dsDNA, following a literature protocol.<sup>[4]</sup> DNA was dissolved in water followed by the addition of TMAPS and TEOS. After 6 - 8 days of silica growth under ambient and static condition, the silicified DNA was characterized by electron microscopy (**Figure S1**).

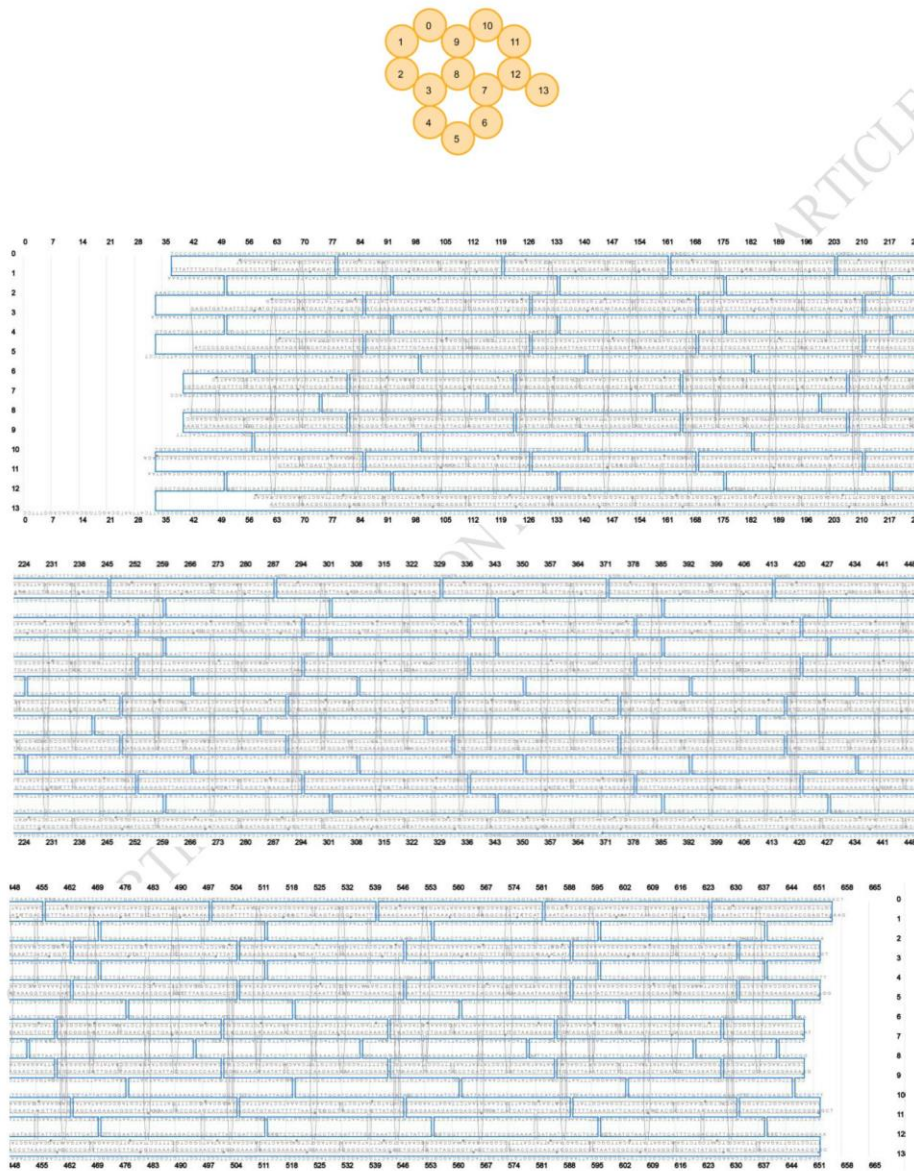


**Figure S1.** Silica mineralization of dsDNA in water. (a) TEM micrographs show the silica mineralized dsDNA after 7 days of silica growth and (b) after sonication for 5 min. Scale bars are 2  $\mu\text{m}$  for (a), 200 nm for the inset and 1  $\mu\text{m}$  for (b).

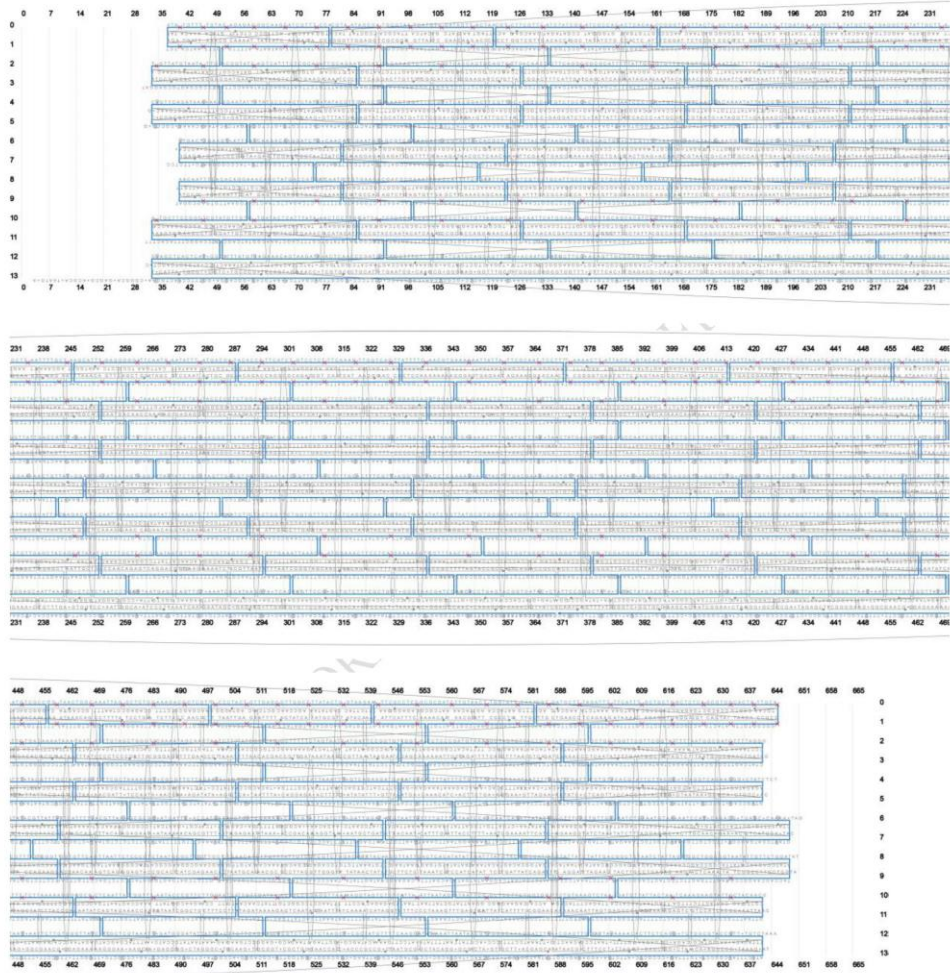
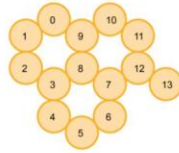


## Design and formation of DNA origami

DNA origami structures were designed using the CaDNAno software<sup>[1]</sup> (design schematics in **Figure S2** and **S3**).



**Figure S2.** CaDNAno scaffold and staple paths and sequences of 14 HB rod structure.



**Figure S3.** CaDNAno scaffold and staple paths and sequences of 14 HB ring structure.

## Materials and Methods

### Chemicals

Unless stated otherwise, all chemicals were used as received. Tetraethoxysilane 98 %, MgCl<sub>2</sub> 98 % and DNA sodium salt (from salmon testes) were obtained from Sigma Aldrich, Trimethyl(3-(trimethoxysilyl)propyl)ammonium chloride (50 % in methanol) was obtained from TCI America. Oligonucleotides were obtained from Eurofins Genomics. DNase I was obtained from Roche. 10×DNase I buffer was obtained from New England Biolabs.

### Folding and Purification of DNA origami structures

*14 HB rod:* The 14 HB rod structure was folded using 10 nM of the scaffold p8634, 100 nM of each staple strand in buffer containing 10 mM Tris, 1 mM EDTA (pH = 8) and 16 mM MgCl<sub>2</sub>. The mixture was heated to 65 °C and held at this temperature for 30 min, then slowly cooled down to 5 °C over a period of 54 hours.

*14 HB ring:* The structure was folded using 10 nM of the scaffold p8634, 100 nM of each staple strand, 10 mM Tris, 1 mM EDTA (pH = 8) and 16 mM MgCl<sub>2</sub>. The solution was then heated to 65 °C and immediately cooled to 5 °C over the course of 43 hours.

*3D DNA Origami Crystals:* 3D DNA Origami lattices were formed according to our previously published protocol.<sup>[2]</sup>

All folded DNA origami structures were purified from excess staple strands by one round of PEG precipitation<sup>[3]</sup> and re-dispersion in buffer or water containing low concentrations of MgCl<sub>2</sub>. In brief, the origami folding mixture was mixed in a 1:1 volumetric ratio with 2×PEG buffer (15 % w/v PEG (MW: 8000 g/mol), 500 mM NaCl, 2×TE) and centrifuged at 16,000 rcf for 30 min. The supernatant was discarded, and the remaining DNA pellet was re-

dissolved in water/ an aqueous solution of 0.5 - 3 mM MgCl<sub>2</sub>, mixed by pipetting until the pellet fully disappeared and finally shaken overnight at 500 rpm and 37 °C.

Silica shell growth

For silica growth the two silanes TMAPS and TEOS were added to the origami molecules in a ratio of 1 phosphate group / nucleotide : 1 TMAPS : 15 TEOS. While TMAPS acts as a co-structure directing agent, polycondensation of TEOS leads to the formation of a silica network. For silica growth 80 µL of DNA origami structures (25 - 500 nM) were mixed with 0.176 µL of TMAPS (50 % in methanol). The mixture was then shaken at 350 rpm for 1 min, after which 0.848 µL of TEOS were added followed by shaking for another 15 min. Finally, the mixture was kept undisturbed for up to 7 days. For lower concentrations of DNA origami (> 100 nM), both TMAPS and TEOS were diluted in MeOH in a 1:1 ratio.

SUPPORTING INFORMATION FOR ACCEPTED ARTICLE

**Characterization techniques**

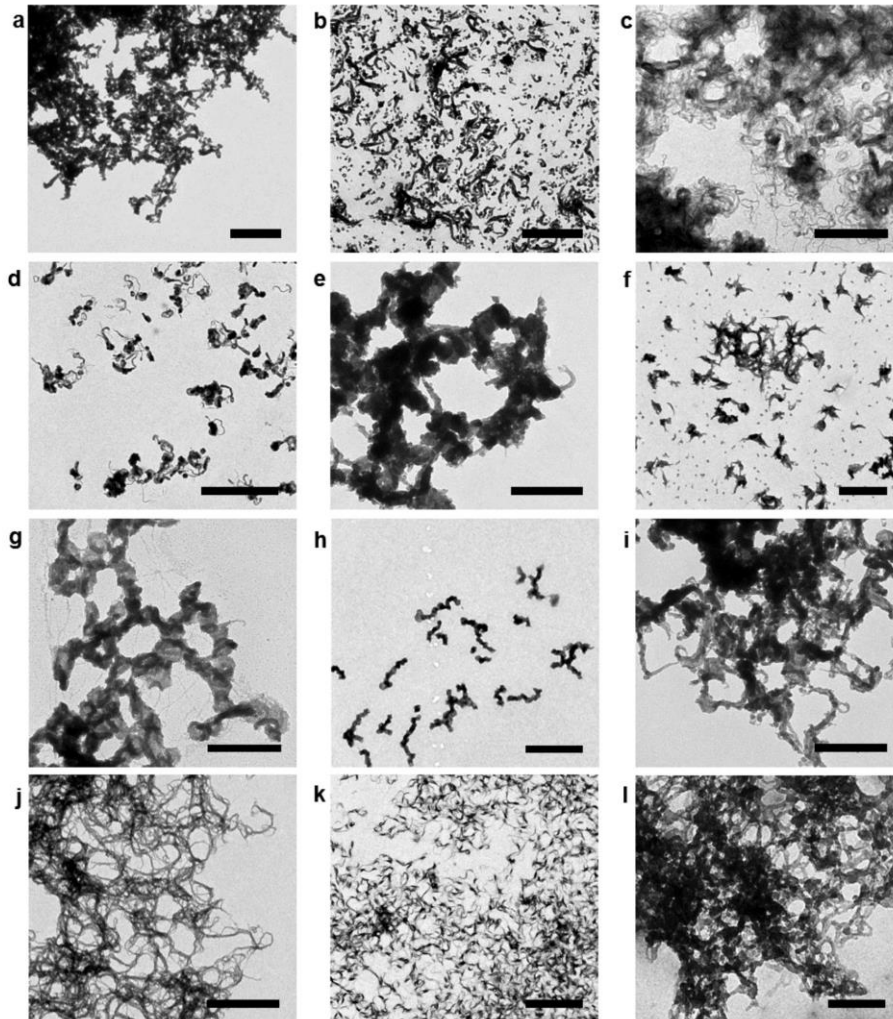
*Transmission Electron Microscopy:* TEM imaging of DNA origamis was carried out using a JEM-1011 transmission electron microscope (JEOL) operating at 80 kV. For sample preparation 5  $\mu$ L of DNA origami structures were deposited on glow-discharged TEM grids (formvar/carbon-coated, 300 mesh Cu; TED Pella, Inc; prod no. 01753 - f) for 1 – 4 min, depending on sample concentration. For visualization, bare origami structures were negatively stained by briefly washing the grid with 5  $\mu$ L of a 2 % uranyl formate solution followed by staining with uranyl formate for 10 s. Origami@SiO<sub>2</sub> were simply washed twice with water.

*Scanning Electron Microscopy:* As prepared TEM grids were directly used for SEM imaging after 10 s sputtering (60 % gold, 40 % palladium) using an Edwards Sputtercoater S150B 1990. Process parameters used for sputtering were 7 mbar Ar, 1.1 kV, 35 mA. The Au/Pd deposited TEM grids were fixed on the sample holder using carbon tape. SEM imaging was carried out on a Zeiss LEO DSM 982 GEMINI (containing a source of thermal field emitting (TFE) cathode (1997) and a detector of LEO High Efficiency In-Lense Secondary Electrons) with an acceleration voltage of 10 kV and an aperture of 30  $\mu$ m. Crystals@SiO<sub>2</sub> were also visualized in 60° tilt mode.

*Scanning Transmission Electron Microscopy and Energy-Dispersive X-ray Spectroscopy:* Scanning TEM and elemental mapping of origami@SiO<sub>2</sub> was performed at 120 kV using a FEI Titan Themis equipped with a SuperX EDX detector in anullar dark field (ADF) mode.

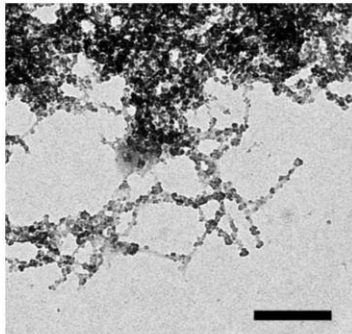


## Silica Coating Optimization



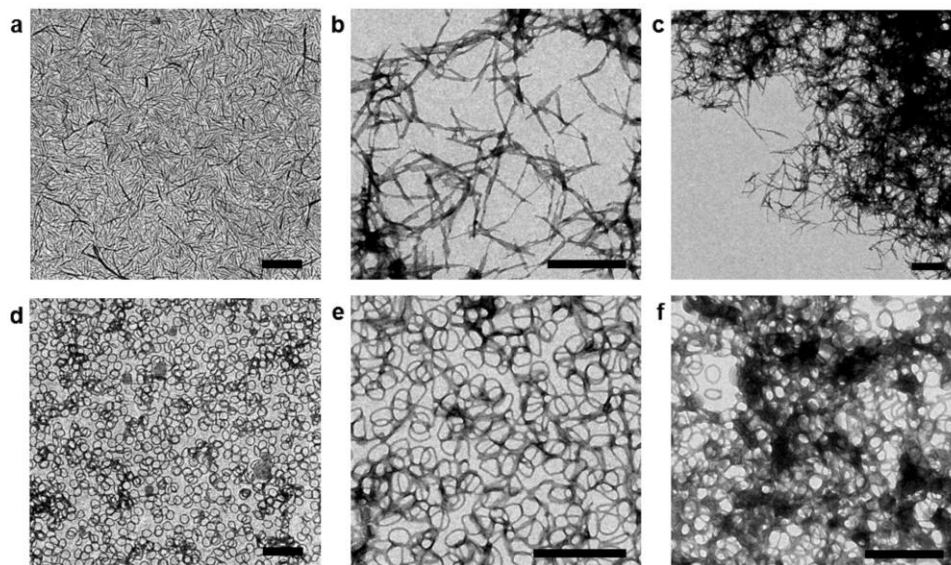
**Figure S4.** TEM micrographs of silica mineralized dsDNA under different conditions. (a) 1×TAE 11mM MgCl<sub>2</sub>, static (b) 1×TAE 11mM MgCl<sub>2</sub>, shaken (c) 1×TAE, static (d) 1×TAE, shaken (e) 11mM MgCl<sub>2</sub>, static (f) 11mM MgCl<sub>2</sub>, shaken (g) 5mM MgCl<sub>2</sub>, static (h) 5mM MgCl<sub>2</sub>, shaken (i) 1×TAE 5mM MgCl<sub>2</sub>, static (j) 200 mM NaCl, static (k) 200 mM NaCl, shaken (l) TES in water. Samples are unstained. Scale bars are 1 μm for (a), (b), (c), (j), (f), 4 μm for (d), 600 nm for (e), (g), (i), 2 μm for (h), (k) and 200 nm for (l).





**Figure S5.** TEM micrograph of 14 HB@SiO<sub>2</sub> after 14 d of silica growth in 11 mM MgCl<sub>2</sub> and at 25 °C using 50 nM origami concentration. Scale bar is 200 nm.

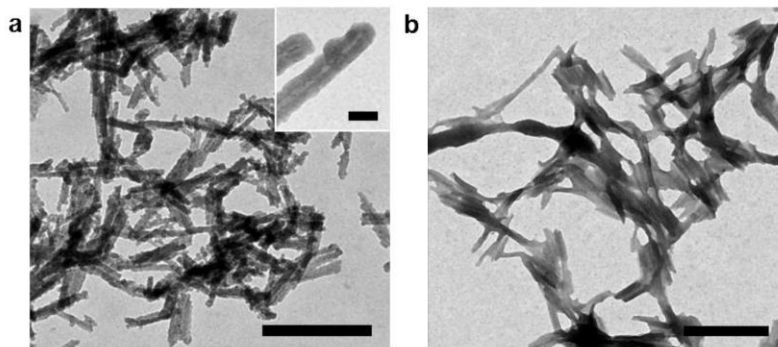
As a control experiment we studied the influence of a higher MgCl<sub>2</sub> concentration (11 mM) on the silica encapsulation of the 14 HB structure. After 14 days a grainy silica layer had grown over the structure and undefined silica clusters were obtained indicating the detrimental influence of the salt ions on the sol-gel process (**Figure S5**). Mg<sup>2+</sup> ions compete with TMAPS molecules through electrostatic interaction with the phosphate backbone of the DNA preventing coverage of the whole origami structure with TMAPS molecules. Therefore, the MgCl<sub>2</sub> concentration needs to be as low as possible (we obtained a smooth silica layer for concentrations between 0.5 mM - 3 mM) and only high enough for the origami structures to sustain their shape.

*Influence of reaction time on silica shell thickness*

**Figure S6.** TEM micrographs of 14 HB rod@SiO<sub>2</sub> after (a) 7, (b) 14, and (c) 21 d of silica growth as well as the 14 HB ring@SiO<sub>2</sub> after (d) 7, (e) 14 and (f) 21 d of silica growth. Scale bars are 500 nm for (a) (b) (c) and 300 nm for (d) (e) (f).

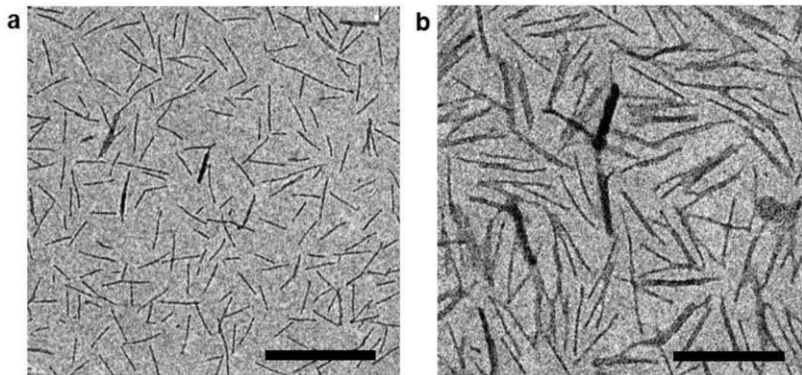
As expected the silica shell grows thicker with increasing growth time. After more than 7 days adjacent origami@SiO<sub>2</sub> structures start to coalesce to form undefined clusters (**Figure S6** (b) (c) (e) (f)). In order to stop silica growth before cluster formation starts and thus to obtain individual origami@SiO<sub>2</sub>, the structures can be isolated by centrifugation and redispersion in water.

*Influence of origami concentration on silica shell thickness*



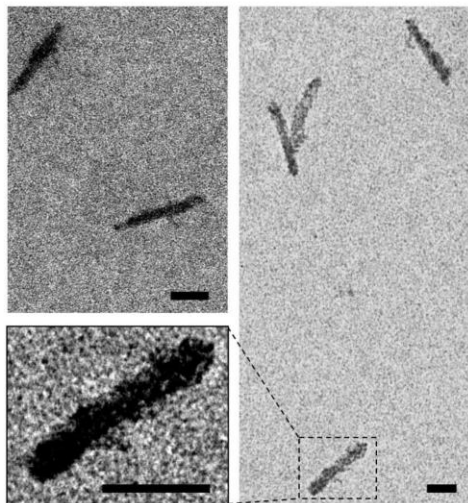
**Figure S7.** TEM micrographs of 14 HB@SiO<sub>2</sub> after 7 d of silica growth in 3 mM MgCl<sub>2</sub> and at 25 °C using (a) 50 nM and (b) 25 nM origami concentration. Scale bars are 500 nm for (a), 30 nm for the inset and 600 nm for (b).

The silica shell thickness is influenced by the origami concentration used for mineralization. The use of 50 nM origami concentration lead to a thinner silica shell after 7 days (**Figure S7 (a)**) compared to the use of 25 nM origami concentration (**Figure S7 (b)**). In both cases the thickness of the silica layer is much higher than for the 14 HB@SiO<sub>2</sub> structures where 450 nM origami concentration was used for silica encapsulation (**Figure S8 (a)**). With increasing silica shell thickness, the 14 HB@SiO<sub>2</sub> structures begin to cluster.

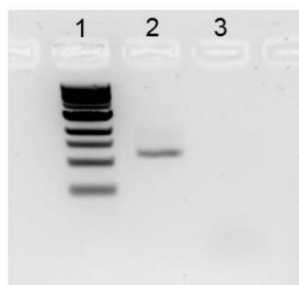
**Thermal Stability Assessment**

**Figure S8.** (a) TEM micrographs of 14 HB@SiO<sub>2</sub> after 7 d of silica growth at room temperature and in 3 mM MgCl<sub>2</sub> using 450 nM origami concentration and (c) after heating to 100 °C for 5 min. Scale bars are 500 nm for (a), 300 nm for (b).

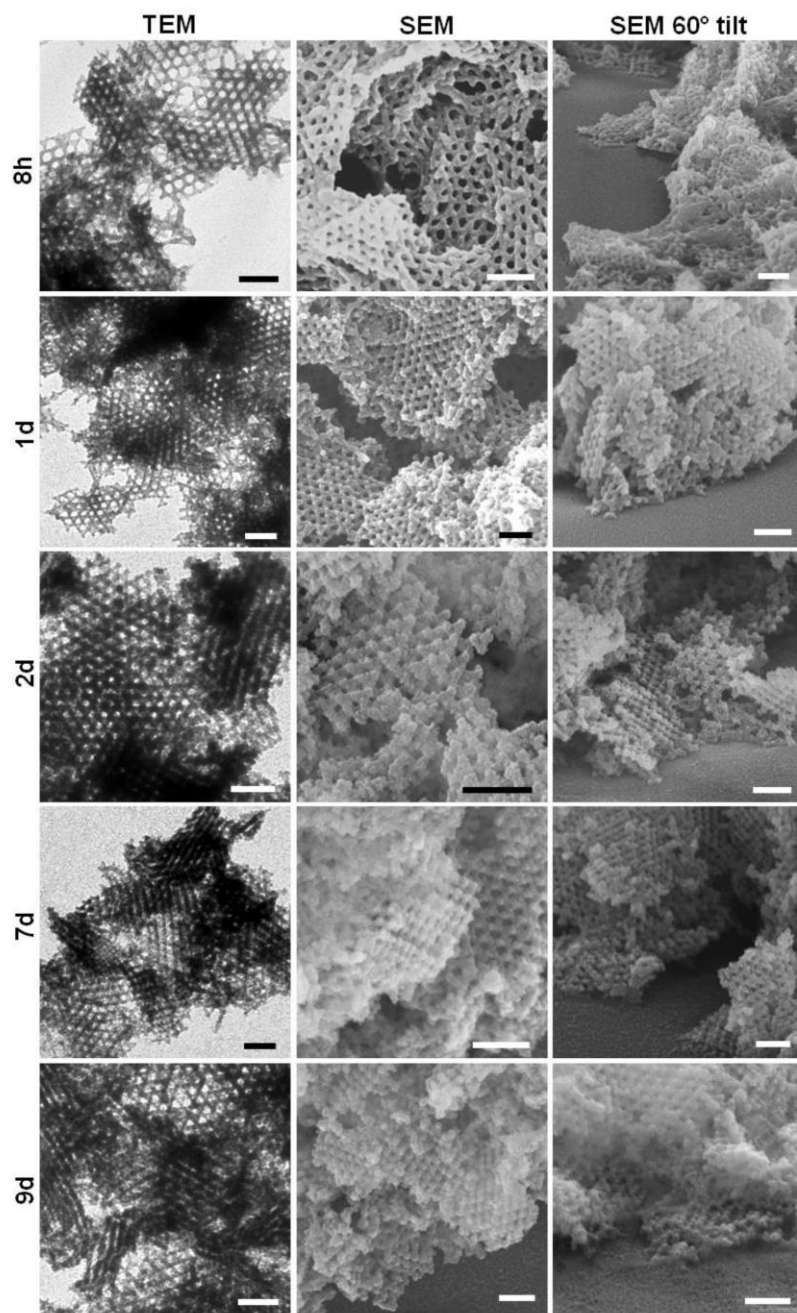
SUPPORTING INFORMATION FOR ACCEPTED ARTICLE

**Stability Assessment (against DNase digestion)**

**Figure S9.** TEM micrographs of 14 HB@SiO<sub>2</sub> (180 nM) after treatment with 1 mg/ml DNase I (dissolved in 1×DNase I buffer) for 1.5 h at room temperature. Scale bars are 100 nm.



**Figure S10:** Analysis by 1.5 % agarose gel electrophoresis. Lane 1 is 1 Kb DNA ladder, lane 2 is uncoated 14 HB rod (5 nM), lane 3 is uncoated 14 HB rod (5 nM) exposed to 1 mg/ml DNase I for 1.5 h at room temperature.



**Figure S11.** TEM and SEM (top view and 60° tilt mode) images of 3D DNA origami crystal lattices after 8 h, 1 d, 2 d, 7 d and 9 d of silica growth. Scale bars are 200 nm.

**Table S1.** Average strut diameter ( $\pm$  S.D.) and resulting shell thickness estimated from TEM image analysis.

Growth Time (d)	Avg. Strut Diameter (nm) by TEM	Avg. Shell Thickness (nm) by TEM
0	12.1 $\pm$ 1.5	0
0.33	13.5 $\pm$ 1.5	0.7
1	14.5 $\pm$ 1.6	1.2
2	15.0 $\pm$ 1.7	1.5
4	15.5 $\pm$ 2.0	1.7
7	19.4 $\pm$ 2.2	3.7
9	23.4 $\pm$ 3.6	5.7

#### References

- [1] S. M. Douglas, A. H. Marblestone, S. Teerapittayanon, A. Vazquez, G. M. Church, W. M. Shih, *Nucleic Acids Res.* **2009**, *37*, 5001-5006.
- [2] T. Zhang, C. Hartl, K. Frank, A. Heuer-Jungemann, S. Fischer, P. C. Nickels, B. Nickel, T. Liedl, *Adv. Mater.* **2018**, *30*, 6.
- [3] E. Stahl, T. G. Martin, F. Praetorius, H. Dietz, *Angew. Chem. Int. Ed.* **2014**, *53*, 12735-12740.
- [4] C. Y. Jin, H. B. Qiu, L. Han, M. H. Shu, S. A. Che, *Chem. Commun.* **2009**, 3407-3409.



## 6.2 Supporting Information for Publication 2

### Supporting Information

#### Chiral Assembly of Gold-Silver Core-Shell Plasmonic Nanorods on DNA Origami with Strong Optical Activity

*Linh Nguyen, Mihir Dass, Martina F. Ober, Lucas V. Besteiro, Zhiming M. Wang, Bert Nickel, Alexander O. Govorov, Tim Liedl, Amelie Heuer-Jungemann\**

##### Materials and Methods

All chemicals were used as received without further purification.  $\text{HAuCl}_4$ ,  $\text{NaOH}$ , L-ascorbic acid,  $\text{MgCl}_2$ , 10 % sodium dodecyl sulfate (SDS), O-(2-Mercaptoethyl)-O'-methyl-hexa(ethylene glycol) (mPEG thiol), and mercapto propionic acid (MPA) were purchased from Sigma Aldrich.  $\text{AgNO}_3$ , 5-bromosalicylic acid (5-BrSA), and cetyltrimethylammonium bromide (CTAB) were purchased from TCI America. DNA and thiol-DNA were purchased from Eurofins Genomics and Biomers.

##### Circular Dichroism Measurements

All CD measurements were performed in a Chirascan plus CD spectrometer with 10 mm pathlength quartz cuvettes. The cuvettes were cleaned with fresh aqua regia, washed thoroughly with MilliQ water and dried under  $\text{N}_2$  flow before each measurement. The baseline measurements were performed with  $1\times$  TAE buffer with 11 mM  $\text{MgCl}_2$ .

The g-factor, also known as the anisotropy factor, was calculated using

$$g = \frac{\Delta\epsilon}{\epsilon}$$

or

$$g = \frac{\text{CD (in mdeg)}}{33000 * \text{Absorbance}}$$

where  $\Delta\epsilon$  is the molar CD and  $\epsilon$  is the absorbance of the sample.<sup>1</sup> Both the CD and the absorbance were measured simultaneously by the CD spectrometer.

### Small-Angle and Wide-Angle X-Ray Scattering

**SAXS:** The SAXS data were recorded at beamline P03 at PETRA III (DESY) in Hamburg. A Pilatus 1M CMOS detector (Dectris Ltd, Switzerland) with  $981 \times 1043$  pixels with  $172 \mu\text{m}$  pixel size served as detector. Sample to detector distances (5139 mm and 2021 mm) and beam centers were calibrated with Ag behenate. Sample solutions were loaded in a quartz glass capillary with a diameter of 1.5 mm and measured with an X-ray beam energy of 12.93 keV.

**WAXS:** The WAXS data were measured at beamline P21 at PETRA III (DESY) in Hamburg. A Perkin Elmer flat panel XRD 1621 with  $2048 \times 2048$  pixels with  $200 \mu\text{m}$  served as a detector. We calibrated the sample to detector distance with lanthanum hexaboride. Sample solution was dropped and dried on a thin parylene foil and the measurement was carried out at 53.7 keV.

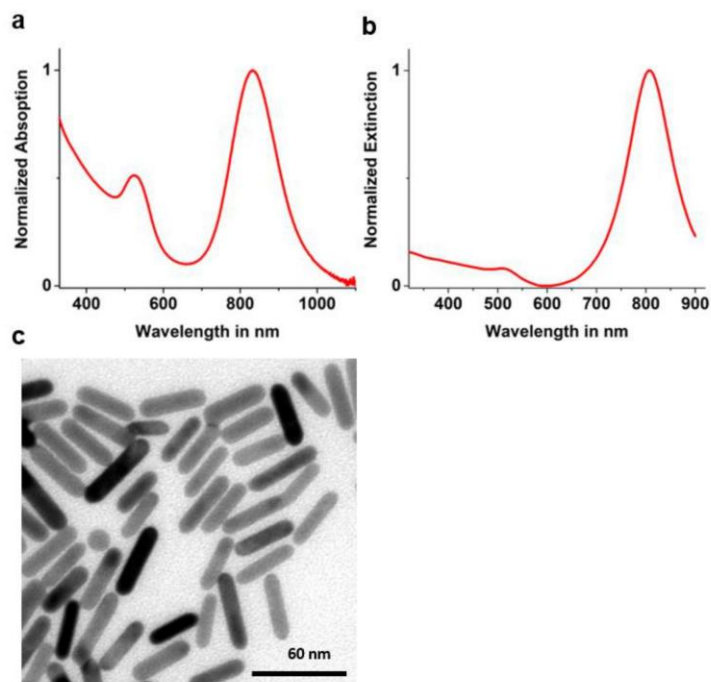
### Theoretical Models

The numerical results presented in **Figure 1b, d** and **Table S1** were obtained from full electrodynamic simulations of model nanorods, performed within an approach based on finite element methods, using COMSOL software package. The nanorods' core and shell sizes were directly taken from the experimental sample, and are listed in **Table S2**. The geometry of the models is also clearly shown in **Figure 1d**. The permittivity of gold and silver was taken from bulk values found in the literature,<sup>2</sup> and broadened by using Drude's model, as:<sup>3</sup>

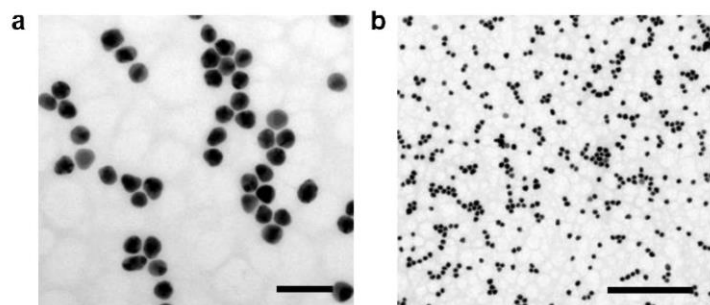
$$\varepsilon_{\text{metal}} = \varepsilon_{\text{bulk}} + \frac{\omega_p^2}{\omega(\omega + i\Gamma)} - \frac{\omega_p^2}{\omega(\omega + i3\Gamma)}$$

Where  $\omega_p$  is the plasma frequency of the material (with  $\omega_{p, \text{Au}} = 8.9 \text{ eV}$  and  $\omega_{p, \text{Ag}} = 9.3 \text{ eV}$ ), and  $\Gamma$  is its damping rate (with  $\Gamma_{\text{Au}} = 0.076 \text{ eV}$  and  $\Gamma_{\text{Ag}} = 0.02 \text{ eV}$ ). The bulk dielectric function,  $\varepsilon_{\text{bulk}}$ , was taken from the literature.<sup>2</sup> The nanorods models were studied in aqueous solution, described as a dielectric medium with permittivity  $\varepsilon_0 = 1.8$ . **Figure 1b** shows normalized results of the extinction cross section of the nanorods, *i.e.* the sum of both absorption and scattering cross sections, after averaging over six different combinations of incidence and polarization of light, in order to reproduce the response of a randomly oriented ensemble of particles in a colloidal suspension. On the other hand, **Figure 1d** presents the near field response under specific propagation and polarization conditions, specifically those exciting the transversal mode of the rods, as depicted with the arrows in the top inset. **Figure S5** presents the spectra of

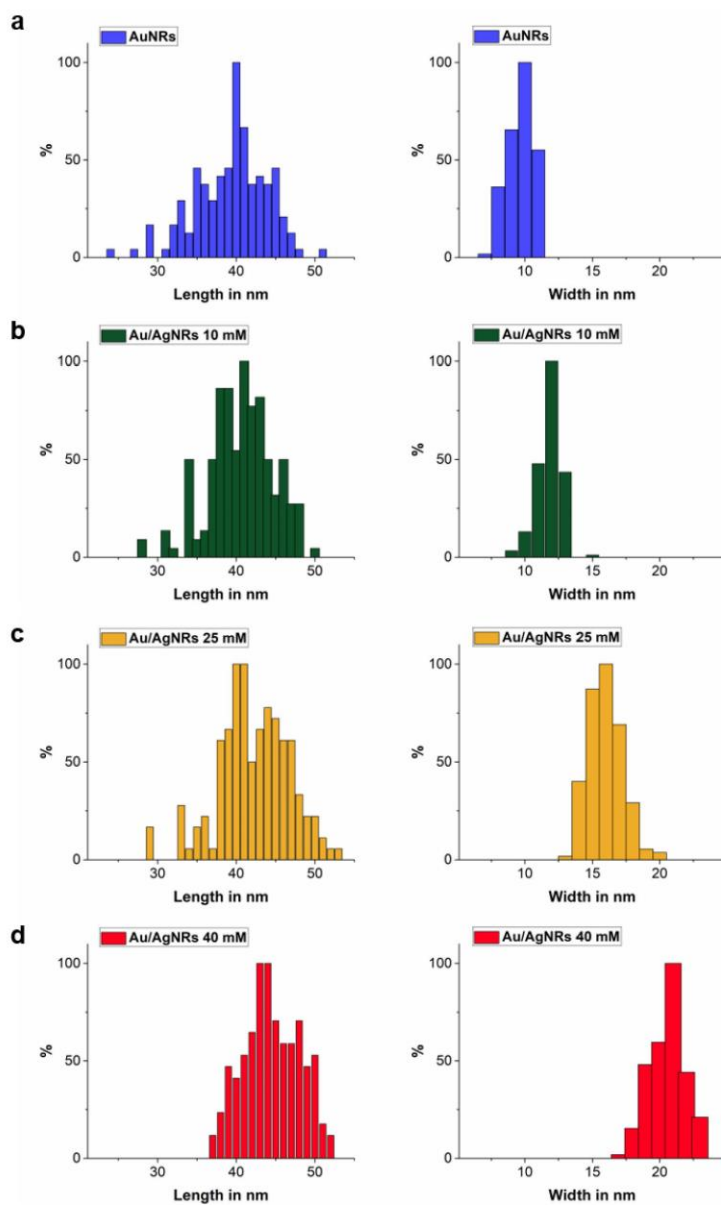
molar attenuation coefficients for the AuNRs and the largest Au/AgNRs, comparing specific polarizations with the incidence-averaged values, where it is easier to appreciate the origin of the two main plasmonic modes to the overall extinction of the particles. The figure is complemented with near field maps of these plasmonic modes.



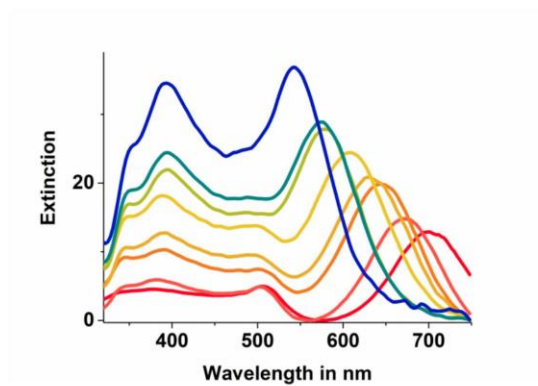
**Figure S1.** (a) Normalized absorption spectrum, (b) calculated extinction spectrum of AuNRs in water, and (c) TEM image of  $\sim 39 \times 10$  nm AuNRs.



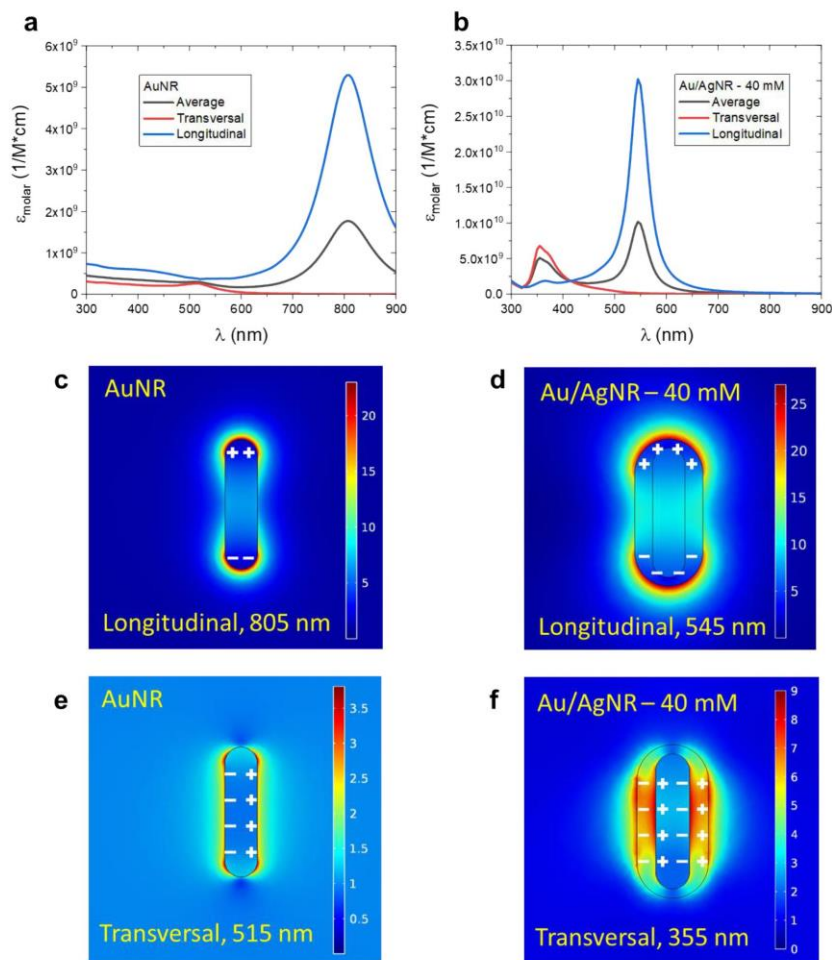
**Figure S2.** TEM micrographs of DNA-coated Au/Ag core-shell spheres. Scale bars are (a) 100 nm and (b) 600 nm.



**Figure S3.** Size distribution of Au/AgNRs@DNA synthesized using 5 nM of  $\sim 39.2 \times 9.8$  nm AuNRs and 10, 25, and 40 mM  $\text{AgNO}_3$  resulting in dimensions of  $\sim 40.4 \times 11.9$  nm,  $\sim 41.9 \times 16.0$  nm, and  $\sim 44.5 \times 20.7$  nm, respectively.



**Figure S4.** Non-normalized extinction spectra of Au/AgNRs (cf. **Fig. 1a**) with increasing Ag-shells display the enhancement in absorption efficiency of the transverse and longitudinal LSPR.

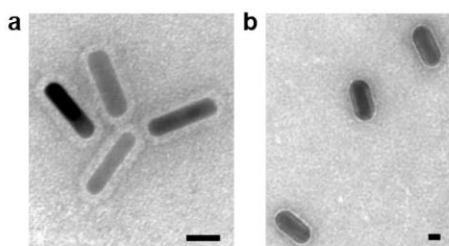
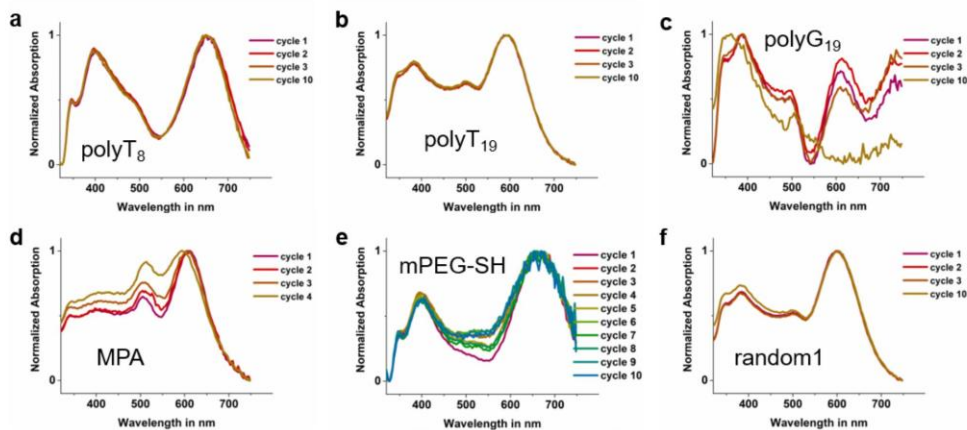


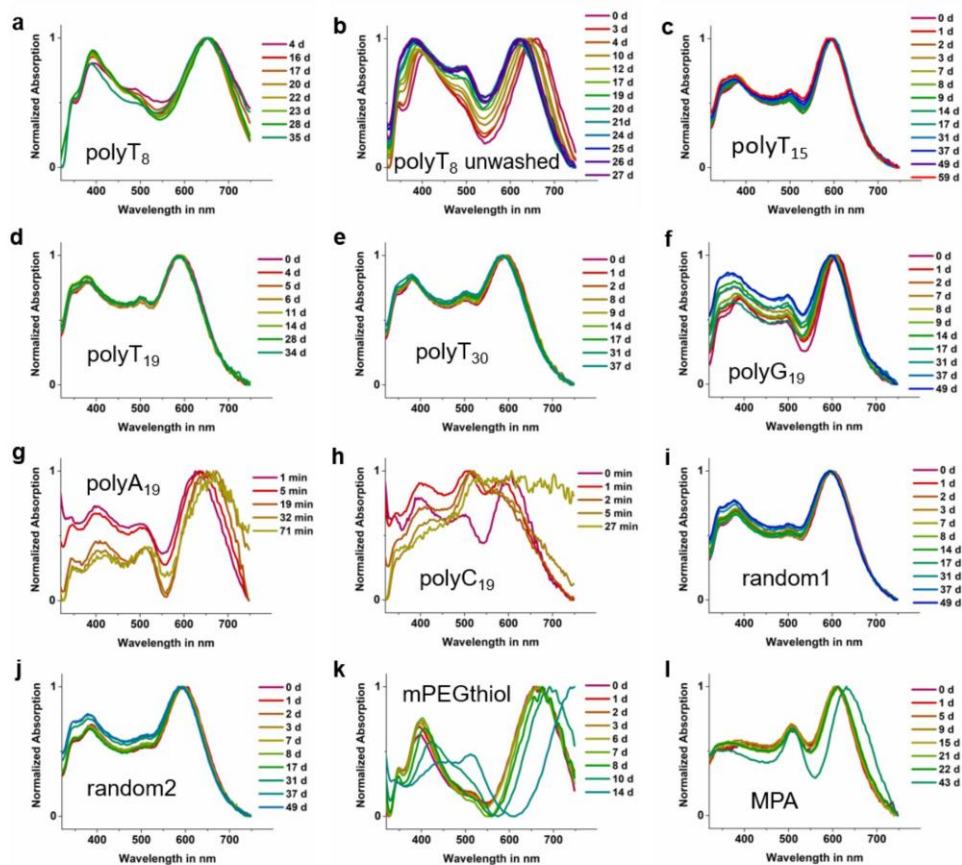
**Figure S5.** (a, b) Molar attenuation coefficient for a AuNR and the largest Au/AgNR considered in the publication. Each plot shows the profile of the two main polarizations, as well as the averaged one representing its optical response in a colloidal suspension. (c-f) Field enhancement maps for the different plasmonic modes supported by these two NRs. The data is evaluated at the maximum of  $\epsilon_{\text{molar}}$  for each polarization of incident light, taken from the first two panels.



**Table S1. Extinction coefficients.**

	Shell thickness [nm]	Experimental $\epsilon$ [ $M^{-1}\cdot cm^{-1}$ ]	Theoretical $\epsilon$ [ $M^{-1}\cdot cm^{-1}$ ]
AuNR $\sim 39.2 \times 9.8$ nm	-	-	$1.76 \cdot 10^9$
Au/AgNRs $\sim 40.4 \times 11.9$ nm	1.1	$2.671 \cdot 10^9$	$3.631 \cdot 10^9$
Au/AgNRs $\sim 41.9 \times 16.0$ nm	3.1	$5.034 \cdot 10^9$	$6.655 \cdot 10^9$
Au/AgNRs $\sim 44.5 \times 20.7$ nm	5.4	$7.603 \cdot 10^9$	$1.014 \cdot 10^{10}$

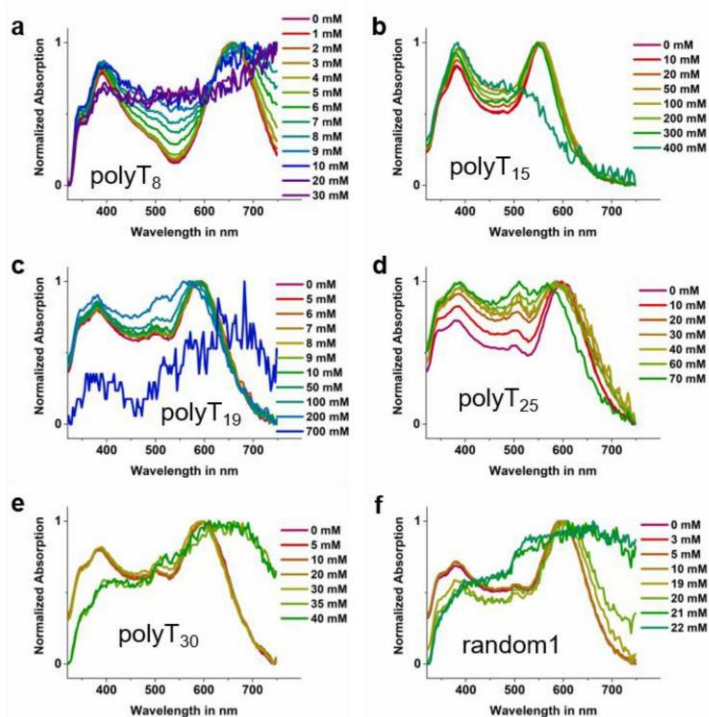
**Figure S6.** Au/AgNRs@DNA with dimensions of (a)  $\sim 37 \times 10$  nm and (b)  $\sim 59 \times 40$  nm. Scale bars are 20 nm.**Figure S7.** Absorption spectra of (a) Au/AgNRs@polyT<sub>8</sub>, (b) Au/AgNRs@polyT<sub>19</sub>, (c) Au/AgNRs@polyG<sub>19</sub>, (d) Au/AgNRs@MPA, and (e) Au/AgNRs@mPEG-thiol (f) Au/AgNRs@random1 after 10 freeze-thaw cycles.



**Figure S8.** Absorption spectra of (a) Au/AgNRs@polyT<sub>8</sub> (purified and redispersed in 1×TA buffer) (b) Au/AgNRs@polyT<sub>8</sub> (unpurified) (c) Au/AgNRs@polyT<sub>15</sub> (in 1×TA buffer) (d) Au/AgNRs@polyT<sub>19</sub> (in 1×TA buffer) (e) Au/AgNRs@polyT<sub>30</sub> (in 1×TA buffer) (f) Au/AgNRs@polyG<sub>19</sub> (in 1×TA buffer) (g) Au/AgNRs@polyA<sub>19</sub> (unpurified) (h) Au/AgNRs@polyC<sub>19</sub> (unpurified) (i) Au/AgNRs@random1 (in 1×TA buffer) (j) Au/AgNRs@random2 (in 1×TA buffer) (k) Au/AgNRs@mPEGthiol (l) Au/AgNRs@MPA (purified and redispersed in water) over time at ambient condition.

**Table S2.** DNA sequences used for functionalization of Au/Ag core-shell NRs.

Name	Sequence
T19-SH	HS-5'TTTTTTTTTTTTTTTTTTTT3'
T15-SH	HS-5'TTTTTTTTTTTTTTTTTT3'
T8-SH	HS-5'TTTTTTTTTT3'
A19-SH	HS-5'AAAAAAAAAAAAAAAAAAAAA3'
G19-SH	HS-5'GGGGGGGGGGGGGGGGGGGG3'
C19-SH	HS-5'CCCCCCCCCCCCCCCCCCCC3'
random1-SH	HS-5'TTCTCTACCACCTACAT3'
random2-SH	HS-5'TTAATCTCGCAACAGG3'

**Figure S9.** Absorption spectra of (a) Au/AgNR@polyT<sub>8</sub> (b) Au/AgNR@polyT<sub>15</sub> (c) Au/AgNR@polyT<sub>19</sub> (d) Au/AgNR@polyT<sub>25</sub> (e) Au/AgNR@polyT<sub>30</sub> and (f) Au/AgNR@random1 in increasing MgCl<sub>2</sub> concentration.

**Note S1: SAXS Data Analysis Methods**

The scattering intensity is shown as a function of scattering vector  $q = |\vec{q}| = 4\pi \sin \theta / \lambda$ , where  $\lambda$  is the wavelength of the X-rays and  $\theta$  the half of the scattering angle  $2\theta$ . The particle dimensions are obtained from model fits to the scattering intensity  $I(q)$  by running the software-internal population-based DREAM algorithm using the software package SasView (<http://www.sasview.org/>). Fit parameter values are given in **Table S3**. To analyze the scattering data of Au/Ag core-shell nanorods with DNA shell we used a simple core-shell-shell cylinder model as given in equation (1) and (2). Core-shell-shell cylinder dimensions are illustrated in **Figure 2**.

$$I(q) = \frac{\text{scale}}{V} \int_0^{\pi/2} F^2(q) \sin(\alpha) d\alpha \quad (1)$$

$$\begin{aligned} F(q) = & (\rho_c - \rho_{s1}) V_c \frac{\sin\left(q \frac{L}{2} \cos \frac{\alpha}{2}\right)}{q \frac{L}{2} \cos \frac{\alpha}{2}} \frac{2 J_1(qR \sin(\alpha))}{qR \sin(\alpha)} \quad (2) \\ & + (\rho_{s1} - \rho_{s2}) V_{s1} \frac{\sin\left(q \frac{L+d_1}{2} \cos \frac{\alpha}{2}\right)}{q \frac{L+d_1}{2} \cos \frac{\alpha}{2}} \frac{2 J_1(q(R+d_1) \sin(\alpha))}{q(R+d_1) \sin(\alpha)} \\ & + (\rho_{s2} - \rho_{solv}) V_{s2} \frac{\sin\left(q \frac{L+d_1+d_2}{2} \cos \frac{\alpha}{2}\right)}{q \frac{L+d_1+d_2}{2} \cos \frac{\alpha}{2}} \frac{2 J_1(q(R+d_1+d_2) \sin(\alpha))}{q(R+d_1+d_2) \sin(\alpha)} \end{aligned}$$

Here,  $J_1$  is the first order Bessel function,  $\alpha$  the angle between the cylinder axis and the q-vector,  $L$  the length of the cylinder core,  $R$  the radius of the cylinder core,  $d_1$  the thickness of the first shell,  $d_2$  the thickness of the second shell.  $V_{c/s1/s2}$  is the volume and  $\rho_{c/s1/s2}$  the scattering length density of the core, the first, and the second shell, respectively. To account for the polydispersity of the cylinder core radius and length we apply a Schulz distribution as given in (3) to those parameters.

$$f(x) = c (z+1)^{z+1} \left(\frac{x}{x_{mean}}\right) \frac{\exp[-(z+1)x/x_{mean}]}{x \Gamma(z+1)} \quad (3)$$

Here,  $c$  is a normalization constant,  $x_{mean}$  the mean value of the distribution, and  $z$  is a measure of the distribution's width such that the polydispersity is given by  $PD = \sigma/x_{mean}$  with  $\sigma$  corresponding to the root-mean-square deviation from  $x_{mean}$ .

Detailed fit parameter:

$$sld_{Au} = 119 * 10^{-6} / \text{\AA}^2 \text{ (fixed)}$$

$$sld_{Ag} = 77 * 10^{-6} / \text{\AA}^2 \text{ (fixed)}$$

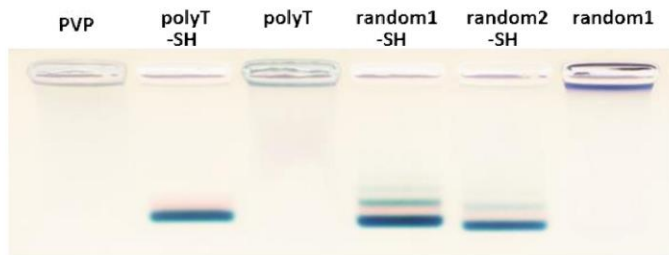
$$sld_{buffer} = 9.4 * 10^{-6} / \text{\AA}^2 \text{ (fixed)}$$

$$\chi_{red}^2 = 1.33$$

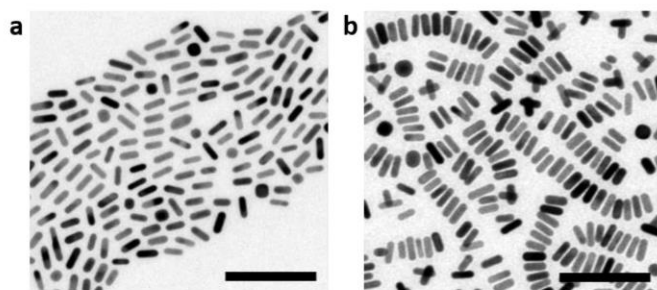
**Table S3.** Parameters obtained from fitting of SAXS data of Au/Ag core-shell nanorods with DNA shell to a cylindrical core-shell-shell model. Errors indicate the purely statistical parameter uncertainties corresponding to a two-sigma confidence interval.

Fit parameter (unit)	value
$sld_{DNA}(10^{-6} / \text{\AA}^2)$	$12.0 \pm 0.2$
$R_{Au}(\text{\AA})$	$33.8 \pm 0.2$
$d_{Ag}(\text{\AA})$	$5.5 \pm 0.2$
$d_{DNA}(\text{\AA})$	$28.7 \pm 0.3$
$L_{Au}(\text{\AA})$	$155 \pm 5$
$PD(R_{Au})$	$0.12 \pm 0.003$
$PD(L_{Au})$	$0.29 \pm 0.05$





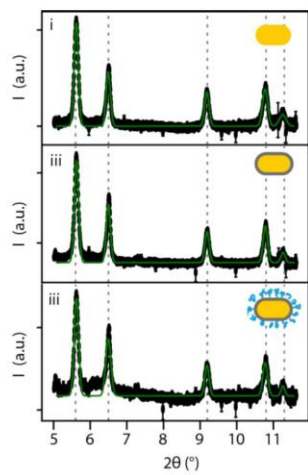
**Figure S10.** 1.5 % agarose gel electrophoresis ( $1\times$ TA buffer) of Au/AgNRs using different DNA sequences (**Table S2**) (unmodified and thiol-modified denoted -SH) for stabilization compared to PVP. Only Au/AgNRs with thiolated DNA show electrophoretic mobility. The appearance of multiple bands is attributed to the formation of Au/AgNR multimers as the random DNA sequence is partially complementary to itself. The faint red band visible in the gel results from Ag-coated Au nanospheres, which are a common by-product in the synthesis of AuNRs.



**Figure S11.** TEM micrographs of (a) AuNRs and (b) Au/AgNRs@polyT<sub>19</sub> used for SAXS measurements. Scale bars are 100 nm.

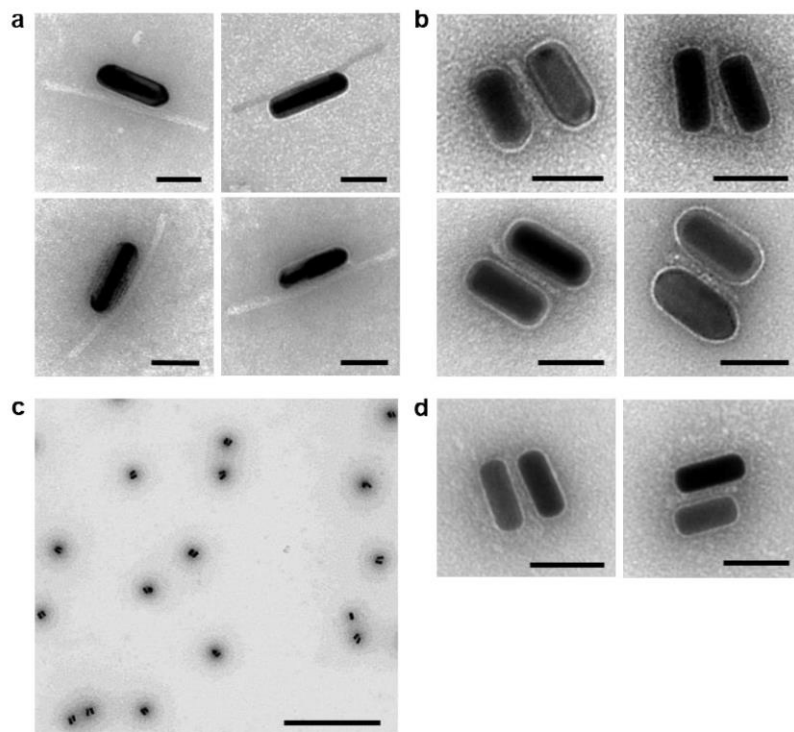
#### Note S2: WAXS Data Analysis

The recorded powder rings were transformed to  $2\theta$  angles *via* radial integration with the *Igor Pro* software plugin *Nika*.<sup>4</sup> To analyze the lattice constant of Au/Ag core-shell nanorods the diffraction signal was fitted by a sum of Gaussian peaks. The lattice spacing  $d$  was calculated from the peak position  $2\theta_c$ , following the relation  $d = 2\pi n/q_c$ , where  $n$  is the diffraction order.



**Figure S12.** WAXS data for different particle compositions. Wide-angle X-ray scattering (WAXS) intensities of AuNRs (i), Au/AgNRs (ii), and Au/AgNRs@DNA (iii). Vertical dashed lines label selected Bragg peaks found at the same position for all WAXS patterns.





**Figure S13.** TEM micrographs of: (a) Au/AgNR conjugated with a 14 HB origami; (b) Dimers of Au/AgNRs self-assembled on a 44 HB origami sheet; (c) Low magnification image of the sample shown in b; (d) AuNRs self-assembled on a 44 HB origami sheet (cf. b and c). Scale bars for a, b and d are 50 nm, scale bar for c is 1  $\mu\text{m}$ .

#### References

1. Berova, N.; Di Bari, L.; Pescitelli, G., Application of Electronic Circular Dichroism in Configurational and Conformational Analysis of Organic Compounds. *Chem. Soc. Rev.* **2007**, *36*, 914-931.
2. Johnson, P. B.; Christy, R. W., Optical Constants of the Noble Metals. *Phys. Rev. B* **1972**, *6*, 4370.
3. Kuzyk, A.; Schreiber, R.; Zhang, H.; Govorov, A. O.; Liedl, T.; Liu, N., Reconfigurable 3D Plasmonic Metamolecules. *Nat. Mater.* **2014**, *13*, 862-866.
4. Ilavsky, J., Nika: Software for Two-Dimensional Data Reduction. *J. Appl. Crystallogr.* **2012**, *45*, 324-328.

## 7 Bibliography

- [1] M. Shimomura, T. Sawadaishi, "Bottom-Up Strategy of Materials Fabrication: A New Trend in Nanotechnology of Soft Materials", *Current Opinion in Colloid and Interface Science*, **2001**.
- [2] P. W. K. Rothemund, "Folding DNA to create nanoscale shapes and patterns", *Nature*, **2006**.
- [3] <https://capsidconstructors.github.io/lab-book/dna-origami.html>, **2022**.
- [4] S. A. Amin, M. S. Parker, E. V. Armbrust, "Interactions between Diatoms and Bacteria", *Microbiology and Molecular Biology Reviews*, **2012**.
- [5] S. Mann, *Biomimetic Materials Chemistry*, John Wiley & Sons, **1996**.
- [6] K. J. Van Bommel, A. Friggeri, S. Shinkai, "Organic Templates for the Generation of Inorganic Materials", *Angewandte Chemie*, **2003**.
- [7] X. Liu, F. Zhang, X. Jing, M. Pan, P. Liu, W. Li, B. Zhu, J. Li, H. Chen, L. Wang, J. Lin, Y. Liu, D. Zhao, H. Yan, C. Fan, "Complex Silica Composite Nanomaterials Templated With DNA Origami", *Nature*, **2018**.
- [8] L. Nguyen, M. Döblinger, T. Liedl, A. Heuer-Jungemann, "DNA-Origami-Templated Silica Growth by Sol–Gel Chemistry", *Angewandte Chemie*, **2018**.
- [9] L. Qiu, H. Liu, J. Jiang, W. Tan, "DNA-Nanostructure-Templated Precise Biomineralization", *National Science Review*, **2018**.
- [10] X. Jing, F. Zhang, M. Pan, X. Dai, J. Li, L. Wang, X. Liu, H. Yan, C. Fan, "Solidifying Framework Nucleic Acids With Silica", *Nature Protocols*, **2019**.
- [11] F. Kim, T. Chen, T. Burgess, P. Rasie, T. L. Selinger, A. Greschner, G. Rizis, K. Carneiro, "Functionalized DNA Nanostructures as Scaffolds for Guided Mineralization", *Chemical Science*, **2019**.
- [12] J. Schlaferman, A. Paige, K. Meserve, J. A. Miech, A. E. Gerdon, "Selected DNA Aptamers Influence Kinetics and Morphology in Calcium Phosphate Mineralization", *ACS Biomaterials Science & Engineering*, **2019**.
- [13] X. Liu, X. Jing, P. Liu, M. Pan, Z. Liu, X. Dai, J. Lin, Q. Li, F. Wang, S. Yang, L. Wang, C. Fan, "DNA Framework-Encoded Mineralization of Calcium Phosphate", *Chem*, **2020**.

- [14] M.-K. Nguyen, V. H. Nguyen, A. K. Natarajan, Y. Huang, J. Ryssy, B. Shen, A. Kuzyk, "Ultrathin Silica Coating of DNA Origami Nanostructures", *Chemistry of Materials*, **2020**.
- [15] D. Athanasiadou, K. M. M. Carneiro, "DNA Nanostructures as Templates for Biomineralization", *Nature Reviews Chemistry*, **2021**.
- [16] P. W. Majewski, A. Michelson, M. A. L. Cordeiro, C. Tian, C. Ma, K. Kisslinger, Y. Tian, W. Liu, E. A. Stach, K. G. Yager, O. Gang, "Resilient Three-Dimensional Ordered Architectures Assembled From Nanoparticles by DNA", *Science advances*, **2021**.
- [17] S. Wu, M. Zhang, J. Song, S. Weber, X. Liu, C. Fan, Y. Wu, "Fine Customization of Calcium Phosphate Nanostructures with Site-Specific Modification by DNA Templated Mineralization", *ACS Nano*, **2021**.
- [18] A. Michelson, H. Zhang, S. Xiang, O. Gang, "Engineered Silicon Carbide Three-Dimensional Frameworks through DNA-Prescribed Assembly", *Nano Letters*, **2021**.
- [19] Y. Wang, L. Dai, Z. Ding, M. Ji, J. Liu, H. Xing, X. Liu, Y. Ke, C. Fan, P. Wang, Y. Tian, "DNA Origami Single Crystals With Wulff Shapes", *Nature Communications*, **2021**.
- [20] F. Zhou, W. Sun, C. Zhang, J. Shen, P. Yin, H. Liu, "3D Freestanding DNA Nanostructure Hybrid As a Low-Density High-Strength Material", *ACS Nano*, **2020**.
- [21] L. Shani, A. N. Michelson, B. Minevich, Y. Flegler, M. Stern, A. Shaulov, Y. Yeshurun, O. Gang, "DNA-Assembled Superconducting 3D Nanoscale Architectures", *Nature Communications*, **2020**.
- [22] Y. Shang, N. Li, S. Liu, L. Wang, Z. G. Wang, Z. Zhang, B. Ding, "Site-Specific Synthesis of Silica Nanostructures on DNA Origami Templates", *Advanced Materials*, **2020**.
- [23] L. Liu, M. Zheng, Z. Li, Q. Li, C. Mao, "Patterning Nanoparticles With DNA Molds", *ACS Applied Materials and Interfaces*, **2019**.
- [24] A. Heuer-Jungemann, V. Linko, "Engineering Inorganic Materials With DNA Nanostructures", *ACS Central Science*, **2021**.
- [25] D. L. Fedlheim, C. A. Foss, *Metal Nanoparticles: Synthesis, Characterization, And Applications*, CRC press, **2001**.

- [26] S. Bayda, M. Adeel, T. Tuccinardi, M. Cordani, F. Rizzolio, "The History of Nanoscience and Nanotechnology: From Chemical–Physical Applications to Nanomedicine", *Molecules*, **2020**.
- [27] P. Slepíčka, N. Slepíčková Kasálková, J. Siegel, Z. Kolská, V. Švorčík, "Methods of Gold and Silver Nanoparticles Preparation", *Materials*, **2019**.
- [28] E. Calucho, C. Parolo, L. Rivas, R. Álvarez-Diduk, A. Merkoçi, in *Comprehensive Analytical Chemistry, Vol. 89* (Ed.: A. Merkoçi), Elsevier, **2020**, pp. 313-359.
- [29] J. Turkevich, P. C. Stevenson, J. Hillier, "A Study of the Nucleation and Growth Processes in the Synthesis of Colloidal Gold", *Discussions of the Faraday Society*, **1951**.
- [30] M. Brust, M. Walker, D. Bethell, D. J. Schiffrin, R. Whyman, "Synthesis of Thiol-Derivatized Gold Nanoparticles in a Two-Phase Liquid–Liquid System", *Chemical Communications*, **1994**.
- [31] N. R. Jana, L. Gearheart, C. J. Murphy, "Seeding Growth for Size Control of 5–40 nm Diameter Gold Nanoparticles", *Langmuir*, **2001**.
- [32] X. Hu, Y. Zhang, T. Ding, J. Liu, H. Zhao, "Multifunctional Gold Nanoparticles: A Novel Nanomaterial for Various Medical Applications and Biological Activities", *Frontiers in Bioengineering and Biotechnology*, **2020**.
- [33] C. A. Mirkin, R. L. Letsinger, R. C. Mucic, J. J. Storhoff, "A DNA-Based Method for Rationally Assembling Nanoparticles Into Macroscopic Materials", *Nature*, **1996**.
- [34] A. P. Alivisatos, K. P. Johnsson, X. Peng, T. E. Wilson, C. J. Loweth, M. P. Bruchez, P. G. Schultz, "Organization of 'Nanocrystal Molecules' Using DNA", *Nature*, **1996**.
- [35] F. A. Aldaye, H. F. Sleiman, "Sequential Self-Assembly of a DNA Hexagon as a Template for the Organization of Gold Nanoparticles", *Angewandte Chemie*, **2006**.
- [36] B. Ding, Z. Deng, H. Yan, S. Cabrini, R. N. Zuckermann, J. Bokor, "Gold Nanoparticle Self-Similar Chain Structure Organized by DNA Origami", *Journal of the American Chemical Society*, **2010**.
- [37] Z. Fan, A. O. Govorov, "Plasmonic Circular Dichroism of Chiral Metal Nanoparticle Assemblies", *Nano Letters*, **2010**.
- [38] A. Kuzyk, R. Schreiber, Z. Fan, G. Pardatscher, E.-M. Roller, A. Högele, F. C. Simmel, A. O. Govorov, T. Liedl, "DNA-Based Self-Assembly of Chiral Plasmonic Nanostructures With Tailored Optical Response", *Nature*, **2012**.

- [39] R. R. Arvizo, S. Bhattacharyya, R. A. Kudgus, K. Giri, R. Bhattacharya, P. Mukherjee, "Intrinsic Therapeutic Applications of Noble Metal Nanoparticles: Past, Present and Future", *Chemical Society Reviews*, **2012**.
- [40] D. Thompson, "Michael Faraday's Recognition of Ruby Gold: The Birth of Modern Nanotechnology", *Gold Bulletin*, **2007**.
- [41] <https://www.nobelprize.org/prizes/chemistry/1925/zsigmondy/facts/>, **2022**.
- [42] V. K. LaMer, R. H. Dinegar, "Theory, Production and Mechanism of Formation of Monodispersed Hydrosols", *Journal of the American Chemical Society*, **1950**.
- [43] D. Pines, D. Bohm, "A Collective Description of Electron Interactions: II. Collective vs Individual Particle Aspects of the Interactions", *Physical Review*, **1952**.
- [44] R. H. Ritchie, "Plasma Losses by Fast Electrons in Thin Films", **1957**.
- [45] N. R. Jana, L. Gearheart, C. J. Murphy, "Wet Chemical Synthesis of High Aspect Ratio Cylindrical Gold Nanorods", *The Journal of Physical Chemistry B*, **2001**.
- [46] E. Prodan, C. Radloff, N. J. Halas, P. Nordlander, "A Hybridization Model for the Plasmon Response of Complex Nanostructures", *Science*, **2003**.
- [47] C. J. Murphy, T. K. Sau, A. M. Gole, C. J. Orendorff, J. Gao, L. Gou, S. E. Hunyadi, T. Li, "Anisotropic Metal Nanoparticles: Synthesis, Assembly, and Optical Applications", *The Journal of Physical Chemistry B*, **2005**.
- [48] J. Pérez-Juste, I. Pastoriza-Santos, L. M. Liz-Marzán, P. Mulvaney, "Gold Nanorods: Synthesis, Characterization and Applications", *Coordination Chemistry Reviews*, **2005**.
- [49] J. Sharma, R. Chhabra, Y. Liu, Y. Ke, H. Yan, "DNA-Templated Self-Assembly of Two-Dimensional and Periodical Gold Nanoparticle Arrays", *Angewandte Chemie*, **2006**.
- [50] J. Zheng, P. E. Constantinou, C. Micheel, A. P. Alivisatos, R. A. Kiehl, N. C. Seeman, "Two-Dimensional Nanoparticle Arrays Show the Organizational Power of Robust DNA Motifs", *Nano Letters*, **2006**.
- [51] S. Y. Park, A. K. Lytton-Jean, B. Lee, S. Weigand, G. C. Schatz, C. A. Mirkin, "DNA-Programmable Nanoparticle Crystallization", *Nature*, **2008**.
- [52] D. Nykypanchuk, M. M. Maye, D. van der Lelie, O. Gang, "DNA-Guided Crystallization of Colloidal Nanoparticles", *Nature*, **2008**.

- [53] A. Kuzyk, R. Schreiber, Z. Fan, G. Pardatscher, E.-M. Roller, A. Högele, F. C. Simmel, A. O. Govorov, T. Liedl, "DNA-Based Self-Assembly of Chiral Plasmonic Nanostructures with Tailored Optical Response", *Nature*, **2012**.
- [54] G. A. Posthuma-Trumpie, J. Korf, A. van Amerongen, "Lateral Flow (Immuno)Assay: Its Strengths, Weaknesses, Opportunities and Threats. A Literature Survey", *Analytical and Bioanalytical Chemistry*, **2009**.
- [55] Y. Liu, L. Zhan, Z. Qin, J. Sackrison, J. C. Bischof, "Ultrasensitive and Highly Specific Lateral Flow Assays for Point-of-Care Diagnosis", *ACS Nano*, **2021**.
- [56] A. H. Free, E. C. Adams, M. L. Kercher, H. M. Free, M. H. Cook, "Simple Specific Test for Urine Glucose", *Clinical Chemistry*, **1957**.
- [57] H. M. Free, G. F. Collins, A. H. Free, "Triple-Test Strip for Urinary Glucose, Protein, and pH", *Clinical Chemistry*, **1960**.
- [58] S. Rosen, in *Lateral Flow Immunoassay*, Springer, **2009**, pp. 1-15.
- [59] K. M. Koczula, A. Gallotta, "Lateral Flow Assays", *Essays Biochem*, **2016**.
- [60] F. Di Nardo, M. Chiarello, S. Cavalera, C. Baggiani, L. Anfossi, "Ten Years of Lateral Flow Immunoassay Technique Applications: Trends, Challenges and Future Perspectives", *Sensors*, **2021**.
- [61] C. Danks, I. Barker, "On-Site Detection of Plant Pathogens Using Lateral-Flow Devices", *EPPO Bulletin*, **2000**.
- [62] C. L. Mthembu, M. I. Sabela, M. Mlambo, L. M. Madikizela, S. Kanchi, H. Gumede, P. S. Mdluli, "Google Analytics and Quick Response for Advancement of Gold Nanoparticle-Based Dual Lateral Flow Immunoassay for Malaria–Plasmodium Lactate Dehydrogenase (pLDH)", *Analytical Methods*, **2017**.
- [63] S. L. Emery, D. D. Erdman, M. D. Bowen, B. R. Newton, J. M. Winchell, R. F. Meyer, S. Tong, B. T. Cook, B. P. Holloway, K. A. McCaustland, P. A. Rota, B. Bankamp, L. E. Lowe, T. G. Ksiazek, W. J. Bellini, L. J. Anderson, "Real-Time Reverse Transcription-Polymerase Chain Reaction Assay for SARS-Associated Coronavirus", *Emerg Infect Dis*, **2004**.
- [64] J. E. Butler, "Enzyme-Linked Immunosorbent Assay", *Journal of Immunoassay*, **2000**.
- [65] S. Sharma, J. Zapatero-Rodríguez, P. Estrela, R. O'Kennedy, "Point-of-Care Diagnostics in Low Resource Settings: Present Status and Future Role of Microfluidics", *Biosensors*, **2015**.

- [66] F. Mahmoudinobar, D. Britton, J. K. Montclare, "Protein-Based Lateral Flow Assays for COVID-19 Detection", *Protein Engineering, Design and Selection*, **2021**.
- [67] W. C. Mak, V. Beni, A. P. Turner, "Lateral-Flow Technology: From Visual to Instrumental", *Trends in Analytical Chemistry*, **2016**.
- [68] J. Li, J. Macdonald, "Lateral flow immunoassays—how fundamental breakthroughs from the 1950s led to the inception of this simple yet powerful tool", *Australian Biochemist*, **2016**.
- [69] P. Porter, J. Coley, M. Gani, "Immunochemical criteria for successful matching of monoclonal antibodies to immunoassays of peptide hormones for assessment of pregnancy and ovulation", *Progress in clinical and biological research*, **1988**.
- [70] S. A. Leavitt, "'A Private Little Revolution': The Home Pregnancy Test in American Culture", *Bulletin of the History of Medicine*, **2006**.
- [71] A. Sena-Torralba, D. B. Ngo, C. Parolo, L. Hu, R. Álvarez-Diduk, J. F. Bergua, G. Rosati, W. Surareungchai, A. Merkoçi, "Lateral Flow Assay Modified With Time-Delay Wax Barriers as a Sensitivity and Signal Enhancement Strategy", *Biosensors and Bioelectronics*, **2020**.
- [72] V.-T. Nguyen, S. Song, S. Park, C. Joo, "Recent Advances in High-Sensitivity Detection Methods for Paper-Based Lateral-Flow Assay", *Biosensors and Bioelectronics*, **2020**.
- [73] J. D. Bishop, H. V. Hsieh, D. J. Gasperino, B. H. Weigl, "Sensitivity Enhancement in Lateral Flow Assays: A Systems Perspective", *Lab on a Chip*, **2019**.
- [74] P. R. West, S. Ishii, G. V. Naik, N. K. Emani, V. M. Shalaev, A. Boltasseva, "Searching for Better Plasmonic Materials", *Laser Photonics Reviews*, **2010**.
- [75] P. W. Rothmund, "Folding DNA to Create Nanoscale Shapes and Patterns", *Nature Communications*, **2006**.
- [76] W. Stöber, A. Fink, E. Bohn, "Controlled Growth of Monodisperse Silica Spheres in the Micron Size Range", *Journal of Colloid and Interface Science*, **1968**.
- [77] G. Ertl, H. Knözinger, J. Weitkamp, *Handbook of Heterogeneous Catalysis, Vol. 2*, Citeseer, **1997**.
- [78] L. Valot, M. Maumus, T. Montheil, J. Martinez, D. Noël, A. Mehdi, G. Subra, "Biocompatible Glycine-Assisted Catalysis of the Sol-Gel Process: Development of Cell-Embedded Hydrogels", *ChemPlusChem*, **2019**.



- [79] C. J. Brinker, G. W. Scherer, *Sol-Gel Science: The Physics and Chemistry of Sol-Gel Processing*, Academic press, **2013**.
- [80] S. Che, A. E. Garcia-Bennett, T. Yokoi, K. Sakamoto, H. Kunieda, O. Terasaki, T. Tatsumi, "A Novel Anionic Surfactant Templating Route for Synthesizing Mesoporous Silica With Unique Structure", *Nature Materials*, **2003**.
- [81] P. K. Jain, S. Eustis, M. A. El-Sayed, "Plasmon coupling in nanorod assemblies: optical absorption, discrete dipole approximation simulation, and exciton-coupling model", *The Journal of Physical Chemistry B*, **2006**.
- [82] P. Nordlander, C. Oubre, E. Prodan, K. Li, M. Stockman, "Plasmon Hybridization in Nanoparticle Dimers", *Nano Letters*, **2004**.
- [83] H. Chen, L. Shao, Q. Li, J. Wang, "Gold Nanorods and Their Plasmonic Properties", *Chemical Society Reviews*, **2013**.
- [84] Z. Qriouet, Y. Cherrah, H. Sefrioui, Z. Qmichou, "Monoclonal Antibodies Application in Lateral Flow Immunochromatographic Assays for Drugs of Abuse Detection", *Molecules*, **2021**.
- [85] K. Wang, W. Qin, Y. Hou, K. Xiao, W. Yan, "The Application of Lateral Flow Immunoassay in Point of Care Testing: A Review", *Nano Biomed. Eng*, **2016**.
- [86] U. Hoff, O. Dirksen, V. Dirksen, G. Kuhn, H. Meyer, B. Diekmann, "Holocene Freshwater Diatoms: Palaeoenvironmental Implications From South Kamchatka, Russia ", *Boreas*, **2014**.
- [87] S. Mann, "Self-Assembly and Transformation of Hybrid Nano-Objects and Nanostructures Under Equilibrium and Non-Equilibrium Conditions", *Nature Materials*, **2009**.
- [88] C. J. Brinker, Y. Lu, A. Sellinger, H. Fan, "Evaporation-Induced Self-Assembly: Nanostructures Made Easy", *Advanced Materials*, **1999**.
- [89] S. Che, Z. Liu, T. Ohsuna, K. Sakamoto, O. Terasaki, T. Tatsumi, "Synthesis and Characterization of Chiral Mesoporous Silica", *Nature*, **2004**.
- [90] B. Liu, Y. Cao, Z. Huang, Y. Duan, S. Che, "Silica Biomineralization via the Self-Assembly of Helical Biomolecules", *Advanced Materials*, **2015**.
- [91] A. Kristensen, J. K. W. Yang, S. I. Bozhevolnyi, S. Link, P. Nordlander, N. J. Halas, N. A. Mortensen, "Plasmonic Colour Generation", *Nature Reviews Materials*, **2016**.
- [92] S. Hayashi, T. Okamoto, "Plasmonics: Visit the Past to Know the Future", *Journal of Physics D: Applied Physics*, **2012**.

- [93] C. Noguez, "Surface Plasmons on Metal Nanoparticles: The Influence of Shape and Physical Environment", *The Journal of Physical Chemistry C*, **2007**.
- [94] L. Pauling, "THE NATURE OF THE CHEMICAL BOND. APPLICATION OF RESULTS OBTAINED FROM THE QUANTUM MECHANICS AND FROM A THEORY OF PARAMAGNETIC SUSCEPTIBILITY TO THE STRUCTURE OF MOLECULES", *Journal of the American Chemical Society*, **1931**.
- [95] K. Martens, F. Binkowski, L. Nguyen, L. Hu, A. O. Govorov, S. Burger, T. Liedl, "Long- and Short-Ranged Chiral Interactions in DNA-Assembled Plasmonic Chains", *Nature Communications*, **2021**.
- [96] M. J. Urban, C. Shen, X.-T. Kong, C. Zhu, A. O. Govorov, Q. Wang, M. Hentschel, N. Liu, "Chiral Plasmonic Nanostructures Enabled by Bottom-Up Approaches", *Annual Review of Physical Chemistry*, **2019**.
- [97] W. A. Paiva-Marques, F. Reyes Gómez, O. N. Oliveira, Jr., J. R. Mejía-Salazar, "Chiral Plasmonics and Their Potential for Point-of-Care Biosensing Applications", *Sensors (Basel)*, **2020**.
- [98] O. Gang, J. J. A. C. Kahn, "Designer Nanomaterials through Programmable Assembly", **2021**.
- [99] C. R. Jacobson, D. Solti, D. Renard, L. Yuan, M. Lou, N. J. Halas, "Shining Light on Aluminum Nanoparticle Synthesis", *Accounts of Chemical Research*, **2020**.
- [100] N. Dmitruk, A. Korovin, "Physical Nature of Anomalous Optical Transmission of Thin Absorptive Corrugated Films", *JETP Letters*, **2009**.
- [101] A. S. Baburin, A. M. Merzlikin, A. V. Baryshev, I. A. Ryzhikov, Y. V. Panfilov, I. A. Rodionov, "Silver-Based Plasmonics: Golden Material Platform and Application Challenges", *Optical Materials Express*, **2019**.
- [102] M. Rycenga, C. M. Cobley, J. Zeng, W. Li, C. H. Moran, Q. Zhang, D. Qin, Y. Xia, "Controlling the Synthesis and Assembly of Silver Nanostructures for Plasmonic Applications", *Chemical reviews*, **2011**.
- [103] G. Saleh, C. Xu, S. Sanvito, "Silver Tarnishing Mechanism Revealed by Molecular Dynamics Simulations", *Angewandte Chemie*, **2019**.
- [104] J. D. Padmos, P. Zhang, "Surface Structure of Organosulfur Stabilized Silver Nanoparticles Studied With X-Ray Absorption Spectroscopy", *The Journal of Physical Chemistry C*, **2012**.

- [105] L. Nguyen, M. Dass, M. F. Ober, L. V. Besteiro, Z. M. Wang, B. Nickel, A. O. Govorov, T. Liedl, A. Heuer-Jungemann, "Chiral Assembly of Gold–Silver Core–Shell Plasmonic Nanorods on DNA Origami with Strong Optical Activity", *ACS Nano*, **2020**.
- [106] B. Auguie, J. L. Alonso-Gómez, A. Guerrero-Martínez, L. M. Liz-Marzán, "Fingers Crossed: Optical Activity of a Chiral Dimer of Plasmonic Nanorods", *The Journal of Physical Chemistry Letters*, **2011**.
- [107] L. K. Khorashad, L. V. Besteiro, M. A. Correa-Duarte, S. Burger, Z. M. Wang, A. O. Govorov, "Hot Electrons Generated in Chiral Plasmonic Nanocrystals as a Mechanism for Surface Photochemistry and Chiral Growth", *Journal of the American Chemical Society*, **2020**.
- [108] X. Han, S. Li, Z. Peng, A. M. Othman, R. Leblanc, "Recent Development of Cardiac Troponin I Detection", *ACS sensors*, **2016**.
- [109] D. Lou, L. Fan, Y. Cui, Y. Zhu, N. Gu, Y. Zhang, "Fluorescent Nanoprobes with Oriented Modified Antibodies to Improve Lateral Flow Immunoassay of Cardiac Troponin I", *Analytical Chemistry*, **2018**.
- [110] L. Cohen, N. Cui, Y. Cai, P. M. Garden, X. Li, D. A. Weitz, D. R. Walt, "Single Molecule Protein Detection with Attomolar Sensitivity Using Droplet Digital Enzyme-Linked Immunosorbent Assay", *ACS Nano*, **2020**.
- [111] B. Ince, M. K. Sezgintürk, "Lateral Flow Assays for Viruses Diagnosis: Up-to-Date Technology and Future Prospects", *Trends in Analytical Chemistry*, **2022**.
- [112] I. Wagenhäuser, K. Knies, V. Rauschenberger, M. Eisenmann, M. McDonogh, N. Petri, O. Andres, S. Flemming, M. Gawlik, M. Papsdorf, "Clinical Performance Evaluation of SARS-CoV-2 Rapid Antigen Testing in Point of Care Usage in Comparison to RT-qPCR", *EBioMedicine*, **2021**.
- [113] J. Dinnes, J. J. Deeks, S. Berhane, M. Taylor, A. Adriano, C. Davenport, S. Dittrich, D. Emperador, Y. Takwoingi, J. Cunningham, "Rapid, Point-Of-Care Antigen and Molecular-Based Tests For Diagnosis of SARS-CoV-2 Infection", *Cochrane Database of Systematic Reviews*, **2021**.
- [114] M. L. Wong, J. F. Medrano, "Real-Time PCR for mRNA Quantitation", *Biotechniques*, **2005**.
- [115] W. H. Organization, World Health Organization, **2020**.

- [116] R. L. Schlenger, "PCR-Tests auf SARS-CoV-2: Ergebnisse richtig interpretieren", *Deutsches Arzteblatt International*, **2020**.
- [117] WHO, "Antigen-Detection in the Diagnosis of SARS-CoV-2 Infection", *Interim Guidance*, **2021**.
- [118] A. I. Cubas-Atienzar, K. Kontogianni, T. Edwards, D. Wooding, K. Buist, C. R. Thompson, C. T. Williams, E. I. Patterson, G. L. Hughes, L. Baldwin, C. Escadafal, J. A. Sacks, E. R. Adams, "Limit of Detection in Different Matrices of 19 Commercially Available Rapid Antigen Tests for the Detection of SARS-CoV-2", *Scientific Reports*, **2021**.
- [119] M. Barlev-Gross, S. Weiss, A. Ben-Shmuel, A. Sittner, K. Eden, N. Mazuz, I. Glinert, E. Bar-David, R. Puni, S. Amit, O. Kriger, O. Schuster, R. Alcalay, E. Makdasi, E. Epstein, T. Noy-Porat, R. Rosenfeld, H. Achdout, O. Mazor, T. Israely, H. Levy, A. Mechaly, "Spike vs Nucleocapsid SARS-CoV-2 Antigen Detection: Application in Nasopharyngeal Swab Specimens", *Analytical and Bioanalytical Chemistry*, **2021**.
- [120] C. Aranha, V. Patel, V. Bhor, D. Gogoi, "Cycle Threshold Values in RT-PCR to Determine Dynamics of SARS-CoV-2 Viral Load: An Approach to Reduce the Isolation Period for COVID-19 Patients", *J Med Virol*, **2021**.
- [121] F. Gonzalez Lomeli, N. Elmaraghy, A. Castro, C. V. Osuna Guerrero, L. L. Newcomb, "Conserved Targets to Prevent Emerging Coronaviruses", *Viruses*, **2022**.
- [122] P. Chun, in *Lateral Flow Immunoassay*, Springer, **2009**, pp. 1-19.
- [123] J. O. Tam, H. de Puig, C. W. Yen, I. Bosch, J. Gómez-Márquez, C. Clavet, K. Hamad-Schifferli, L. Gehrke, "A Comparison of Nanoparticle-Antibody Conjugation Strategies in Sandwich Immunoassays", *Immunoassay Immunochem*, **2017**.



# Acknowledgements

The answer to “Would I do my PhD again?” is “Yes!”. I could not have wished for better supervisors than Tim and Amelie. To me they were the right people at the right place and time. Together we were a strong team with great ideas and positive outcome. It was not only a professional but also a personal match which made us successful in our jobs.

*“Ich vertraue prinzipiell immer erst mal meinen PhD Studenten.“ (Tim)*

**Tim** has always believed in my skills and autonomy. I appreciate that I was given complete trust and freedom. Tim is a good listener and puts moralities before his career. He is a constantly growing character with a consciousness for doing good for others. I was lucky to meet him.

**Amelie** is the personification of high spirits (😊). Her communication skills and her empathy have made everyone love her. She has the perfect skills for being a group leader since she has the ability to motivate and to cope with many different characters. Her interest in research and her support has made her the greatest lab partner.

**Susi** was not my supervisor; however, she supported me as much as my supervisors. She was a moral support, an entertainer as well as a positive distraction in high workload times. Tim and she are an example of great long-term work partners.

**Joachim Rädler** defines a person who is a great leader at the same time being sweet and cordial. He showed interest and respect and has always given me the feeling of being appreciated as a valuable part of the chair. He is sometimes “all over the place” which makes him very adorable.

**Everyone** working in Joachim’s chair has contributed to my time at the chair which was a great experience.

**Philip Tinnefeld** is my second corrector and I am very thankful for his support in the last steps of my work.